Synthesis of Carbon and Tungsten Based Thin Films by Plasma Enhanced Chemical Vapor Deposition

A Thesis Submitted to the

College of Graduate Studies and Research

in Partial Fulfillment of the Requirements

for the Degree of Doctoral of Philosophy

in the Department of Physics and Engineering Physics

University of Saskatchewan

Saskatoon

By

Weifeng Chen

© Weifeng Chen, April 2007. All rights reserved.

Permission to use

In presenting this thesis in partial fulfillment of the requirements for a Postgraduate degree from the University of Saskatchewan, I agree that the Libraries of this University may make it freely available for inspection. I further agree that permission for copying of this thesis in any manner, in whole or in part, for scholarly purposes may be granted by the professor or professors who supervised my thesis work or, in their absence, by the Head of the Department or the Dean of the College in which my thesis work was done. It is understood that any copying or publication or use of this thesis or parts thereof for financial gain shall not be allowed without my written permission. It is also understood that due recognition shall be given to me and to the University of Saskatchewan in any scholarly use which may be made of any material in my thesis.

Requests for permission to copy or to make other use of material in this thesis in whole or part should be addressed to:

Head of the Department of Physics and Engineering Physics

University of Saskatchewan

Saskatoon, Saskatchewan

Canada S7N 5E2

Abstract

The main objective of this thesis is to find optimum discharge conditions in plasma reactors to realize controlled synthesis of various carbon-based materials with desired properties. Experimental conditions including substrate biasing, substrate pretreatment, gas flow rate, catalyst coating, and the type of carbon source, play important roles in controlling the nucleation and growth of carbon-based materials. In this Ph.D. work, the effects of various processing factors on nucleation and growth of carbon based materials were systematically investigated. The work has led to a better understanding of how each experimental parameter affects the carbon-based materials growth. Optimization of experiment conditions based on this understanding is beneficial for the controlled synthesis of carbon-based materials with desired properties. In addition, the controlled synthesis of tungsten-based nanostructures using a hot filament reactor was studied.

The main results presented in this thesis are: (1) Synthesis of well-aligned carbon nanotube or carbon nanocone films with a glow discharge under a negative substrate biasing. The electric field in the plasma sheath above the substrate has been found to play an important role in controlling the alignment and orientation of nanotubes or nanocones. (2) Synthesis of high purity diamond films using solid graphite as the carbon source by graphite etching. The technique provides a route to realizing deposition of high quality diamond films at low substrate temperatures (typically as low as 350 ℃). (3) Successful synthesis of high quality diamond films on aluminum-coated steels using a graphite etching technique. The aluminum interlayer effectively reduces the graphitization which occurs on a steel substrate. (4) Synthesis of nanocrystalline diamond films with smooth surfaces under high gas flow rates with a positive substrate biasing. Both high gas flow rate and positive biasing effectively increase the nucleation

density of diamond and therefore reduce the diamond grain size. (5) Synthesis of high purity crystalline tungsten or tungsten oxide nanorod films by optimizing the filament temperature in a hot filament reactor.

Acknowledgements

I would like to express deepest thanks and appreciation to my supervisors, Professor Akira Hirose and Professor Chijin Xiao, for being the chief motivators and providing timely guidance and support throughout all phases of this thesis work. Without them, this work would not have been possible.

I especially thank Professor Qiaoqin Yang for her friendship and many insightful discussions. Her untiring willingness to teach and encourage me made the whole course of this thesis work highly enjoyable. Her dedication to material science has been a great inspiration. I am also indebted to her for the fruitful collaboration in experiments described in Chapter 3 and Chapter 4 in this thesis.

I would like to thank Mr. Dave McColl for his friendship and kind technical assistance whenever needed. I would also like to thank my fellow graduate students Dazhi Liu, Xianfeng Lu, J.T. Steenkamp, and postdoctoral fellow Yuanshi Li for providing a friendly atmosphere in which to work and relax. In particular, I appreciate Xianfeng Lu's help in characterizing field emission properties of nanocrystalline diamond films presented in Chapter 3. A note of thanks is also in order for the Physics Machine Shop (Perry Balon, Blair Chomyshen and Ted Toporowski) and for Tom Bonli, and Jason Maley, who provided help in sample characterizations.

Finally, I would like to thank all my family members for their patience and love throughout the tenure of my work on this thesis.

The financial support provided by the Canada Research Chair Program, the Natural Sciences and Engineering Research Council of Canada and the University of Saskatchewan is acknowledged with gratitude.

Dedicated to my parents.

Table of Contents

Permission to use I
Abstract II
Acknowledgements IV
Table of Contents VI
Acronyms VIII
List of Tables X
List of Figures XI
Chapter 1 Introduction 1
1.1 Carbon allotropes 2
1.2 Properties and applications of diamond 8
1.3 Chemical vapor deposition of diamond 11
1.3.1 Hot filament CVD 14
1.3.2 Microwave plasma CVD 16
1.4 Properties of and applications of carbon nanotubes 18
1.5 Carbon nanotubes synthetic techniques 20
1.6 Plasma 23
1.7 Plasma sheath 26
1.8 Motivation and organization of thesis 28
Chapter 2 Plasma reactors and sample characterization techniques 31
2.1 Hot filament CVD reactor 31
2.2 Microwave CVD reactor 33
2.3 SEM 37
2.4 Raman spectroscopy 39
2.5 XRD 43
2.6 AFM 45
2.7 TEM 47
Chapter 3 Effects of substrate biasing on the growth of carbon based materials 50
3.1 Effects of bias polarity on the growth of carbon-based materials 51
3.1.1 Introduction 51
3.1.2 Experiment 53
3.1.3 Results and discussion 54

3.1.4 Conclusion 56
3.2 Substrate bias effect on the orientation control of carbon nanotubes 57
3.2.1 Introduction 57
3.2.2 Experiments 59
3.2.3 Results and discussion 61
3.2.4 Conclusion 68
Chapter 4 Effects of the carbon source: graphite etching 70
4.1 Low temperature synthesis of diamond thin films with in situ graphite etching 70
4.1.1 Introduction 70
4.1.2 Experiments 71
4.1.3 Results and discussion 72
4.1.4 Conclusion 77
4.2 Deposition of diamond thin films on steels using graphite etching 77
4.2.1 Introduction 77
4.2.2 Experiments 79
4.2.3 Results and discussion 80
4.2.4 Conclusion 83
Chapter 5 Effects of gas flow rate on diamond nucleation and growth 84
5.1 Introduction 84
5.2 Experiments 85
5.3 Results and discussion 86
5.4 Conclusion 95
Chapter 6 Synthesis of high purity tungsten-based nanostructures 96
6.1 Introduction 96
6.2 Experiment 97
6.3 Results and discussion 98
6.4 Conclusion 103
Chapter 7 Conclusions and future work 105
7.1 Conclusions 105
7.2 Suggestions for future work 107
References 109

Acronyms

AFM	Atomic force microscopy
BCC	Body-centered cubic
BEG	Bias enhanced growth
BEN	Bias enhanced nucleation
CCD	Charge-coupled device
CNT	Carbon nanotube
CVD	Chemical vapor deposition
FCC	Face-centered cubic
FEE	Field electron emission
FWHM	Full width at half maximum
HFCVD	Hot filament chemical vapor deposition
HPHT	High pressure high temperature
HREM	High Resolution Electron Microscopy
MCD	Microcrystalline diamond
MWCVD	Microwave chemical vapor deposition
MWNT	Multi-walled nanotubes
NCD	Nanocrystalline diamond
NIRIM	National Institute for Research in Inorganic Materials
PECVD	Plasma enhanced chemical vapor deposition
SEM	Scanning electron microscopy
STM	Scanning tunneling microscope
SWNT	Single-walled nanotubes
TE	Transverse electric

TM Transverse magnetic

TEM Transmission electron microscope

VS Vapor-solid

XRD X-ray diffraction

List of Tables

Table 1: Some of the outstanding properties of diamond. [*Ashfold et al.*, 1994].............9
Table 2: Typical growth parameters and their variation range.......................................60
Table 3: Typical FEE parameters of diamond films grown at various gas flow rates (sccm): 200, (b) 300, and (c) 400..92

List of Figures

Figure 1.1: Molecular structures of carbon allotropes: graphite, diamond, fullerene, and carbon nanotube. 3
Figure 1.2: Crystal structure of diamond. [http://en.wikipedia.org/] 4
Figure 1.3: Crystal structure of graphite. [http://en.wikipedia.org/] 5
Figure 1.4: Structure of amorphous carbon. [http://en.wikipedia.org/] 8
Figure 1.5: Simplified diagram showing the Berman-Simon line which indicates the regions of pressure and temperature where diamond is in the stable phase. [*Harlow*, 1998] 11
Figure 1.6: Schematic diagram of the physical and chemical processes during diamond CVD. [http://www.chm.bris.ac.uk/] 13
Figure 1.7: Schematic diagram of a HFCVD reactor. 15
Figure 1.8: Schematic diagrams of: (a) NIRIM-type (b) ASTEX-type microwave plasma CVD reactors. [http://www.chm.bris.ac.uk/] 17
Figure 1.9: Schematic experimental setups for nanotube growth method: (a) arc-discharge method, (b) laser ablation method, and (c) catalyst-assisted CVD method. [*Dresselhaus et al.*, 2001] 22
Figure 1.10: Two general growth modes of nanotube in catalyst –assisted chemical vapor deposition. Left: base growth mode. Right: tip growth mode. [*Dresselhaus* et al., 2001] 23
Figure 1.11: Space and laboratory plasmas on log n versus log T_e scales. [*Lieberman* and *Lichtenberg*, 1994] 25
Figure 1.12: The formation of plasma sheaths: (a) initial ion and electron densities and potential; (b) densities, electric field, and potential after formation of the sheath. [*Lieberman* and *Lichtenberg*, 1994] 28
Figure 2.1: Schematic diagram of the HFCVD system.. 32
Figure 2.2: A picture of the HFCVD system. 32
Figure 2.3: A picture of the microwave plasma CVD reactor. 34
Figure 2.4: Schematic diagram of the microwave CVD reactor. 35
Figure 2.5: Reactor modelling by Funer *et al* [*Funer et al.*, 1995]. The diagram on the left shows the calculated electric field strength in the reactor, while that on

the right shows the calculated plasma location. The bar through the centre of the reactor represents the position of the quartz window. 36
Figure 2.6: Emitted particles and photons from a specimen due to the incident electron beam in a scanning electron microscope. [*Watchman*, 1993]...................38
Figure 2.7: Raman spectrum of natural diamond (type IIa), showing the main Raman active mode at ~1332 cm^{-1} (taken using 514 nm laser excitation wavelength). [http://www.chm.bris.ac.uk/]...40
Figure 2.8: Raman spectrum of graphite, showing D-band and G-band. Raman spectrum taken using 514 nm laser excitation. 42
Figure 2.9: Raman spectrum of CVD diamond with non-diamond carbon in the film. Raman spectrum taken using 514 nm laser excitation. The increasing base line is due to amorphous carbon. 42
Figure 2.10: Raman spectrum of high quality CVD diamond synthesized in this thesis work. Raman spectrum taken using 514 nm laser excitation....................43
Figure 2.11: Reflection of X-rays from two planes of atoms in a crystal. 44
Figure 2.12: Relationship of rotation angles of the sample and detector. 45
Figure 2.13: Schematic diagram of an AFM. 46
Figure 2.14: Schematic presentation of a TEM [http://nobelprize.org/]. 48
Figure 2.15: Sample TEM images of closed (left) and open (right) multiwall nanotubes [http://physicsweb.org/]. 48
Figure 3.1: SEM images of films with three substrate bias voltages: (a) without biasing, (b) 50 V, and (c) -300 V...54
Figure 3.2: (a) Cross section SEM image of nanocone film, (b) TEM image of a carbon nanocone. 55
Figure 3.3: Raman spectroscopy of graphitic nanocone. 55
Figure 3.4: Schematic diagram of the hot filament plasma sputtering coating device. The main parameters are also listed in the diagram. 59
Figure 3.5: SEM micrograph of carbon nanotubes grown without bias voltage...........61
Figure 3.6: SEM (top view) images of nanotubes grown at -400 V bias at different regions: (a) at the left edge, (b) between the edge and center, (c) in the center region. 63

Figure 3.7: Angles between the CNTs alignment and the sample normal, as a function of the distance from the sample edge for three gas pressures in the discharge. 64
Figure 3.8: TEM image of a typical multi-walled carbon nanotube. 65
Figure 3.9: A cut-way view of the sample and the expected electric field lines in the cathode region around the sample for (a) narrow and (b) wide cathode region. 68
Figure 4.1: Typical SEM morphologies (plan-view) of diamond films grown on silicon at substrate temperatures (a) 310 ℃ for 10 h and (b) 250 ℃ for 20 h. 73
Figure 4.2: Typical SEM morphologies (plan-view) of diamond films grown on silicon at substrate temperatures (a) 310 ℃ for 10 h and (b) 250 ℃ for 30 h using conventional H_2 + 1% CH_4 gas mixture. 73
Figure 4.3: Typical Raman spectra of the diamond films grown at substrate temperature (a) 310 ℃ for 10 h and (b) 250 ℃ through graphite etching; (c) 310 ℃ and (d) 250 ℃ using conventional H_2 + 1% CH_4 gas mixture. 75
Figure 4.4: SEM image of the carbon layer formed on a mild steel substrate using graphite etching. 80
Figure 4.5: Typical Raman spectrum of the carbon layer deposited on a mild steel substrate using graphite etching. 81
Figure 4.6: SEM image of diamond film deposited on the aluminum-coated steel substrate using graphite etching. 82
Figure 4.7: Raman spectrum of the diamond film deposited on the aluminum-coated steel substrate using graphite etching. 82
Figure 5.1: Typical SEM morphologies (plan-view) of films grown at various gas flow rates (sccm) of: (a) 200, (b) 300, and (c) 400. 87
Figure 5.2: The 0.5×0.5 μm^2 and (b) the 20×20 μm^2 AFM topography of the NCD film grown at gas flow rate of 400 sccm. 89
Figure 5.3: Typical Raman spectra of the diamond films grown at gas flow rates (sccm) of: (a) 200, (b) 300, and (c) 400. 89
Figure 5.4: XRD pattern of the NCD film grown at a flow rate of 400 sccm. 90
Figure 5.5: FEE current vs. electric field curves of the diamond films grown at various gas flow rates (sccm): (a) 200, (b) 300, and (c) 400. 91

Figure 5.6: Morphology of the NCD film grown at a flow rate of 400 sccm with a positive biasing during the diamond growth stage: (a) SEM image, and (b) $0.5\times0.5\ \mu m^2$ AFM image..93
Figure 6.1: (a) Typical SEM micrographs of samples deposited at different filament temperatures: (a) 1600 ℃; (b) 1940 ℃; (c) 2000 ℃; (d) 2280 ℃.............98
Figure 6.2: (a) Typical TEM image of nanorods deposited at a filament temperature of 2140 ℃; (b) HREM image of a nanorod deposited at a filament temperature of 2140 ℃. 99
Figure 6.3: XRD patterns of nanorods grown at different filament temperatures: (a) 2000 ℃; (b) 2140 ℃; (c) 2240 ℃; (d) 2280 ℃......................................100
Figure 6.4: Integrated area ratio of main peak of W to the WO_{2+x} main peak in XRD measurements from samples grown at different filament temperatures. Each point in the error bar represents an average of 6 samples grown on the same condition. 101

Chapter 1

Introduction

A plasma is an ionized gas consisting of electrons, ions and neutrals. Plasma has become indispensable for advanced materials processing because plasma can provide a highly excited medium that has no chemical or physical counterpart in a natural, equilibrium environment. Plasmas alter the normal pathways through which chemical systems evolve from one stable state to another, thus providing the potential to produce materials with properties that are not attainable by any other means. There are many applications of plasma-based material processing technologies. The role of plasma technology in fabrication of computer chips is perhaps best known. Without the dry etching technology enabled by plasma reactors, fabrication of high aspect ratio (height/width) nanoscale structures would have been impossible. A current and emerging theme of plasma-based materials processing is plasma-assisted synthesis of materials with novel properties. Carbon-based materials including diamond, carbon nanotubes (CNTs) and other carbon nanostructures, have many attractive properties for practical applications. The research project of this thesis is in the field of plasma-assisted syntheses of carbon-based materials. In addition, the synthesis of high purity tungsten nanorod films is studied.

This introductory Chapter focuses on plasma-assisted synthesis of carbon-based materials. After a brief description of carbon allotropes in Section 1.2, the properties and synthesis techniques of diamond and carbon nanotubes, and plasmas in processing

reactors will be introduced. The motivation for the research will be addressed in Section 1.5. The major findings and outline of this thesis will be given in Sections 1.6 and 1.7.

1.1 Carbon allotropes

An *allotrope* is a variant of a substance consisting of only one type of atom. Allotropes differ in the way the atoms bond with each other and arrange themselves into a structure. Because of their different molecular structures, allotropes have different physical and chemical properties. Substances that have allotropes include carbon, oxygen, sulfur, and phosphorus.

Carbon allotropes include graphite, diamond, amorphous carbon, the recently discovered fullerene [*Kroto et al*., 1985] and carbon nanotube [*Iijima*, 1991]. Carbon allotropes have substantial physical and chemical differences. For example, pure diamond is an electrical insulator, while graphite is a good conductor. Diamond is one of the hardest materials known, while graphite is one of the softest. Diamond is usually transparent, but graphite is opaque. The differences arise from the differences in chemical bonds (or electronic configuration) between carbon atoms. In carbon allotropes, carbon atoms bond to each other covalently by sharing electron pairs. The covalent bonds have directional properties. This in turn gives carbon the ability to adapt into various molecular and crystalline structures (Fig. 1.1).

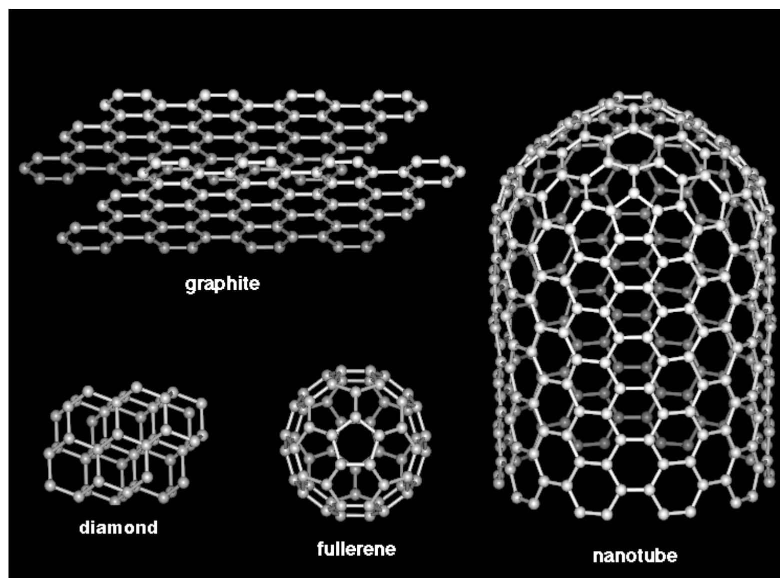

Figure 1.1: Molecular structures of carbon allotropes: graphite, diamond, fullerene, and carbon nanotube.

Carbon, like many of the second-row elements in the Periodic Table, has atomic orbitals that can hybridize. A carbon atom has four valence electrons (one s-orbital electron and three p-orbital electrons) in the outer electronic shell. Carbon can adapt to form chemical bonds with different geometries (or different hybridized bonds).

In diamond, one 2s electron (2s: -19.20 eV) and three 2p electrons (2p: -11.79 eV) are mixed to form four hybrid orbitals, which are called sp^3 hybridization orbitals (sp^3: -13.64 eV, 4 sp^3 valence electrons, responsible for sigma bonds). Each carbon atom is bonded tetrahedrally to four other nearest carbon atoms. The bond lengths are 1.544 Å and the bond angles between any two of the bonds are about 109.5°. As a result, diamond has a face-centered cubic (FCC) crystal structure as shown in Fig. 1.2.

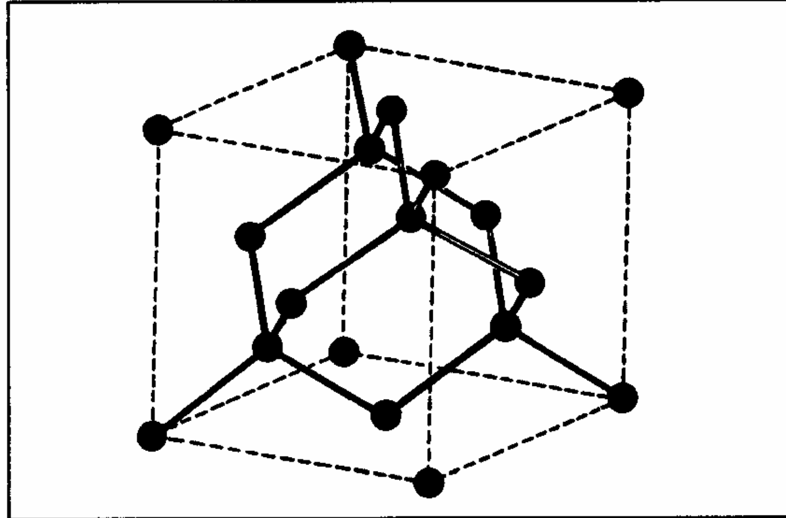

Figure 1.2: Crystal structure of diamond. [From http://en.wikipedia.org/]

The hardness of diamond can be attributed to its crystalline structure and the strength of the chemical bonds between its carbon atoms. The interlocking network of covalent bonds makes the structure very rigid. Diamond is well known as the hardest material (hardness: 1200 GPa). Diamond has also the highest elastic modulus and is the least compressive substance. Since the valence electrons in diamond are involved in the formation of sigma bonds and no delocalized pi bonds, diamond has a very low electrical conductivity.

In graphite, one 2s electron and two 2p electrons of a carbon atom are mixed to form three sp^2 orbitals (sp^2: -14.26 eV, three sp^2 valence electrons, responsible for sigma bonds). The geometry of the sp^2 hybridized orbital is trigonal planar. The other unmixed 2p electron forms a pure orbital (responsible for pi bonds). As a result, graphite has a layered structure (Fig. 1.3). Each graphene layer is made up of rings containing six carbon atoms. The rings are linked to each other in a structure that resembles the hexagonal mesh of chicken-wire. Within a graphene sheet, each carbon

atom covalently bonds (sp^2 bonds, bond length of 1.421 Å, with 120° between any two of the bonds) to three nearest neighbor carbon atoms and belongs to three neighboring rings. The fourth electron (the unaffected p-orbital electron, 2p: -11.79 eV) of each carbon atom becomes part of an extensive pi bond system that resides above and below each graphite sheet.

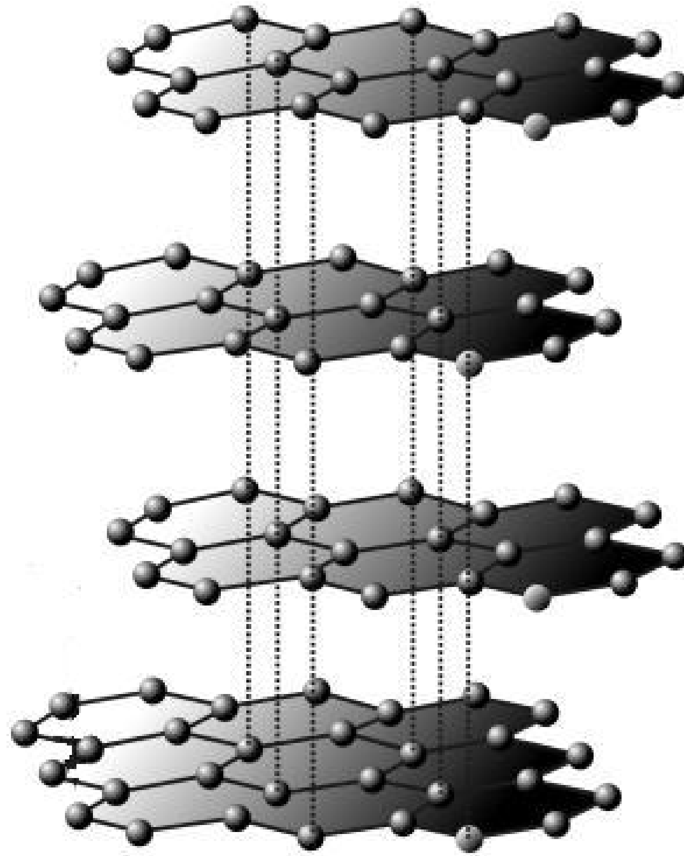

Figure 1.3: Crystal structure of graphite. [From http://en.wikipedia.org/]

The electrical conductivity and softness of graphite can be related to graphite's crystalline structure. The bonds between the carbon atoms within the layer are stronger than those in diamond. There is also distributed pi bonding between the carbon atoms in the sheet. The electrons in the delocalized pi bonding system can move around

throughout the graphite and they are responsible for the high electrical conductivity of graphite. Bonds between atoms within a layer of graphite are strong, but the forces (Van der Waals forces) between the layers are weak. Because the layers can slip past each other, graphite is soft and can be used as lubricant.

The fullerenes were discovered in 1985 by Kroto and co-workers as an entirely new form of carbon, which became known as C_{60} or the fullerene molecule. The fullerene molecule consists of 60 carbon atoms arranged in pentagons and hexagons, very like in a standard soccer ball. It is also known as Buckminster Fullerene due to the resemblance of this shape to the geodesic domes designed and built by the architect R Buckminster Fuller. It was soon discovered that C_{60} is not the only ball-like carbon molecule possible (although it is the most stable and the most dominant). The rugby-ball shaped C_{70} molecule or other ellipsoid and tubular carbon molecules are other possibilities. Fullerenes are similar in structure to graphite, which is composed of a sheet of linked hexagonal rings, but they also contain pentagonal (or sometimes heptagonal) rings that prevent the sheet from being planar. Fullerenes have been found in interstellar space and can also be artificially synthesized. As of the early twenty-first century, the chemical and physical properties of fullerenes are still under active study. For example, potential application of fullerenes as drug delivery agents has been recognized for binding specific antibiotics to the structure to target resistant bacteria and even to target certain cancer cells such as melanoma.

The name of carbon nanotubes (CNT) is derived from their size and tubular shape, since the diameter of a nanotube is on the order of few nanometers (approximately 50,000 times smaller that the diameter of a human hair). The bonding in carbon nanotubes is sp^2, with each atom joined to three neighbours, as in graphite. The tubes can therefore be considered as rolled-up graphene sheets (graphene is an individual

graphite layer). There are two forms of nanotube structures. Single-walled nanotubes (SWNT) can be considered as a long wrapped graphene sheet. Multi-walled nanotubes (MWNT) can be considered as a collection of concentric SWNTs with different diameters. The sp^2 bonding structure in a carbon nanotube, stronger than the sp^3 bonds found in diamond, provides the molecules with their unique strength. The stiffness of a material is measured in terms of its Young's modulus, the rate of change of strain with applied stress. The Young's modulus of the best nanotubes can be as high as 1000 GPa which is approximately 5 times higher than that of steel. The tensile strength, or breaking strain of nanotubes can be up to 63 GPa, around 50 times higher than that of steel. Carbon nanotubes are among the strongest and lightest materials known.

Amorphous carbon is the terminology used for carbon material that does not have any crystalline structure (see Fig. 1.4). As with all glassy materials, some short-range order can be observed, but there is no long-range pattern of atomic positions. Coal and soot are both forms of amorphous carbon, one of the most common carbon allotropes.

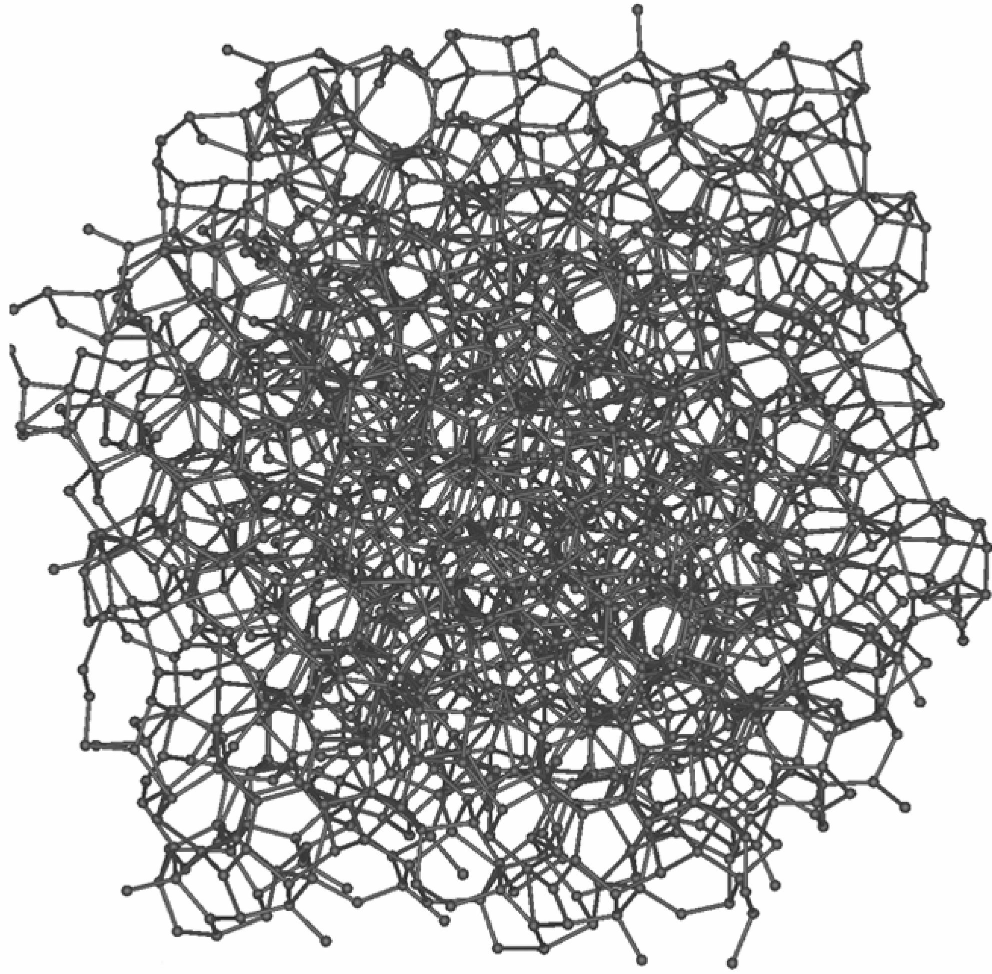

Figure 1.4: Structure of amorphous carbon. [From http://en.wikipedia.org/]

1.2 Properties and applications of diamond

Diamond is of particular interest due to its extraordinary physical properties. These include high hardness, high electrical resistivity, high thermal conductivity, good optical transparency in a wide spectral range, chemical inertness, low coefficient of expansion, low friction, wear resistant, and biological compatibility. Some of the outstanding properties of diamond are shown in Table 1.

Table 1: Some of the outstanding properties of diamond. [*Ashfold et al.*, 1994]

Extreme mechanical hardness (~ 90 GPa)
Strongest known material, highest bulk modulus (1200 GPa), lowest compressibility (8.3×10^{-13} m^2 N^{-1})
Highest known value of thermal conductivity at room temperature (2000 Wm^{-1} K^{-1})
Low thermal expansion coefficient at room temperature (0.8×10^{-6} K^{-1})
Broad optical transparency from deep UV to the far IR region of the electromagnetic spectrum
Good electrical insulator (room temperature resistivity is ~ 10^{16} Ω cm)
Diamond can be doped to change its resistivity over the range 10-10^6 Ω cm, so becoming a semiconductor with a wide band gap of 5.4 eV
Chemically inert and corrosion resistant
High radiation hardness

Given these many notable properties, it should come as no surprise that diamond finds uses in many diverse applications (beside its use as a gem) including heat sinks, abrasives, and wear-resistant coatings for cutting tools. Diamond films are coated on the surfaces of cutting tools to increase their hardness, wear resistance, and heat dissipation capacity. This allows tools to be operated at high temperatures and with longer lifetime.

The thermal conductivity of diamond at room temperature is 2000 W m^{-1} K^{-1}, which is about five times that of copper. Diamond has a high melting point (3820 K). The thermal expansion coefficient of diamond at 300 K is merely 0.8×10^{-6} K^{-1}. The thermal properties of diamond, coupled with its high electrical resistivity, make diamond an ideal material in use as heat spreaders for high powered electronic devices. For example, diamond heat spreaders are already used in manufacturing solid state laser diodes.

Diamond is transparent to broad segments of the electromagnetic spectrum. Beginning with the long wavelengths of the electromagnetic spectrum, diamond, like

most electrical insulators, is transparent to radio-waves and microwaves and continues to be transparent into the infrared region except for a few strong characteristic absorption bands.

Diamond has a large band-gap (5.4 eV), high electrical resistivity, high carrier charge mobility, and high radiation tolerance. Once successfully doped, diamond could become a wide-band-gap semiconductor with many desired physical, thermal, and chemical properties as described above. Recent progress in diamond film processing has demonstrated that doping of diamond films grown in a low-pressure gas environment with certain impurities may lead to the development of new electronic devices, making diamond a promising semiconductor for electronic applications. However, it should be mentioned that it is very difficult to produce n-type doped diamond at the present time, although p-doped diamonds exist in nature and have also been synthesized.

The outstanding and unique properties described above make diamond a much sought-after substance for a wide range of applications. The natural diamond is rare and expensive. It has therefore long been desired to develop methods to synthesize diamond in the laboratory. A variety of techniques have evolved for the synthesis of diamond, including High Pressure High Temperature (HPHT) processes, and Chemical Vapor Deposition (CVD).

Early experiments to produce synthetic diamonds used a High Pressure High Temperature process that produced diamond under conditions where it was the thermodynamically stable form of carbon with the help of metal catalysts (Fig. 1.5). This technique was pioneered by the General Electric company in the USA in 1955 [*Bundy et al.*, 1955]. In this method, diamond is crystallized from graphite at P ~ 50-100 kBar and T ~ 1800-2300 K. HPHT grown diamond tends to consist of small crystals of a few millimetres in diameter.

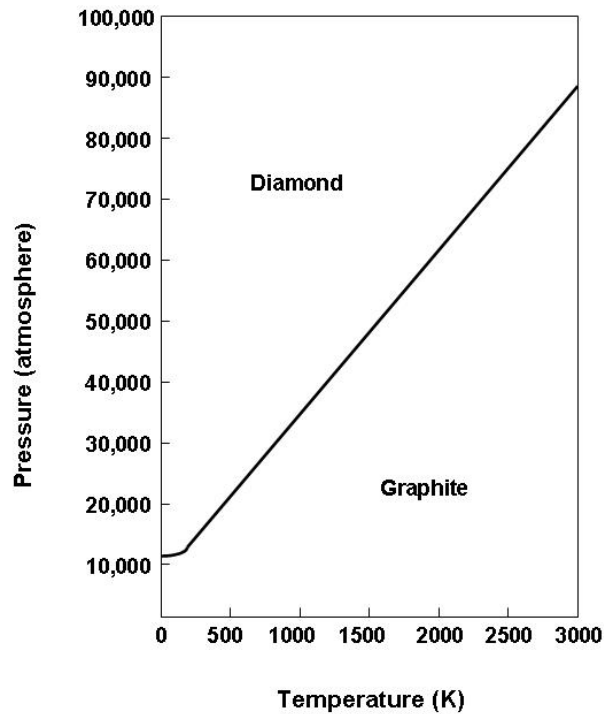

Figure 1.5: Simplified diagram showing the Berman-Simon line which indicates the regions of pressure and temperature where diamond is in the stable phase. [*Harlow*, 1998]

The advent of chemical vapor deposition of diamond has dramatically increased the possibility of exploitation of its other extraordinary properties and potential wide-range industrial applications. This technique uses, as process gases, a standard hydrocarbon gas (typically methane) in an excess of hydrogen. The resultant diamond produced by this technique can display properties comparable to those of natural diamond. In the next section, the diamond CVD technique will be described in detail.

1.3 Chemical vapor deposition of diamond

Chemical vapour deposition of polycrystalline diamond film is an approach that can be used to synthesize diamond at much lower temperatures and pressures under non-

equilibrium conditions [*Angus et al.*, 1988; *Ashfold et al.*, 1994]. CVD diamond can show mechanical, tribological, and even electronic properties comparable to those of natural diamond. The possibility of coating large surface areas with a continuous film of diamond will open up whole new ranges of potential application for the CVD methods.

Chemical vapor deposition involves gas phase chemical reactions which transform gaseous molecules into a solid material in the form of thin film or powder on the surface of a substrate. The technique used for diamond film deposition is now established and has been well described in a number of review articles [*Angus et al.*, 1988; *Ashfold et al.*, 1994]. A basic reaction in the CVD of diamond is based on the decomposition of a hydrocarbon, such as methane, as follows:

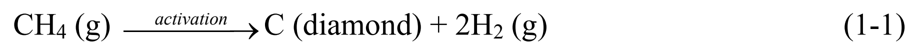

$$CH_4\,(g) \xrightarrow{activation} C\,(diamond) + 2H_2\,(g) \qquad (1\text{-}1)$$

The deposition process involves a complex mechanism which is not fully understood at this time. Two conditions seem necessary: (a) activation of the carbon species, and (b) the action of atomic hydrogen. The complex chemical and physical processes which occur during diamond CVD are illustrated in the Fig. 1.6. The process gasses first mix in the chamber before diffusion toward the substrate surface. They pass through an activation region, e.g., a hot filament or microwave plasma, which provides energy to the gaseous species. This activation causes molecules to fragment into reactive radicals and atoms, creates ions and electrons, and heats the gas up to temperatures reaching a few thousand Kelvins. Beyond the activation region, these reactive fragments continue to mix and complete a complex set of chemical reactions until they strike the substrate surface. At this point the species either adsorb and react with the surface, or desorb again back into the gas phase, or diffuse around close to the surface until an appropriate reaction site is found. If all the conditions are suitable, surface reactions for growth of diamond occur.

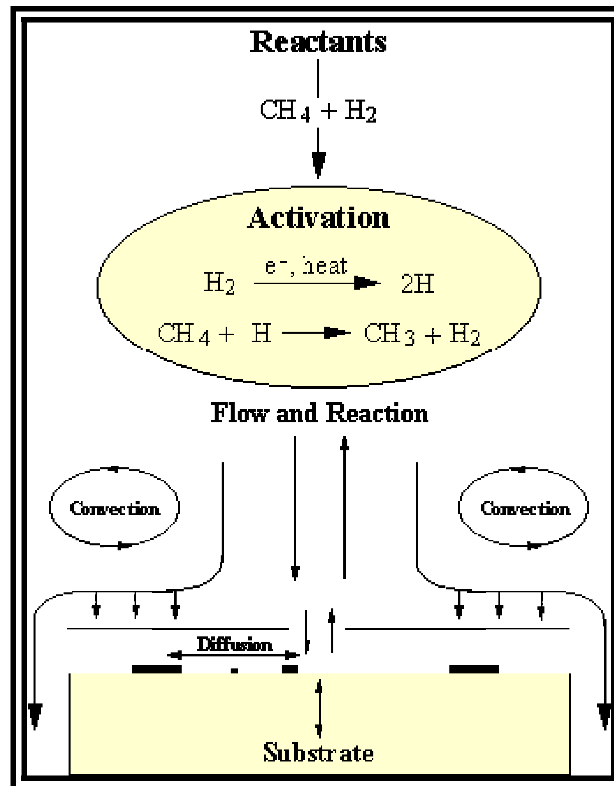

Figure 1.6: Schematic diagram of the physical and chemical processes during diamond CVD. [http://www.chm.bris.ac.uk/]

A number of studies have been performed to identify the chemical process responsible for diamond growth in the last 20 years. A plausible mechanism for CVD diamond growth is that the methyl radical (CH_3) is the important compound in generating the growth of CVD diamond [*Yarbrough* and *Messier*, 1992]. Acetylene (C_2H_2) contributes also to diamond growth, particularly in its initial nucleation stage [*Spear*, 1989]. The methyl radicals, along with other gas-phase species, will be transported towards the substrate by a combination of convective and diffusive flow mechanisms depending on the particular process conditions.

It has also been proposed that atomic hydrogen is the most critical component in the gas phase mixture. The presence of hydrocarbon radicals and excessive atomic

hydrogen in the deposition gas provide a dynamic non-equilibrium system, in which only sp^3 carbon bonding can survive. The hydrocarbon radicals provide the vapor source of carbon for diamond deposition. The atomic hydrogen is believed to play several critical roles: 1) H atoms react with neutral species such as CH_4 to create reactive radicals, such as CH_3, which can attach to an adequate surface; 2) atomic hydrogen is known to etch graphitic sp^2 carbon twenty times faster than diamond-like sp^3 carbon [*Hsu*, 1988]. The H atoms thus serve to preferably remove graphitic bonding that may form on the surface, while leaving only high quality diamond.

To deposit diamond by CVD, the carbon species must be activated since, at low pressure, graphite is thermodynamically stable and without activation only graphite would be formed. Activation is obtained by two energy-intensive methods: high temperature (e.g. hot filament) and plasma (e.g. microwave). In the following sub-sections, brief introductions of hot filament CVD and microwave CVD will be given.

1.3.1 Hot filament CVD

The oldest and most widely studied method to produce polycrystalline diamond films is the Hot Filament CVD (HFCVD) technique. In the original design of Matsumoto [*Matsumoto et al.*, 1982], the key part of the HFCVD set-up is the metal filament (typically tantalum or tungsten) which is heated to about 2200 ℃. This hot filament is used to activate the gas mixture, generally comprising a few percent of methane in hydrogen. The deposition is performed at reduced pressures (1 to 30 Torr) and the substrate is placed within a small distance from the filament (~1 cm). In addition, a DC power supply can be connected between the hot filament and the substrate, either to initiate a glow discharge or to bias the substrate with respect to the filament without

initiating a discharge. A schematic diagram of an HFCVD apparatus is shown in Fig. 1.7.

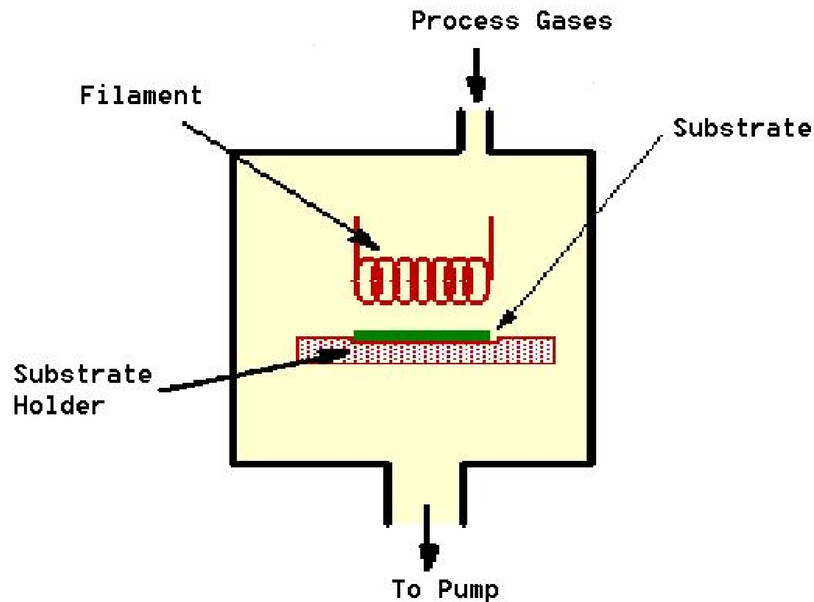

Figure 1.7: Schematic diagram of a HFCVD reactor.

HFCVD provides some advantages over other diamond CVD techniques. The major advantage of such systems is that they are relatively simple (and therefore inexpensive). Another advantage of an HFCVD process is that it is easy to scale up the diamond film deposition. In the HFCVD process, the power consumption is only proportional to the deposition area (number of filaments), while for other diamond CVD techniques it is proportional to the volume of the gas activation. Constructing a sandwich of alternating substrate holders and filament arrays, the reactor volume and gas consumption can be further improved. By the use of arrays of multiple filaments the method can be scaled up for larger deposition area.

The major drawback of the HFCVD technique is the use of the filament itself. Because of the deformation during the carburization process and the high brittleness of

the tungsten carbide phases as compared to pure tungsten, the filament demands careful handling. The lifetime of the filament is relatively short (~80 h). Besides, the filament heats up the substrate inhomogeneously and the filament material slowly evaporates causing contamination in the grown diamond film.

1.3.2 Microwave plasma CVD

In a microwave plasma CVD system, as the name suggests, microwave radiation (typically 2.45 GHz) is coupled into the gas mixture thereby forming and sustaining a plasma. Electron bombardment is a significant contributor to ionisation and decomposition of the gas. Efficient coupling of energy into vibrational levels allows gas temperatures of 2000-3000 K to be attained, prompting thermal dissociation of molecular hydrogen and hydrocarbon gases. The first microwave plasma CVD reactor was designed at NIRIM (National Institute for Research in Inorganic Materials, in Japan). The NIRIM-type microwave reactor is schematically illustrated in Fig. 1-8a. In this configuration a quartz tube is placed within a waveguide. The substrate is placed on a substrate holder at a position where a plasma is formed.

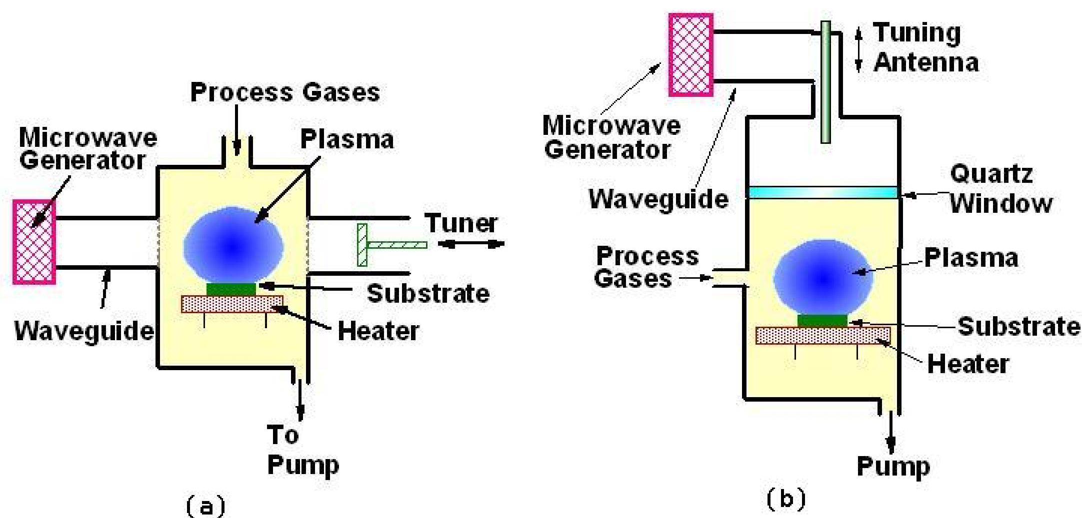

Figure 1.8: Schematic diagrams of: (a) NIRIM-type (b) ASTEX-type microwave plasma CVD reactors. [http://www.chm.bris.ac.uk/]

In 1988, a new design of microwave plasma CVD reactor (ASTEX-type, ASTEX being a commercial manufacturer of plasma systems based in the US) was reported by Bachmann *et al.* [*Bachmann et al.*, 1988]. A schematic of such an ASTEX-type reactor is presented in Fig. 1.8b. In this configuration microwaves are directed along a waveguide and are coupled into the chamber via an antenna. Microwaves pass through a quartz window and into the reactor. One advantage of this set-up is that the reactor walls are stainless steel, thus deposited films are free of Si and O contamination, which was a problem when using the quartz reactor tube in a NIRIM type reactor. The steel chamber also allows the use of higher microwave powers (up to 6 kW) than the NIRIM design. The microwave plasma CVD reactor used in this thesis belongs to ASTEX-type.

Although microwave plasma CVD reactors are much more expensive (due to their complexity) than HFCVD systems, they are widely used because of the following advantages. The microwave plasma is an electrode-free discharge so that the

contamination of diamond films by electrode materials can be avoided. This is of particular importance for the growth of high quality diamond films for electronic applications. Also, the microwave plasma is very stable over many days, and a subtle control of the plasma, and hence the properties of synthesized diamond film, is possible.

1.4 Properties of and applications of carbon nanotubes

Since their discovery in 1991 by Iijima and others, carbon nanotubes (CNTs) have been investigated by many researchers extensively [*Iijima*, 1991]. CNTs are characterized by a large length/diameter aspect ratio. Electronic, molecular and structural properties of carbon nanotubes are determined to a large extent by the chirality and periodic structures. Carbon nanotubes are expected to have remarkable material properties and hold tremendous promise for numerous applications. Those special properties include high mechanical strength, high chemical robustness, high thermal conductivity, good capillary properties [*Pederson* and *Broughton*, 1992], and wide range of electrical conductivities.

Because of the stiffness of carbon nanotubes, they are ideal candidates for structural applications. For example, they may be used as reinforcement in high strength, low weight, and high performance composites.

Depending on their precise molecular symmetry, some nanotubes are semiconductors, while others exhibit truly metallic conductivity. This behavior, coupled with their nanoscale geometry, makes them ideal, perhaps unique, candidates for wires, inter-connecters, and even devices for true molecular electronics [*Colbert*, 1999].

Carbon nanotubes are considered as ideal electron field emitters [*de Heer et al.*, 1995; *Fan et al.*, 1999]. If a solid is subjected to a sufficiently high electric field, electrons near the Fermi level can be extracted from the solid by tunneling through the surface potential barrier. The emission current depends on the strength of the local electric field at the emission surface and its work function (which denotes the energy necessary to extract an electron from its highest bounded state into the vacuum). The applied electric field must be very high in order to extract an electron. This condition is fulfilled for carbon nanotubes, because their elongated shape in small size ensures a large local field enhancement. For technological applications, the emissive material should have a low threshold emission field and large stability at high current density. Furthermore, an ideal emitter is required to have a nanometer size diameter, structural integrity, a high electrical conductivity, and a large chemical stability. Carbon nanotubes possess all these properties. Examples of potential applications of nanotubes as field emitting devices are flat panel displays, electron guns for electron microscopes, and atomic force microscope (AFM) tips.

Because of their flexibility, nanotubes can be also used in scanning probe instruments. It has been reported that the carbon nanotubes are one of the best probe tips for scanning tunneling microscopy [*Dai et al.*, 1996]. Advantages are the improved resolution in comparison with conventional Si or metal tips and also the tips do not suffer from crashes with the surfaces because of their high elasticity.

1.5 Carbon nanotubes synthetic techniques

There are several known methods to produce CNTs. The most common techniques used nowadays are: arc discharge, laser ablation, and catalyst assisted chemical vapor deposition.

Among the techniques described above, electric arc discharge has been used most frequently due to the simplicity of this technique. The principle of this method is based on an arc discharge between two graphite electrodes under an inert atmosphere of helium or argon at pressure of hundreds of Torrs [*Ebbesen* and *Ajayan*, 1992]. Figure 1-9a is the schematic representation of this method. Two graphite electrodes are separated by approximately 1mm. A direct current of 50 to 100 A driven by approximately 20 V creates a high temperature discharge between the two electrodes. The temperature in the inter-electrode plasma region is high (around 4000 K). The high temperature plasma between the two rods causes sublimation of graphite. Nanotubes self-assemble from the resulting carbon vapor and are deposited on one of the graphite rods. The positive electrode is usually sublimated and consumed. Therefore, the anode has to be continuously moved forward to keep a constant distance between the electrodes. The synthesized nanotubes have lengths on the order of ten microns and diameters in the range of 5-30 nm. The nanotubes are typically bound together by strong Van der Waals interactions to form tight bundles. Nanotubes produced by this method are usually straight, indicative of their high crystallinity. Fullerenes, amorphous carbon and graphite are also produced on the reactor wall as by-products. Therefore, it is a technique that produces a mixture of components and requires separating nanotubes from the soot in the crude product.

In the laser ablation technique, a high-power laser beam is used to vaporize a graphite target in an oven at 1200 ℃ (see Fig. 1-9b). The oven is filled with helium or argon gas at a pressure of 500 Torr. A water cooled surface is included in the system to collect the nanotubes. The nanotubes develop on the cooler surface of the reactor, as the vaporized carbon condenses. The reactions probably occur with the similar mechanism of growth of carbon nanotubes as in an arc discharge. Laser ablation produces a small amount of clean nanotubes, whereas arc discharge methods generally produce large quantities of impure materials.

The catalyst assisted chemical vapor deposition of carbon nanotubes is essentially a two-step process consisting of a catalyst preparation step followed by the actual synthesis of nanotubes [*Li et al.*, 1996]. A substrate is first coated with a layer of transition metal catalyst particles. The catalyst is generally prepared by sputtering a transition metal onto a substrate and then using either etching or thermal annealing to induce catalyst particle nucleation. Thermal annealing results in cluster formation on the substrate, from which the nanotubes will grow. A schematic experimental setup for CVD growth is depicted in Fig. 1.9c. The general nanotube growth mechanism in a CVD process involves the decomposition of carbon-containing molecules, and saturation of carbon atoms at the edge of catalyst particles. The catalyst nanoparticles (the dark circle and half circle in Fig. 1.10) generally stay at the tips of the growing nanotubes during the growth process, although in some cases they remain at the nanotubes base, depending on the adhesion between the catalyst and the substrate. The precipitation of carbon from the saturated metal particle leads to the formation of tubular carbon solids having sp^2 structure. Tubule formation is favored over other forms of carbon such as graphitic sheets with open edges. This is because a tube contains no dangling bonds and therefore is in a low energy form. Most of the CVD methods

employ ethylene or acetylene as the carbon feedstock and the substrate growth temperature is typically in the range of 700-900 ℃. Iron, nickel or cobalt nanoparticles are often used as catalyst. The rationale for choosing these metals as catalyst for CVD growth of nanotubes lies in the phase diagrams for the metals and carbon. At high temperatures, carbon has finite solubility in these metals, which leads to the formation of metal-carbon solutions and therefore the aforementioned growth mechanism. In general, the CVD method results in poorer quality carbon nanotubes having a wide diameter range. However, the CVD method is relatively easy to scale up, which could be advantageous for commercial production.

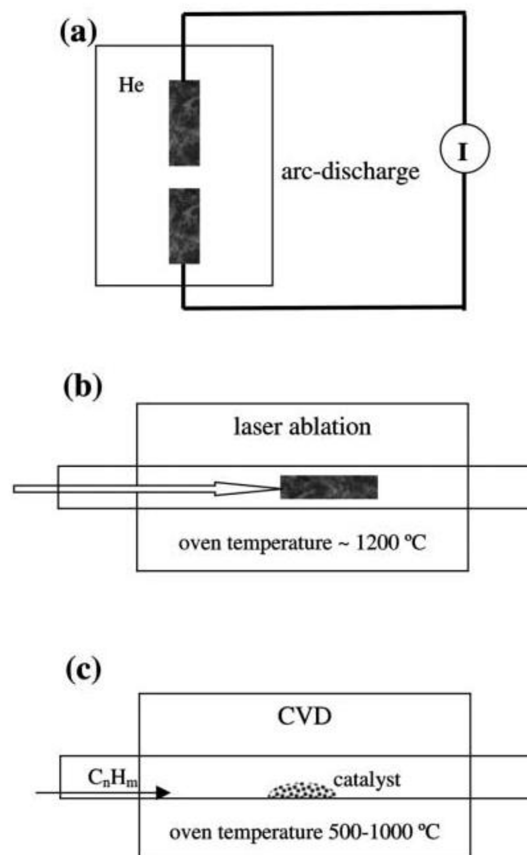

Figure 1.9: Schematic experimental setups for nanotube growth method: (a) arc-discharge method, (b) laser ablation method, and (c) catalyst-assisted CVD method. [*Dresselhaus et al.*, 2001]

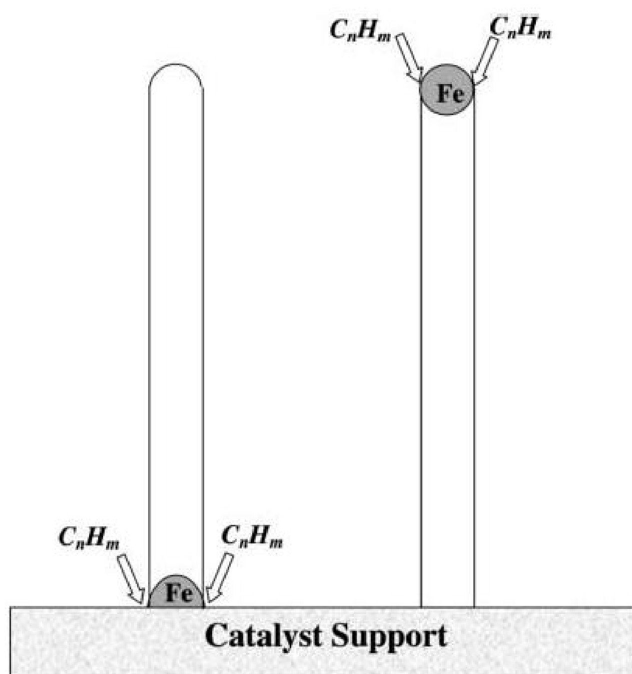

Figure 1.10: Two general growth modes of nanotube in catalyst –assisted chemical vapor deposition. Left: base growth mode. Right: tip growth mode. [*Dresselhaus et al.*, 2001]

1.6 Plasma

Plasma is a partially or fully ionized gas containing charged particles (electrons, ions, negative ions, etc.) and neutral particles (atoms, molecules, etc.). Normally a plasma is charge neutral. Plasma is often called the fourth state of matter [*Chen*, 1984; *Lieberman* and *Lichtenberg*, 1994]. A solid substance in thermal equilibrium generally passes into a liquid state as the temperature is increased. The liquid passes into a gaseous state as the temperature is further increased. At a sufficiently high temperature, the molecules in the gas decompose to form a gas of atoms that move freely in random directions, except for infrequent collisions. If the temperature is further increased, the substance starts to be ionized and therefore enters the plasma state. This state is usually characterized by a

common charged particle density n_e (electron density) ≈ n_i (ion density) and, in equilibrium, a temperature T_e (electron temperature in eV) = T_i (ion temperature in eV) = T. (Room temperature 297 K is equivalent to $T \approx 0.026$ eV.) The temperatures required to form plasmas from pure substances in thermal equilibrium range roughly from 4000 K for easy-to-ionize elements like cesium to 20000 K for hard-to-ionize elements like helium. The fractional ionization of plasma is defined as

$$x_{iz} = \frac{n_i}{n_g + n_i} \quad , \tag{1-2}$$

where n_g is the neutral gas density and n_i the ion density. For weakly ionized plasmas, $x_{iz} << 1$, and for highly ionized plasmas, $x_{iz} \approx 1$.

Much of the matter in the universe is in the plasma state. Stars, as well as most interstellar matter, are in plasma state. While stars are plasmas in thermal equilibrium, the light and heavy charged particles in low-pressure processing discharges are almost never in thermal equilibrium, neither among themselves nor with their surroundings. Because these discharges are electrically driven and are weakly ionized, the applied electric power preferentially heats the mobile electrons, while the heavy ions efficiently exchange energy by collisions with background gas. Hence, $T_e >> T_i$ for these plasmas.

Electron density and temperature are two important parameters of a plasma. Figure 1.11 illustrates the wide range of electron densities and temperatures that are encountered in natural and laboratory plasmas (note the logarithmic scales used). Among those laboratory plasmas, two types of discharges are particularly important for plasma processing, namely, low- and high- pressure discharges.

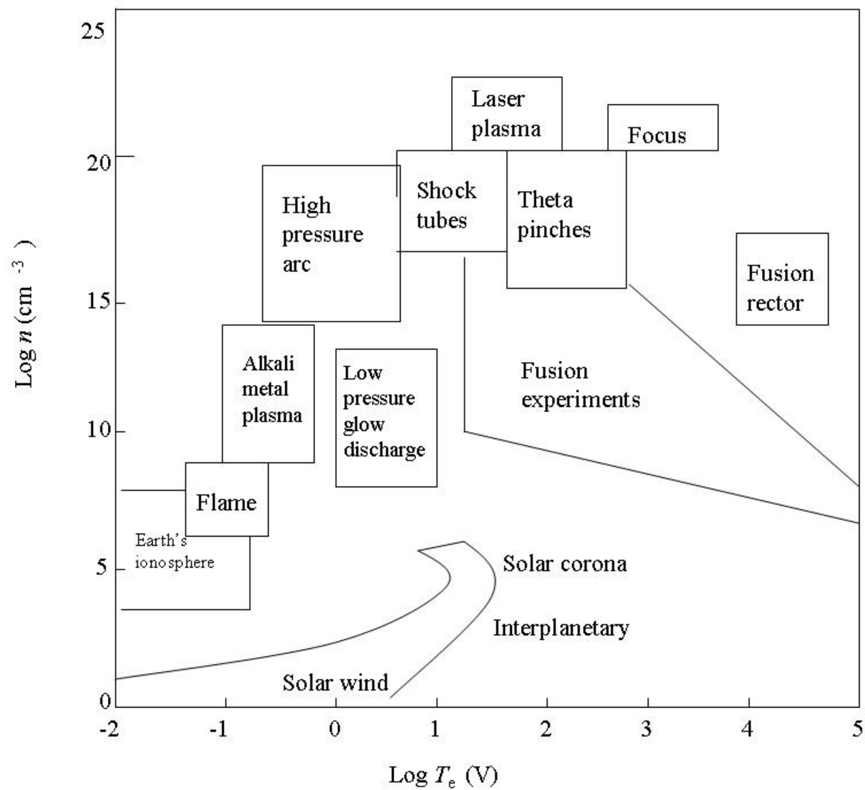

Figure 1.11: Space and laboratory plasmas on log n versus $\log T_e$ scales. [*Lieberman* and *Lichtenberg*, 1994]

Low-pressure discharge plasmas are characterized by $T_e \approx$ 1-10 eV, $T_i << T_e$ and $n \approx 10^8 - 10^{13}$ cm^{-3}. In these discharges, the plasma itself, as well as the plasma-substrate system, is not in thermal equilibrium, which enables substrate temperatures to be relatively low (compared to those temperatures required in a conventional thermal process), while maintaining adequate deposition rates or etching rates due to high temperature plasmas. Although n_i and n_e may be five orders of magnitude lower than n_g in low pressure processing plasmas, the charged particles play central roles in sustaining the discharge and in processing. Because $T_e >> T_i$, it is the electrons that dissociate the feedstock gas to create the free radicals, the etchant atoms, and deposition precursors required for chemical processes at the substrate. Electrons also ionize the gas to create the positive ions that subsequently bombard the substrate. Energetic ion (either

positively charged or negatively charged) bombardment can increase chemical reaction rates at the surface, clear inhibitor films from the surface, and physically sputter materials from or implant ions into the surface. While energy is delivered to the substrate also, e.g., in the form of bombarding ions, the energy flux serves to promote the chemistry at the substrate, rather than to heat the substrate. The gas pressures for these discharges are low: $p \approx 1$ mTorr - 10 Torr. In this thesis work, the plasma used to facilitate diamond deposition and to sputter thin catalytic nickel films for the deposition of Ni catalyst or aluminum on substrates belongs to this type.

High-pressure plasma (~ 1 atm) has lower electron temperature, $T_e \approx$ 0.1-2 eV, but higher plasma density, $n \approx 10^{14}$ - 10^{19} cm^{-3}. The light and heavy particles are nearly in thermal equilibrium, with $T_i \leq T_e$. These discharges are used mainly to deliver heat to the substrate, e.g., to increase surface reaction rates, to melt, sinter, or evaporate materials, or to weld or cut refractory materials.

1.7 Plasma sheath

One of the most important concepts in the description of electrical discharges is the idea of a sheath region surrounding any surface in contact with the plasma. When a positive charge is introduced in the plasma, electrons will be drawn towards it and form an electron cloud surround the charge. Therefore, the influence of the charge is limited to a short distance termed the Debye length. This shielding effect is called Debye shielding in plasma physics. Suppose there is no appreciable electric field inside the plasma: when ions and electrons hit the wall, they recombine and are lost. Since electrons have much higher thermal velocities than ions, they are lost faster and leave the plasma with a net positive charge. The plasma must then have positive potential with respect to the

wall. This potential cannot be distributed over the entire plasma, since Debye shielding will confine the potential variation to a layer of the order of several Debye lengths in thickness. This layer, which must exist on all cold walls with which the plasma is in contact is called a "sheath". The function of a sheath is to form a potential barrier so that the more mobile species, usually electrons, is confined electrostatically. In the following, the physics of plasma sheath is explained in detail.

The bulk plasma, which is quasi-neutral (if singly ionized, $n_i \approx n_e$), is joined to wall surfaces across thin positively charged layers called *sheaths* [*Chen*, 1984]. The electron thermal velocity, $\sqrt{\frac{kT_e}{m}}$, is at least 100 times the ion thermal velocity, $\sqrt{\frac{kT_i}{M}}$, because $m \ll M$ and $T_e \gg T_i$ (for low pressure discharge cases), where k is the Boltzmann constant, and m and M are the electron and ion masses, respectively. Let us consider a slab plasma of width l with $n_i = n_e$ confined between two grounded (potential $\Phi = 0$) absorbing walls (Fig. 1.12a). In the bulk plasma, the net charge density $\rho = e(n_i - n_e)$ is nearly zero and the electric field E_x is also zero. Hence, the fast-moving electrons are not confined and will rapidly be lost to the walls. Some electrons near the walls are lost, leading to the situation, shown in Fig. 1.12b, where thin ($s \ll l$) positive ion sheaths form near each wall in which $n_i \gg n_e$. A net positive charge density ρ within the sheaths forms in these regions such that $\Phi(x)$ is positive within the plasma and falls sharply to zero on both walls. The electric fields within the sheaths point from the plasma to the wall. Thus the force $-eE_x$ acting on electrons is directed into the plasma. This acts as a potential energy “well” for containing electrons and a “hill” for accelerating ions to the walls. If the plasma potential (with respect to the walls) is V_p, then we can expect that $V_p \sim$ a few T_e in order to confine most of the electrons. The

energy of ions bombarding the walls is then a few times T_e. Although the electron temperature T_e may be two orders of magnitude larger than the ion temperature T_i, the energy of ions bombarding the substrate can reach the electron energy. If the substrate is biased negatively with respect to the plasma, this energy can be as high as several keV, much exceeding T_e. The acceleration of low-temperature ions across a thin sheath region where the plasma and substrate meet is central to all processing discharges.

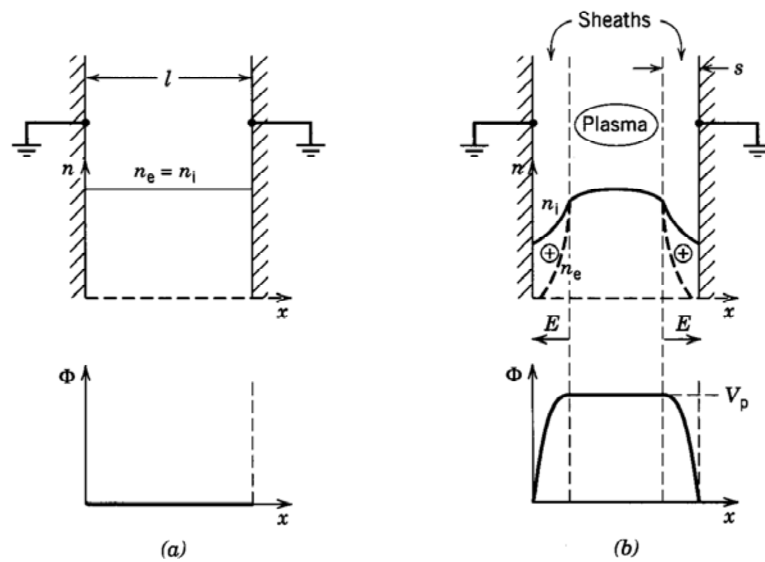

Figure 1.12: The formation of plasma sheaths: (a) initial ion and electron densities and potential; (b) densities, electric field, and potential after formation of the sheath. [*Lieberman* and *Lichtenberg*, 1994]

1.8 Motivation and organization of thesis

The main goal of this thesis is to realize controlled synthesis of various carbon-based materials with desired properties. Experimental factors including substrate biasing, substrate pretreatments, catalyst coating and so on, play important roles in controlling

the nucleation and growth of carbon-based materials. In this thesis, the effects of different processing factors on nucleation and growth of carbon based materials were systematically investigated. This work has led to a comprehensive understanding of how each experimental parameter affects carbon-based materials growth. Optimization of experimental conditions based on this understanding is beneficial for the controlled synthesis of carbon-based materials with desired properties: for example, nanocrystalline diamond films with smooth surfaces grown under a high gas flow rate with positive substrate biasing, well-aligned carbon nanotubes or carbon nanocones by glow discharge under negative substrate biasing, or deposition of high quality diamond at low substrate temperatures using graphite etching technique.

The outline of this thesis is as follows. A brief introduction to carbon allotropes and their properties and applications, synthetic techniques for diamond and carbon nanotubes, physics of plasma and plasma sheath has been given in this Chapter. The rest of this thesis is organized as follows.

Chapter 2 contains explanations of experiment methodologies adopted in this thesis. Two CVD reactors (hot filament CVD reactor with glow discharge capabilities and microwave plasma CVD reactor) used for synthesis of the carbon based materials will be described in details. Also, the techniques used to characterize the samples will be described.

Chapter 3 presents the results of studies on the effects of substrate biasing in a hot filament reactor on the nucleation and the growth of diamond, carbon nanocones, and carbon nanotubes. It has been observed that positive biasing increases the diamond nucleation density. In the case when a negative bias is applied to the substrate to initiate a glow discharge, the growth direction of carbon nanotubes or carbon nanocones varies gradually from the edge to the center of the substrate. The electric field in the plasma

sheath region has been singled out as the main candidate responsible for aligned nanotube (or nanocone) growth.

In Chapter 4, results of investigations of the effect of the carbon source on diamond deposition in a microwave plasma reactor will be presented. In this study, a new diamond deposition method by graphite etching was developed. Synthesis of high quality diamond under unusually low substrate temperature (350 ℃) has been realized by this method. In addition, the graphite etching method was adopted for experiments on diamond deposition on a steel substrate using a hot filament reactor. High quality diamond film has been successfully deposited on aluminum-coated steels using the graphite etching method.

Chapter 5 presents results of studies on the effects of gas flow rate on diamond deposition using a microwave chemical vapor deposition reactor. Results show that high gas flow rate significantly increases the diamond nucleation density and results in nanocrystalline diamond films. The synthesis of nanocrystalline diamond with a smooth surface grown under high gas flow rate is beneficial for optical and mechanical applications of diamond films.

In this thesis, the main research stream is the synthesis of carbon-based materials. In addition, experiments for the synthesis of tungsten and tungsten oxide nanorod films in the hot filament reactor were also performed. In Chapter 6, applications and synthetic techniques of tungsten nanorods will be introduced. Our experiment and results will be presented. Our results show that the synthesis of high purity tungsten or tungsten oxide nanorod films is possible by optimizing the tungsten filament temperatures.

Finally, the main results of the thesis work are summarized in Chapter 7 with some suggestions for future work.

Chapter 2

Plasma reactors and sample characterization techniques

Two CVD reactors were used for the synthesis of carbon-based materials: a hot filament CVD reactor and a microwave CVD reactor. In this Chapter, detailed description of these CVD reactors is given. Also, various material characterization techniques were employed to characterize samples in this thesis. In this Chapter, principles and descriptions of the main techniques are given in detail.

2.1 Hot filament CVD reactor

Figure 2.1 shows the schematic diagram of the hot filament CVD (HFCVD) reactor used in the present study. The HFCVD reactor (image shown in Fig. 2.2) consists of a main vacuum chamber, a gas supply and pumping system, and electrical system. A cross-shaped glass tube with a diameter of 15 cm is used as the vacuum chamber. The vacuum system consists of a diffusion pump backed by a rotary pump. A two-channel gas flow controller, combined with a needle valve in the pumping line controls the mixture of gases and the pressure in the chamber. The gas mixture is guided with a stainless steel tube directly to the top of the reaction chamber.

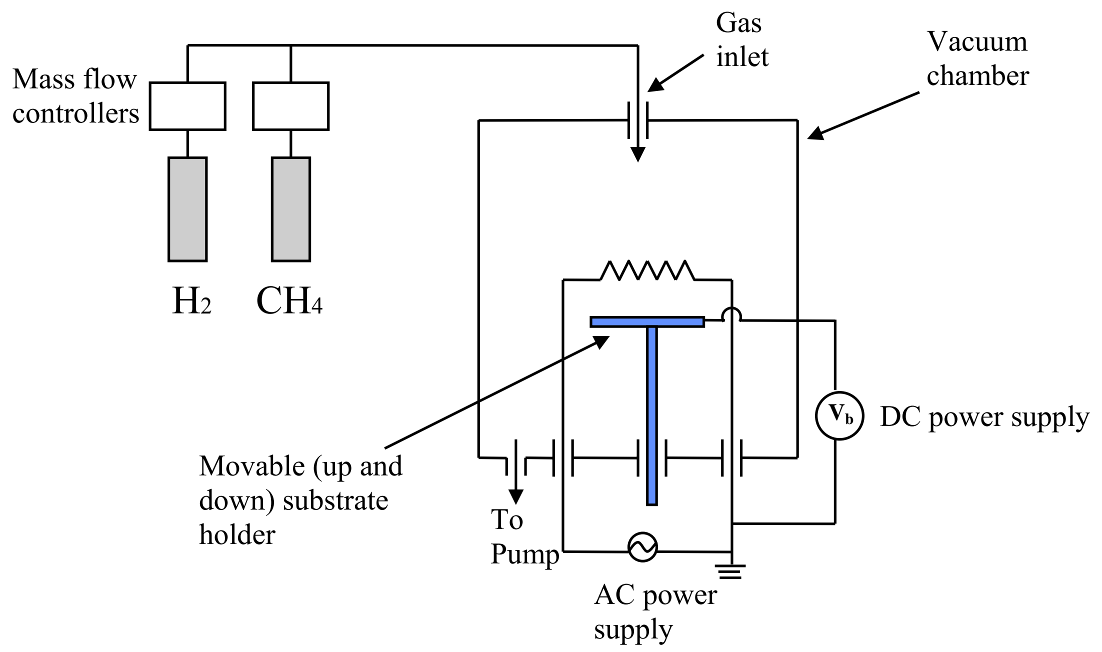

Figure 2.1: Schematic diagram of the HFCVD system.

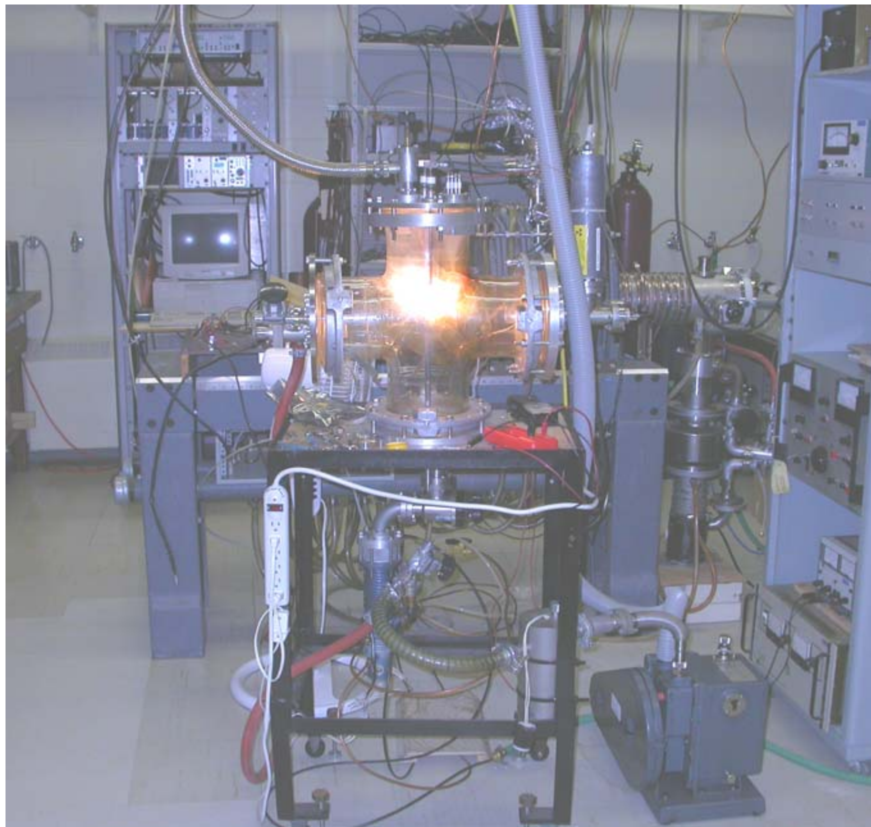

Figure 2.2: A picture of the HFCVD system.

The hot filament in the CVD reactor is a tungsten coil 4 mm in diameter and 4 cm in length. The tungsten wire is 0.3 mm thick and the number of turns is normally 10. The tungsten wire filament is connected to a power source and is Ohmically heated. This provides the thermal energy required for dissociation of the processing gases. An optical pyrometer is used to measure the filament temperature during thin film deposition. A cooling fan is positioned around the chamber to dissipate the heat produced by the filament during growth. The substrate temperature was measured using a thermocouple attached to the substrate holder. As an option, a dc bias voltage could be applied between the filament and the substrate holder for creating a glow discharge or for biasing the substrate without actually breaking down the gas.

2.2 Microwave CVD reactor

Figure 2.3 shows a picture of the microwave plasma CVD reactor used in this thesis. It is an ASTEX-type custom designed 2.45 GHz single mode cavity reactor (Plasmionique, MW-PECVD 1250UOS). The reactor consists of a vertically oriented stainless steel chamber of 140 mm in inner diameter and a microwave source providing up to 1.2 kW (Sairem, model GMP 12 KE/D). The double-wall design allows effective cooling using flowing water. The stainless steel substrate holder of diameter 122 mm is concentric with the reactor chamber. The substrate holder is electrically floating, so a biasing voltage can be applied to it. The substrate holder can be moved vertically to control, in conjunction with various matching tuners, the distance between the substrate and the plasma ball and to minimize the reflected microwave power.

Figure 2.3: A picture of the microwave plasma CVD reactor.

Figure 2.4 shows the schematic of a microwave plasma reactor. This design uses a microwave generator and rectangular waveguide, with a mode converter to convert the TE_{10} (transverse electric) mode in the rectangular waveguide to a TM_{01} (transverse magnetic) mode in the cylindrical waveguide (the reactor vessel). A moveable antenna is used to maximise energy coupling between the two waveguide sections. The cylindrical waveguide is terminated by the metallic substrate holder. This section forms

a ‘cylindrical resonant cavity’. A plasma is produced in the region(s) where the local electric field is strongest. The substrate holder can be moved vertically to adjust the cavity geometry and to minimize, in conjunction with various matching tuners, the reflected microwave power. In reality, reactors are internally far more complex than simple cylinders due to the presence of service ports, welds, diagnostic probes and so on. In general it is only possible to predict the electromagnetic field structure, and hence the plasma location, by numerical solution of Maxwell’s equations within the entire reactor volume, as shown in the modelling work of Funer *et al.* [*Funer et al.*, 1995].

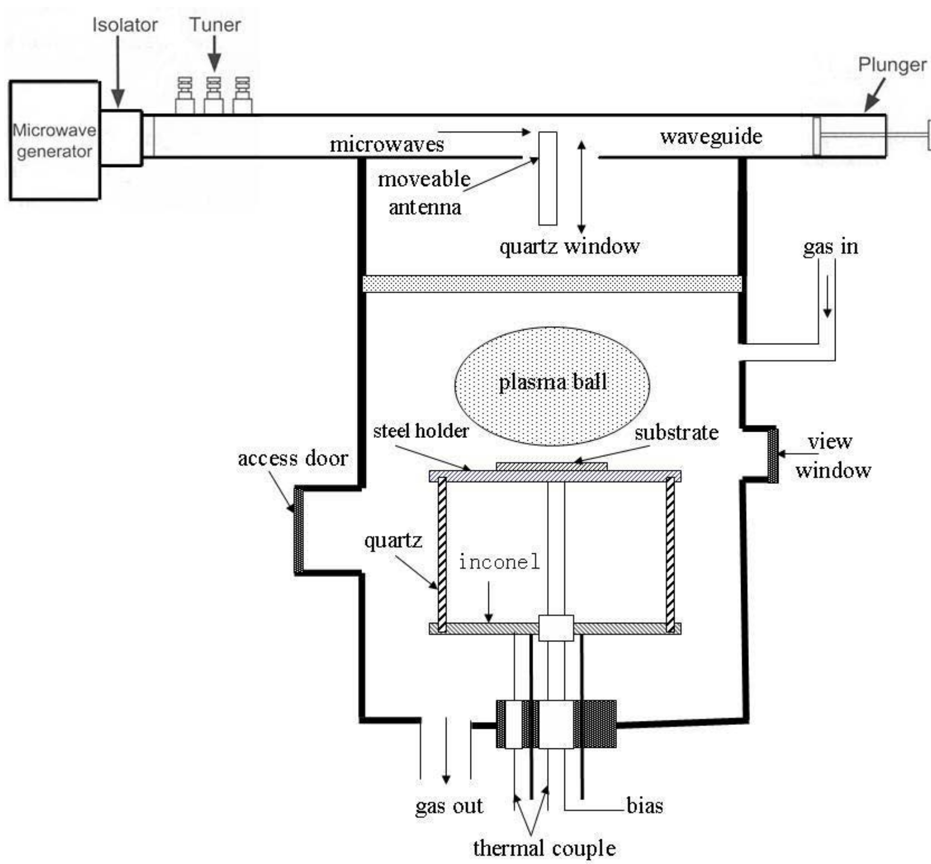

Figure 2.4: Schematic diagram of the microwave CVD reactor.

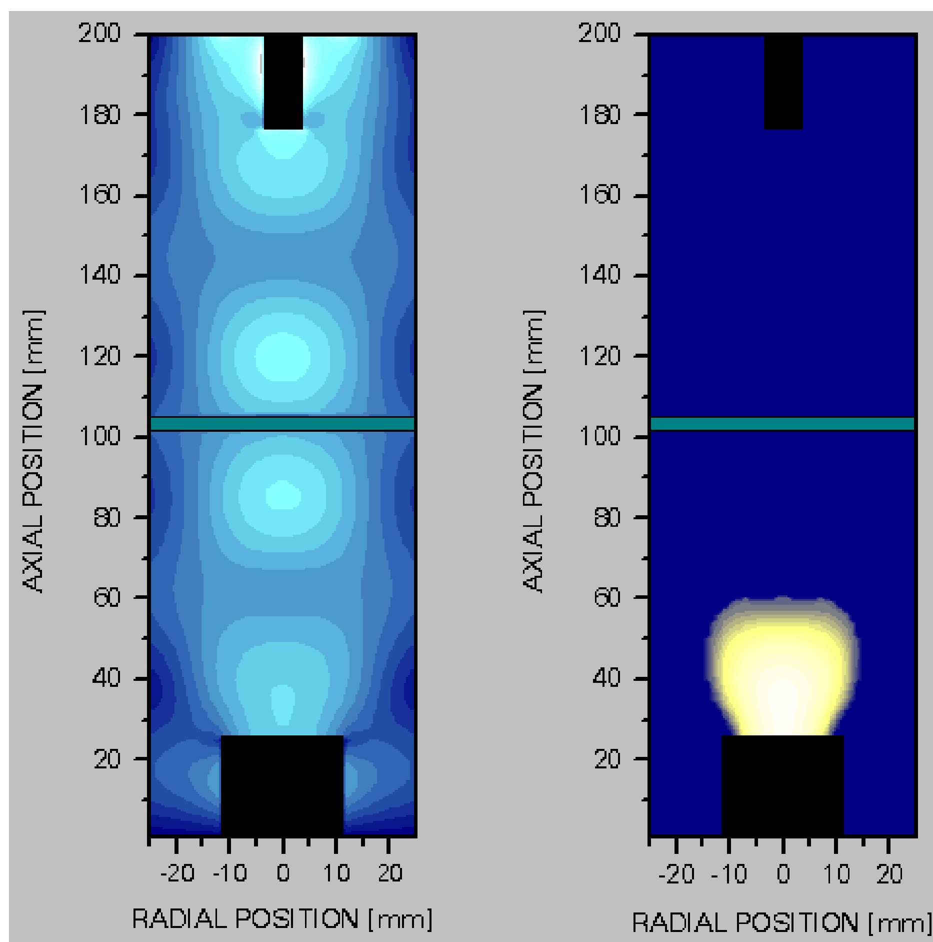

Figure 2.5: Reactor modelling by Funer *et al* [*Funer et al.*, 1995]. The diagram on the left shows the calculated electric field strength in the reactor, while that on the right shows the calculated plasma location. The bar through the centre of the reactor represents the position of the quartz window.

The flow rates of the selected reactant gases can be accurately controlled by a multi-channel mass flow controller and the mixed gas is effused into the reactor through two gas diffuser rings. Each gas diffuser ring consisted of 8 small holes of 0.8 mm in diameter. The distribution orifices are evenly distributed axially on the inner chamber wall. Under optimized conditions, an excited spherical plasma ball is located about 5

mm above the substrate holder. The substrate holder is usually located 50 mm below the top gas diffuser and 30 mm above the bottom gas diffuser.

2.3 SEM

Scanning electron microscopy (SEM) is one of the most widely used surface characterisation techniques. A detailed explanation of the technique of SEM can be found in [*Flewitt* and *Wild*, 1994; *Wachtman*, 1993]. SEM, as its name suggests, uses the quantum mechanical wave nature of electrons, instead of light waves, to image a sample. The electrons are generated by thermionic emission from a metal filament, and accelerated to ~20 keV. A system of electrical and magnetic field 'optics' is used to focus the electron beam at a spot on the sample surface. The focused electron beam is scanned over the surface of a specimen in a raster pattern via magnetic scan coils. The incident energetic electron beam results in several reflected emissions including backscattered electrons, secondary electrons, or X-rays (see Fig. 2.6). The current of electrons reflected from the surface is collected, amplified, and plotted as a two-dimensional 'micrograph' image on a cathode ray screen by mapping the signal intensity as a function of position. The image has a large depth of focus so that the entire surface of a specimen with high relief is in focus. This is an important advantage of SEM over optical microscopy. While visible light has wavelengths between 4000 and 7000 Å, electrons accelerated to 20 keV have a de Broglie wavelength of 0.6 Å, so electron microscopes have much higher spatial resolution than optical microscopes. Typical spatial resolution of a 20 keV SEM is about 3 nm. Also, chemical composition analysis of a micro-volume of a sample is possible through energy analysis of the emitted X-rays. Preparation of samples for SEM observation is relatively easy since

most SEMs only require that samples to be conductive in order to prevent charge accumulation on the sample. The combination of larger depth of focus, greater resolution, and ease of sample preparation makes the SEM one of the most heavily used instruments in many research areas today. The limitation of SEM is that the sample surface must be electrically conducting, otherwise the electron beam would charge up the surface. For an insulating material, the sample is given a thin (~10 nm) Au coating by glow discharge sputtering before SEM examination. Also, SEM must be carried out under a high vacuum (10^{-6} Torr or better).

In the work presented in this thesis, SEM was used to give information on the appearance, or morphology, of the sample surface. Also, by studying the SEM image of the cross section of the sample, the thin film thickness can be measured. This allows determining the growth rate of the film, knowing the duration of time needed for film growth. In this thesis, a high resolution SEM (20 kV, JSM 840A) was used for SEM imaging.

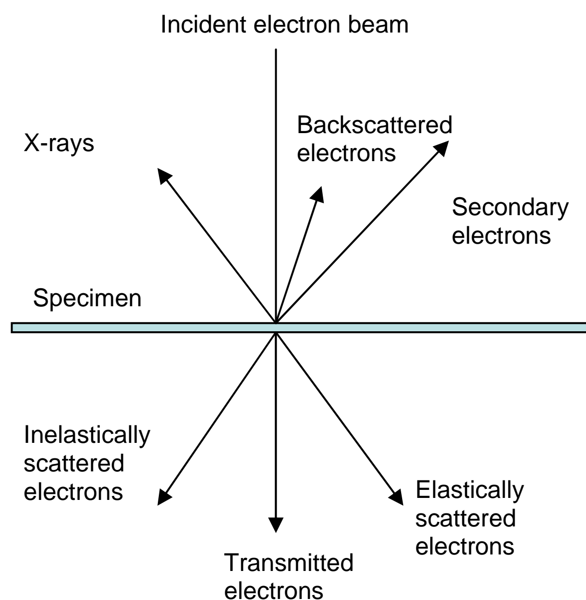

Figure 2.6: Emitted particles and photons from a specimen due to the incident electron beam in a scanning electron microscope. [*Wachtman*, 1993]

2.4 Raman spectroscopy

Raman spectroscopy is a technique to identify and characterize the chemical structure of materials. When an electromagnetic wave is incident on material, it is scattered by electrons bound to molecules either elastically or inelastically. Elastic scattering (Rayleigh scattering) involves no change in the frequency while in inelastic scattering, the scattered wave has a frequency either lower (Stokes Raman scattering) or higher (anti-Stokes Raman scattering) than the frequency of the incident light. The frequency difference corresponds to the molecular vibrational resonance frequency specific to the sample by which sample identification can be made. In micro Raman spectroscopy, the incident light is focused to a diameter as small as 1 micrometer corresponding to the spatial resolution of the measurement.

Raman spectroscopy is a useful technique for the identification of a wide range of substances - solids, liquids, and gases. It is a straightforward, non-contact, non-destructive technique requiring no sample preparation.

In Raman spectrometers, lasers are used as a photon source due to their highly monochromatic nature, and high intensity. This is necessary, as the Raman scattering cross-section is low. Typically the Stokes lines (scattered light with wavelength shift) are ~ 10^5 times weaker than the Rayleigh scattering (scattered light without wavelength shift). Most Raman spectrometers for material characterisation use a microscope to focus the laser beam to a small spot (<1-100 μm diameter). Light scattered from the sample passes back through the microscope optics into the spectrometer. Raman shifted radiation is detected with a charge-coupled device (CCD) detector, and a computer is used for data acquisition and curve fitting.

In this thesis, a micro-Raman (Renishaw 2000) system operated at the argon laser wavelength of 514 nm was mainly used to characterize the diamond and other carbon-based materials. In the following, typical diamond Raman spectra are presented as an example of the application of Raman spectroscopy.

Natural diamond exhibits one main Raman active vibration scattering peak which manifests itself as a sharp first order peak in the Raman spectrum at ~1333 cm^{-1} in natural diamond and a weak second order feature at ~2750 cm^{-1} [*Solin* and *Ramdas*, 1970]. A Raman spectrum taken from a natural diamond sample, showing the first order peak, is presented in Fig. 2.7. The full-width at half maximum (FWHM) of the peak is typically ≤2 cm^{-1}.

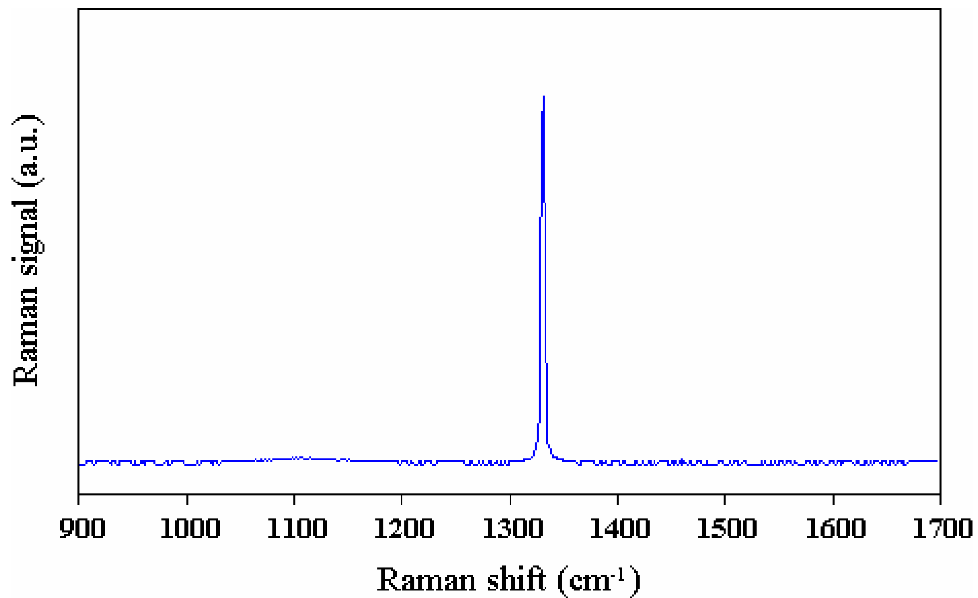

Figure 2.7: Raman spectrum of natural diamond (type IIa), showing the main Raman active mode at ~1332 cm^{-1} (taken using 514 nm laser excitation wavelength). [http://www.chm.bris.ac.uk/]

In diamond films grown by CVD, carbon is also incorporated into the film in non-diamond forms. These non-diamond carbons may be graphitic [*Zhu et al.*, 1989] or

amorphous carbon [*Nemanich et al.*, 1988] in the film. The Raman spectrum of an infinite crystal of pure graphite (or a large single crystal sample, in practice) would show one sharp peak at 1580 cm^{-1} [*Nemanich et al.*, 1988; *Tuinstra* and *Koenig*, 1970]. For small crystallite sizes, the selection rules concerning the Raman activity of certain phonons in infinite graphite crystals are relaxed as the crystal can no longer be regarded as infinite. The sharp graphite peak becomes a broad band (the G-band) and a 'disordered' (or D-band) peak appears in the spectrum at ~1350 cm^{-1} [*Tuinstra* and *Koenig*, 1970] (see Fig. 2.8). Amorphous carbon produces a broad asymmetric hump in the region 1000-1600 cm^{-1} [*Yoshikawa et al.*, 1988]. Both graphite and amorphous carbon have Raman scattering efficiencies greater than that of diamond. This means that for identical numbers of sampled atoms in the three carbon forms - diamond, graphite, and amorphous carbon, the graphite and amorphous carbon samples would give a much stronger Raman signal than the diamond sample. These scattering efficiency ratios, relative to diamond have been reported to be ~50 times for graphite [*Wada* and *Solin*, 1981], and ~233 times for amorphous carbon [*Sails et al.*, 1996], both measured using 514 nm laser excitation. A Raman spectrum of CVD diamond with nondiamond carbon in the film is shown in Fig. 2.9.

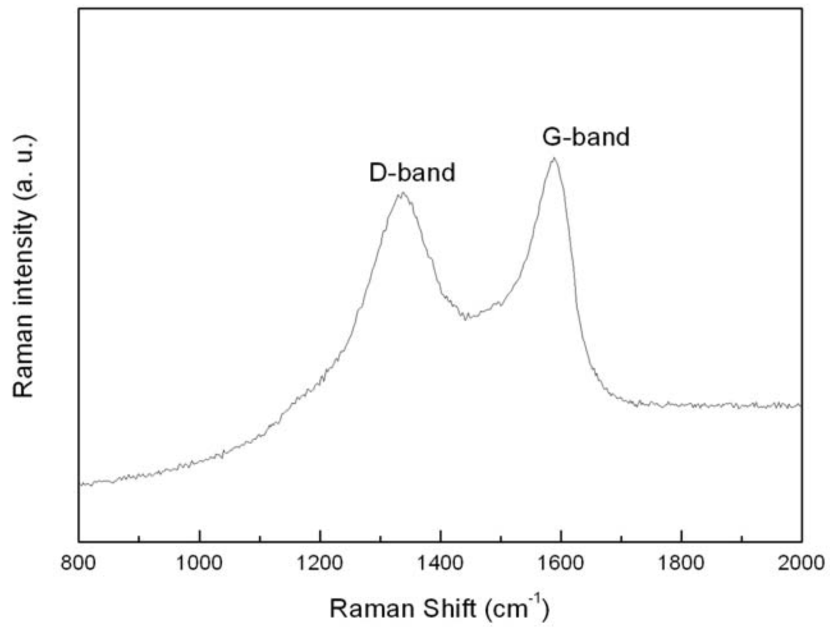

Figure 2.8: Raman spectrum of graphite, showing the D-band and the G-band. Raman spectrum taken using 514 nm laser excitation.

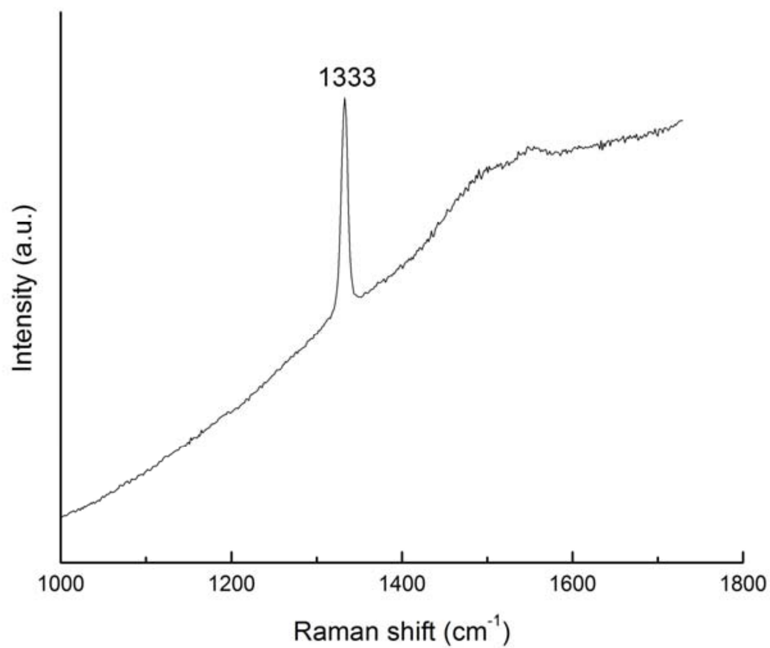

Figure 2.9: Raman spectrum of CVD diamond with non-diamond carbon in the film. Raman spectrum taken using 514 nm laser excitation. The increasing base line is due to amorphous carbon.

A Raman spectrum of CVD diamond film synthesized in this thesis work is shown in Fig. 2.10. A strong, narrow diamond peak, located at around 1333 cm^{-1}, and lack of features attributable to non-diamond carbons indicate that the film is of high quality.

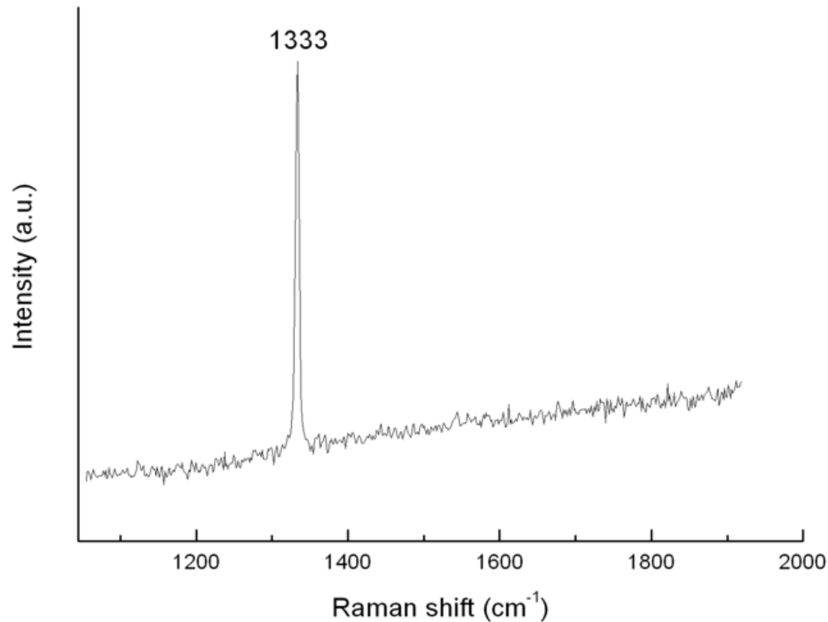

Figure 2.10: Raman spectrum of high quality CVD diamond synthesized in this thesis work. Raman spectrum taken using 514 nm laser excitation.

2.5 XRD

X-ray diffraction (XRD) is a useful analytical technique to identify and characterize unknown crystalline materials. The interplanar spacing in regular crystals is of the order of the wavelength of incident X-ray radiation. Irradiating a crystal with a collimated and mono-energetic X-ray beam gives rise to constructive and destructive interference. Figure 2.11 shows an X-ray beam interacting with two layers of atoms in a crystal. As shown in the diagram, the path difference between the waves reflected at neighbouring lattice layers is $2d\sin\theta$, where θ is the angle between the incident beams and the lattice

planes and d is the distance between two lattice planes. Constructive interference occurs when the path difference is an integer multiple of the incident wavelength. This leads to Bragg's law: $n\lambda=2d\sin\theta$, where λ is the wavelength of the X-rays and n is an integer. When the Bragg conditions for constructive interference are satisfied, a "reflection" is produced, and the relative peak intensity is generally proportional to the number of grains in a preferred orientation. The X-ray diffraction patterns generated by this technique thus provide a structural fingerprint of unknown samples.

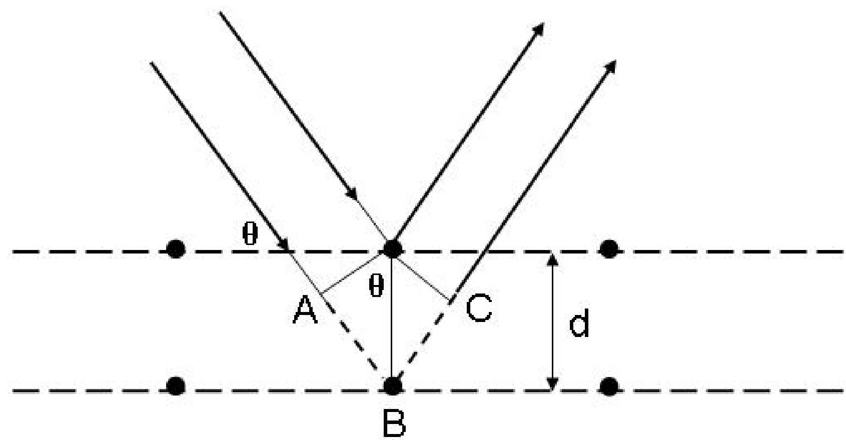

Figure 2.11: Reflection of X-rays from two planes of atoms in a crystal.

XRD measurements were performed using a Rigaku (Rotaflex Ru-200) diffractometer in which X-rays of the Cu K_α line (λ=0.15418 nm), produced by impinging an 80 kV, 40 mA electron beam on a Cu target, was used. The sample and the detector are mounted on two separate rotating bases, when the sample rotates an angle θ, the detector rotates an angle 2θ as shown in Fig. 2.12. The diffracted beam may be detected by a detector such as a Geiger counter. The whole system is controlled by a computer which is also used to store the data from the detector. Data reduction

routines rapidly determine peak position, relative intensities, and calculate intracrystalline d-spacings. The complete powder diffraction file is available for identification of the crystalline structure of the tested material.

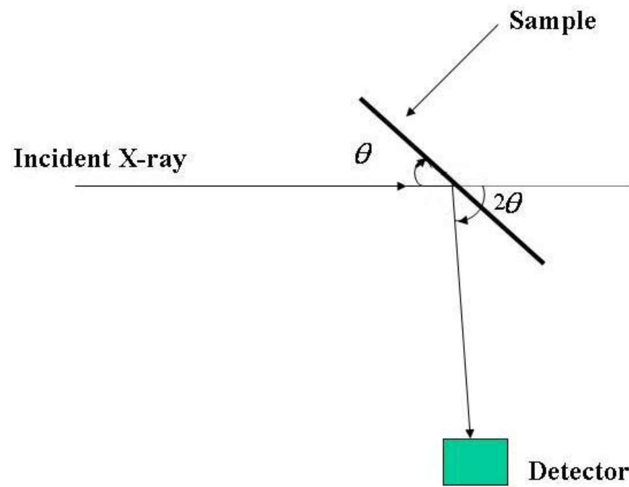

Figure 2.12: Relationship of rotation angles of the sample and detector.

The XRD is a convenient and reliable material characterization technique because of : 1) rapid identification of materials; 2) ease of sample preparation; 3) computer-aided material identification; 4) large library of known crystalline structures.

2.6 AFM

Atomic force microscopy (AFM) is a powerful technique to measure the surface topography with a resolution of sub-nanometer without the need for any additional sample preparation. The AFM consists of a sharp silicon tip (usually 10-20 nm diameter) attached to a cantilever (Fig. 2.13). The tip is brought close to the surface and the sample is scanned beneath the tip. As the tip moves over the surface, the cantilever deforms under interactions between the surface and tip atoms. The deformation of the

cantilever (which obeys Hooke's law) can be directly measured by the displacement of a laser beam reflected from it onto a 2-D photodiode array.

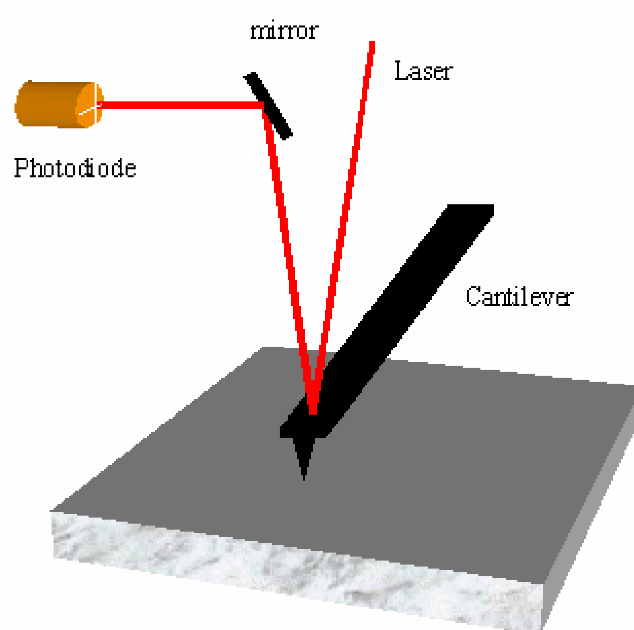

Figure 2.13: Schematic diagram of an AFM.

The atomic force microscope is run in two basic modes: contact mode and tapping mode. In contact mode, the AFM tip is in contact with the surface continuously. The main problem with this method is that the tip can drag over the surface and the lateral forces can distort the surface structure. In tapping mode (also called intermittent contact mode), the AFM cantilever is vibrated above the sample surface, so the tip is only in contact with the surface intermittently. This helps reduce shear forces associated with the tip movement. For most imaging in AFM, tapping mode is the recommended mode.

The major advantages of AFM over other morphology characterization techniques (e.g. SEM) are: 1) Imaging of conducting and non-conducting surfaces down to sub-

nanometer resolution; 2) Imaging in air and liquid, allowing in-situ measurements and real time imaging of biological and chemical processes.

2.7 TEM

Similar to SEM, the transmission electron microscope (TEM) exploits the wave nature of an energetic electron beam. A schematic diagram of the microscope is shown in Fig. 2.14. An electron beam from an electron gun is accelerated typically to 200 keV. TEM uses electromagnetic lenses to focus the electrons into a very narrow beam to a spot of the order of 1 mm. The electron beam then travels through the specimen (e.g. in the form of a thin film). Depending on the density of the material present, some of the electrons are scattered from the beam. At the bottom of the microscope the unscattered electrons hit a fluorescent screen, which gives rise to a "shadow image" of the specimen. The image can be studied directly by the operator or photographed with a camera. The microstructure, e.g., the size, and lattice defects of the specimen can be studied by use of TEM. Figure 2.15 shows a high resolution TEM image of multiwall carbon nanotubes. The size, helicity, number of walls, lattice defects of carbon nanotubes can be studied.

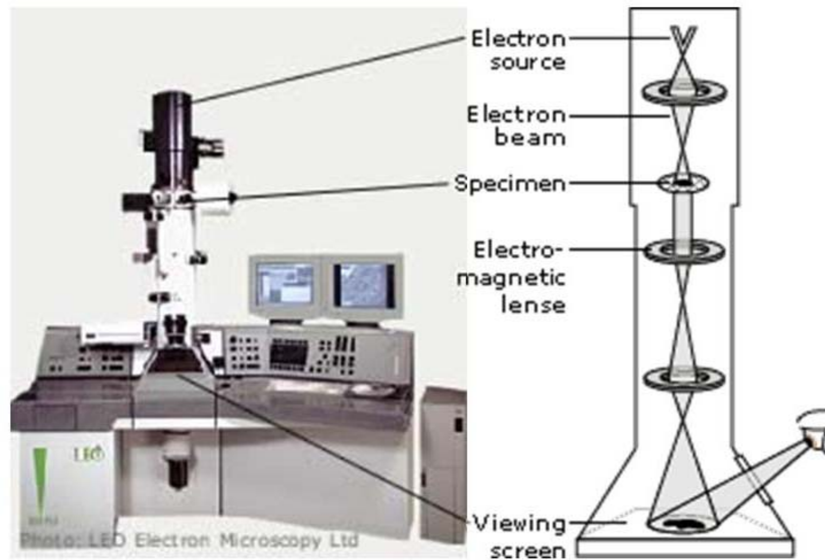

Figure 2.14: Schematic presentation of a TEM [http://nobelprize.org/].

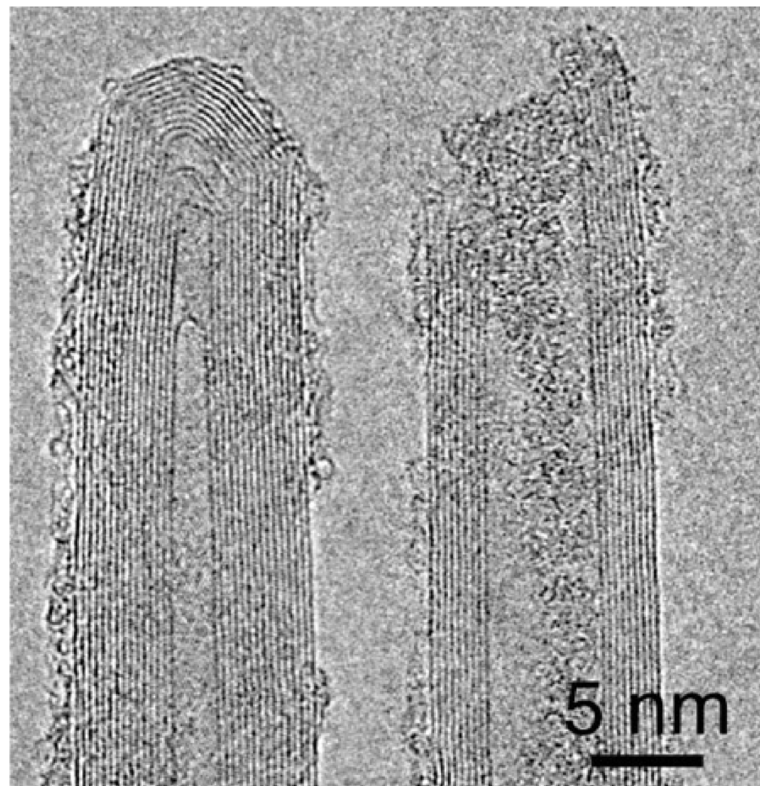

Figure 2.15: Sample TEM images of closed (left) and open (right) multiwall nanotubes [http://physicsweb.org/].

Samples for electron microscopy in form of films mounted on fine-meshed grids are required to be very thin. If near-atomic resolution is required film thicknesses have to be limited to a few tens of Å. Therefore, the quality of the electron microscopy work is sometimes limited by the thinning-down procedure as structural changes may occur during thinning.

To prepare the carbon nanotubes or carbon nanocones specimens for TEM analysis, the deposited film was scratched off from the substrate. First, a solution of the deposit (in the form of powder) and distilled water was prepared. Then, a copper grids (with diameter of 3 mm) was immersed in the solution and well mixed in an ultrasonic cleaner before being taken out of the solution and dried. Finally, the dried samples attached to the grid was analyzed using a TEM device (100 keV, Phillips 410LS).

Chapter 3

Effects of substrate biasing on the growth of carbon based materials

Substrate biasing has significant influence in chemical vapor deposition of carbon-based materials such as diamond and carbon nanotubes. Generally, substrate biasing has been adopted to improve the nucleation density of diamond. Sample deposition with biasing is typically performed in microwave chemical vapor deposition (MWCVD) systems, as reported by several investigators [*Yugo et al.*, 1991; *Jiang et al.*, 1993]. In contrast, only a few investigations have been performed concerning the bias process in hot filament chemical vapor deposition (HFCVD) systems, despite the fact that the scaling up of the processes toward larger deposition areas is far easier compared to an MWCVD system. Also, various biasing conditions (polarity, voltage, and duration) may lead to different results. Furthermore, bias conditions are also critical for controlling the orientation of carbon nanotubes and carbon nanocones. It is, therefore, necessary to study the bias effects in HFCVD system.

Two sets of experiments were designed to investigate bias effects on carbon-based materials growth. First, the effects of bias polarity on carbon-based materials growth on bare silicon substrates were studied. Results show that positive substrate bias with a glow discharge plasma significantly increases the diamond nucleation density and

negative substrate biasing leads to the growth of aligned carbon-based nanocones. In the second project, the silicon substrates were first pre-coated with a thin nickel (Ni) layer and the deposition experiments of carbon nanotubes were performed under various bias conditions similar to experiments performed in the first project. Results show that in all bias conditions regardless of the polarity of bias, carbon nanotubes were deposited on Ni-coated substrates. However, the biasing condition plays an important role on controlling the orientation and alignment of carbon nanotubes. The mechanism of controlling of the orientation and alignment of carbon nanotubes under various biasing conditions was addressed in this study.

3.1 Effects of bias polarity on the growth of carbon-based materials

3.1.1 Introduction

Due to the intrinsically low nucleation density of diamond on silicon, a pretreatment such as substrate bias or substrate scratching of the silicon substrate is necessary to increase the nucleation density of diamond crystallites. Besides methods like scratching with diamond powder, the bias treatment is another efficient technique to increase the nucleation density. Enhanced nucleation density by electron bombardment for positive biasing has been reported [*Cui* and *Fang*, 1996]. Negative biasing was usually adopted in the bias enhanced nucleation (BEN) process which is one of the most promising and effective methods to increase the nucleation density. During the BEN process, the substrate is negatively biased in a methane rich CH_4/H_2 mixture (several percent methane) for 20-60 minutes, followed by a conventional CVD process without biasing

(typically 1% methane or less). Generally, the BEN process results in a high nucleation density (in the order of 10^{10} cm^{-2}) and highly orientated microcrystalline diamond (MCD) [*Jiang et al.*, 1993]. However, different results have been reported when negative bias was applied in the diamond nucleation stage under similar experimental conditions. Heiman *et al.* [*Heiman et al.*, 2001] reported that continuous nanocrystalline diamond (NCD) films instead of MCD films were obtained in a microwave CVD reactor. Jan *et al.* [*Jan et al.*, 1999] fabricated nano-sized conical diamond arrays using BEN in a microwave CVD device. Some researchers also applied continuous (in both nucleation and growth stages) negative bias to the substrates for diamond deposition and this process is termed bias enhanced growth (BEG). Sharda and Umeno [*Sharda* and *Umeno*, 2000] produced NCD films using BEG. Zhou *et al.* [*Zhou et al.*, 2002] fabricated amorphous carbon/NCD composites using BEG in an HFCVD reactor. Huang *et al.* [*Huang et al.*, 2003] deposited MCD using BEG in an MWCVD device. Yugo *et al.* [*Yugo et al.*, 1990] found that negative bias hindered the growth of diamond and completely prevented diamond growth when the magnitude of the negative voltage was higher than 200 V. The above results suggest that various kinds of carbon structures can be obtained by substrate biasing.

In the present study, electric voltages with both polarities were applied to silicon substrates in a HFCVD device to study the effects of substrate biasing. It has been found that, in general, positive bias increases the diamond nucleation density. Also, negative biasing promotes the deposition of dense, well-aligned carbon nanocones.

Carbon nanocones are solid graphitic cones with submicron-scale roots and nanometer-size sharp tips. Carbon nanocones are expected to have low turn-on electric field for field emission applications due to the high geometrical enhancement factor near the tips. The enhanced nucleation density by positive substrate biasing treatment is

consistent with the literature, while the synthesis of well-aligned carbon nanocones under negative biasing in a HFCVD system is not consistent with the literature.

3.1.2 Experiment

The experiments have been performed in a HFCVD system shown in Fig. 2.1. The distance between filament and the substrate was kept at 8 mm (from the bottom of the filament coil to the substrate). A dc bias voltage was applied between filament and substrate holder either for creating a glow discharge or for biasing without glow discharge. To initiate a glow discharge, the bias voltage has to exceed a threshold value (depending on experiment conditions including gas, gas pressure, bias polarity, and the distance between filament and substrate holder) before it is brought back to a desired value to maintain the discharge. Single crystalline Si wafers with a size of $10 \times 5 \times 0.5$ mm^3 are used as substrates. Methane and hydrogen were introduced into the reactor. A series of experiments under different biasing conditions were performed. The typical experimental parameters are as follows: the total flow rate of gases is 35 sccm and the methane concentration ranges from 1.0 to 2.0 vol%. The pressure in the chamber during deposition is set to 3.2-11 kPa (24-80 Torr). The filament current is 9.5-10.5 A. The filament temperature is about 2100 ℃ measured by the optical pyrometer. The substrate temperature is 750 ℃, measured by the thermocouple attached to the substrate holder. For positive bias (substrate holder as anode), the voltage between the filament and substrate holder is around 50 V to maintain a glow discharge current of 100 mA. A higher voltage of approximately 300 V is used for negative bias to maintain a glow discharge current of 100 mA, the same current as for positive bias. The typical deposition time is one hour.

3.1.3 Results and discussion

Figure 3.1 shows top-view SEM images of films deposited on silicon substrates under three biasing conditions: (a) without biasing, (b) positive biasing, and (c) negative biasing. The images show that positive substrate biasing (Fig. 3.1b) significantly increases the diamond nucleation density compared with the case without biasing (Fig. 3.1a). The mechanism of diamond nucleation enhancement by positive bias may be attributed to enhanced electron bombardment on the substrate and growing diamond film surface [*Cui* and *Fang*, 1996].

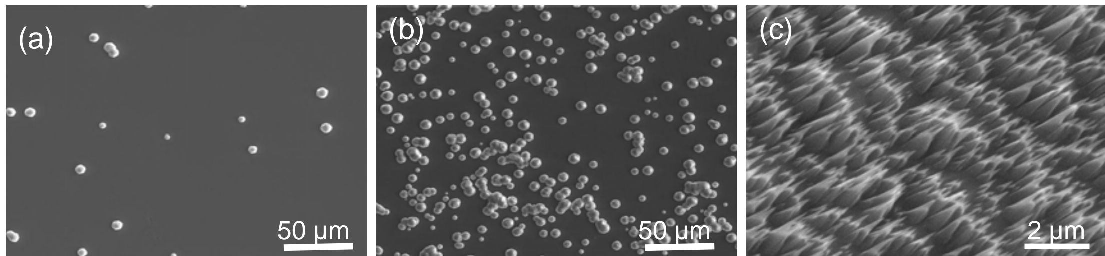

Figure 3.1: SEM images of films with three substrate bias voltages: (a) without biasing, (b) 50 V, and (c) -300 V.

With negative biasing, well-aligned nanocones with various alignment orientations were deposited (Fig. 3.1c). Figure 3.2a shows the cross section SEM image of nanocone films. Figure 3.2b shows the TEM image of a typical nanocone. The solid nanocones consist of submicrometre-sized roots and nanometer-sized tips. The lengths of the nanocones are in the range of a few micrometers. Chemical composition analysis by electron probe microanalysis shows that the nanocones consist of carbon. Raman spectroscopy spectra show two graphitic peaks at around 1350 cm^{-1} (graphitic D-band) and 1580 cm^{-1} (graphitic G-band). It further confirms that the nanocones are graphitic carbon (Fig. 3.3).

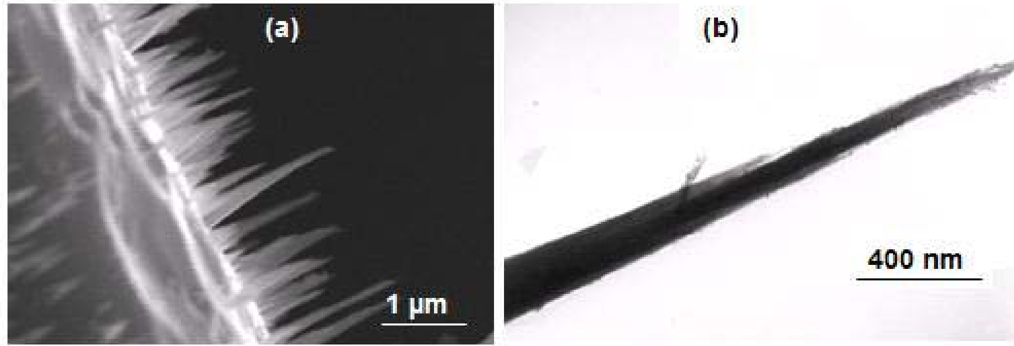

Figure 3.2: (a) Cross section SEM image of nanocone film, (b) TEM image of a carbon nanocone.

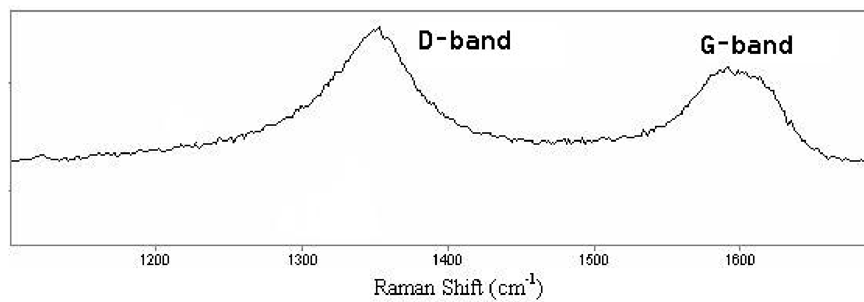

Figure 3.3: Raman spectroscopy of graphitic nanocone.

The fact that the aligned nanocones can be deposited only in a discharge with negative biasing suggests that the nearly unidirectional distribution of carbon-containing ions incident on the substrate may be responsible for the alignment and formation of nanocones, similar to the model proposed by Gamaly and Ebbesen [*Gamaly* and *Ebbesen*, 1995] for the growth of carbon nanotubes. In the experiments with negative biasing, carbon-containing ions and neutrals are the two sources responsible for the carbon grown parallel and perpendicular to the electric field lines. The deposition from neutrals should be isotropic, while the deposition from ions is mainly along the electric field lines. Due to the sharp potential drop in the plasma sheath near the substrate, ions reach high velocities along the direction of the electric field lines toward the substrate. Carbon-containing ions are accelerated toward the substrate at high velocity, and

contribute to the formation of carbon nanocones. The carbon growth along the electric field lines from ions is expected to be much faster than the growth perpendicular to the field lines due to the isotropic growth from carbon-containing neutrals. At the same time, the growing carbon is etched by atomic hydrogen and hydrogen ions. Under simultaneous competition of etching and anisotropic deposition, well-aligned carbon nanocones are formed.

3.1.4 Conclusion

Substrate bias plays an important role in the nucleation and growth of carbon-based film. In this section, effects of the substrate bias polarity on the growth of carbon films in an HFCVD reactor were experimentally investigated. The results show that with a glow discharge, a positive bias increases the diamond nucleation density. With a glow discharge and negative substrate bias, well-aligned graphitic carbon nanocones are formed. The acceleration of carbon ions toward the substrate along the strong local electric field near substrate is believed to be responsible for the growth of the well-aligned graphitic nanocones.

3.2 Substrate bias effect on the orientation control of carbon nanotubes

3.2.1 Introduction

Carbon nanotubes grown by the CVD method are often randomly oriented. Unless made to be aligned, many of their unique properties cannot be fully exploited. In particular, the alignment of CNTs is very important for such applications as scanning probes, sensors, field emitters and nanoelectronics. Several methods for growing aligned CNTs were developed in the last few years. The alignment of the tubes was achieved by: (1) embedding catalyst nano-particles in nanopores [*Li et al.*, 1996]; (2) utilizing very dense tube growth which forces the tubes to align parallel to each other [*Choi et al.*, 2002a]; (3) growth under plasma conditions by application of a bias voltage to the substrate by Ren's group [*Ren et al.*, 1998].

In this PhD work, effects of the substrate biasing on the orientation control of CNTs have been investigated in a hot-filament CVD system. In this study, a thin nickel (Ni) film with a thickness around 20 nm was first deposited on a silicon substrate as catalyst for CNTs growth. CNTs grow from Ni clusters. Our study shows that the alignment orientation of the CNTs appears to be determined by the direction of the local electric field at the sample surface. The method used to grow aligned CNTs is similar to Ren's method. In Ren's study, C_2H_2 and NH_3 gases were introduced to the reactor while NH_3 is a necessary catalyst gas. In the experiments of this thesis, a CH_4 and H_2 gas mixture, which is the typical gas source for CVD diamond growth, was used with Ni as catalyst. Any pretreatment of the surface of the catalyst-metal thin film, e.g., an

exposure to NH_3 gas, or ion etching, is not necessary for growing CNTs in our method [*Yang et al.*, 2003].

It has been pointed out that in a Plasma Enhanced CVD (PECVD) process CNTs are aligned along the electric field [*Hayashi et al.*, 2001; *Bower et al.*, 2000; *Chhowalla et al.*, 2001; *Merkulov et al.*, 2002; *Ono et al.*, 2002]. The bias of the substrate surface with respect to the plasma appears to be the primary mechanism responsible for the alignment of CNTs in a microwave PECVD process [*Bower et al.*, 2000]. Hayashi *et al.* [*Hayashi et al.*, 2001] suggest that forces, exerted to the nanotubes, toward the plasma caused by the local electric field in the sheath and the negative charge at the tips of nanotubes assist CNTs to grow perpendicular to a substrate. Bower *et al.* [*Bower et al.*, 2000] and Chhowalla et al. [*Chhowalla et al.*, 2001] have found that electric field of order of 0.1 V/μm is necessary to completely align the CNTs. Merkulov *et al.* [*Merkulov et al.*, 2002] have further found that the alignment orientation of carbon nanofibers is determined by the direction of the electric field lines. Thong *et al.* [*Thong et al.*, 2002] have found that metal nanowires can be grown from a cold-field-emission CNT (or a tip). By applying a bias voltage to an electrode, the nanowires can grow along the electric field lines towards the electrode and finally contact the electrode. Ono *et al.* [*Ono et al.*, 2002] revealed that the application of a high electrostatic field with a negative substrate bias enhanced the growth of CNTs, while a positive substrate bias suppressed the formation of CNTs. Our experimental results are consistent with those reports and suggest that the strength and the polarity of the electric field play important roles in CNTs alignment. The experiments further revealed that the orientation of aligned CNTs can be controlled by the electric field lines in the plasma sheath by adjusting the gas pressure in the reactor.

3.2.2 Experiments

The CNTs have been grown using a hot-filament CVD reactor to study the biasing effects. P-type (100)-oriented mirror polished Si wafers are used as substrates. A thin nickel (Ni) film, deposited by ion sputtering in an argon plasma discharge in the deposition chamber, is used as catalyst. Figure 3.4 shows the schematic diagram of the ion sputtering coating device for Ni film deposition. In the ion sputtering coating device, the electrons from the hot filament are accelerated by a bias voltage between the hot filament and substrate holder. The collision of these energetic electrons ionizes the argon atoms. Some argon ions are accelerated towards the nickel plate (at a more negative voltage than substrate holder) and cause sputtering of nickel atoms or clusters which eventually arrive at the substrate through diffusion and form a thin film on the substrate.

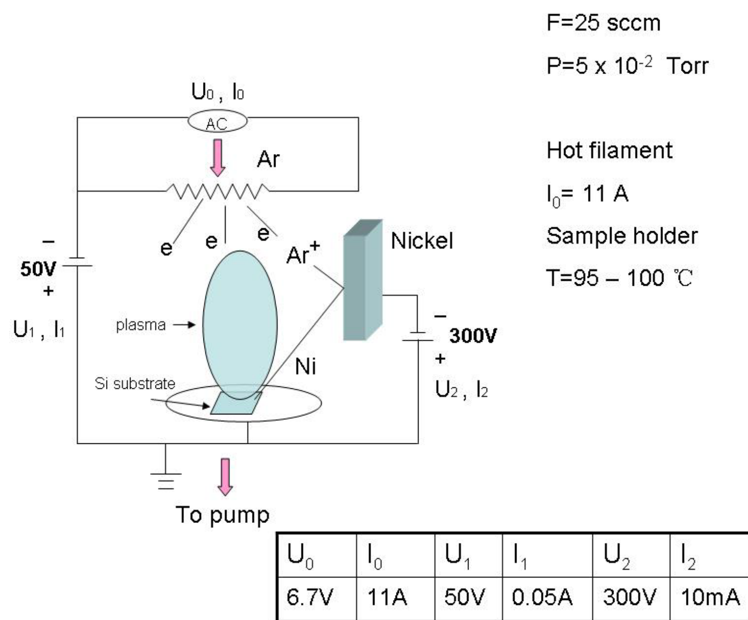

U_0	I_0	U_1	I_1	U_2	I_2
6.7V	11A	50V	0.05A	300V	10mA

Figure 3.4: Schematic diagram of the hot filament plasma sputtering coating device. The main parameters are also listed in the diagram.

After Ni coating, methane and hydrogen are introduced into the reactor for CNT growth. A dc bias voltage is applied between the filament and the substrate holder either for creating a glow discharge or for biasing the substrate without a discharge. A series of experiments under different biasing conditions have been performed. The typical experimental parameters are as follows: the total flow rate of gases is 35 sccm and the methane concentration ranged from 1.5 to 15 vol.%; the pressure in the chamber during deposition is 2.66 kPa (20 Torr); the filament current 9.5-10.5 A. The distance between the filament and the substrate is 10 mm; the substrate temperature 600 ℃, as measured by the thermocouple attached to the substrate holder. For positive bias (substrate holder as anode), the voltage between the filament and substrate holder is around 50 V to maintain a glow discharge current of 100 mA. A higher voltage of approximately 400 V is used for negative bias to maintain a glow discharge current of 100 mA, the same current as for positive bias. The typical experimental parameters and their variation ranges are listed in Table 2. When one parameter is varied, other parameters are kept at typical values listed in Table 2.

Table 2: Typical growth parameters and their variation range.

	Typical Value	Variation range
Methane concentration	8%	1.5-15%
Working pressure	2.66 kPa	266 Pa-3.99 kPa
Substrate temperature	600 ℃	400-650 ℃
Negative bias voltage and discharge current	400 V 100 mA	0-600 V 0-200 mA
Positive bias voltage and discharge current	50 V 100 mA	0-200 V 0-600 mA

3.2.3 Results and discussion

In the case when no bias voltage is applied between filament and substrate, randomly oriented nanotubes were grown, as shown in Fig. 3.5. In the case of negative bias without initiating a discharge, no matter how high the voltage (50-200 V), the resultant nanotubes were also randomly oriented, similar to those grown without bias voltage as shown in Fig. 3.5.

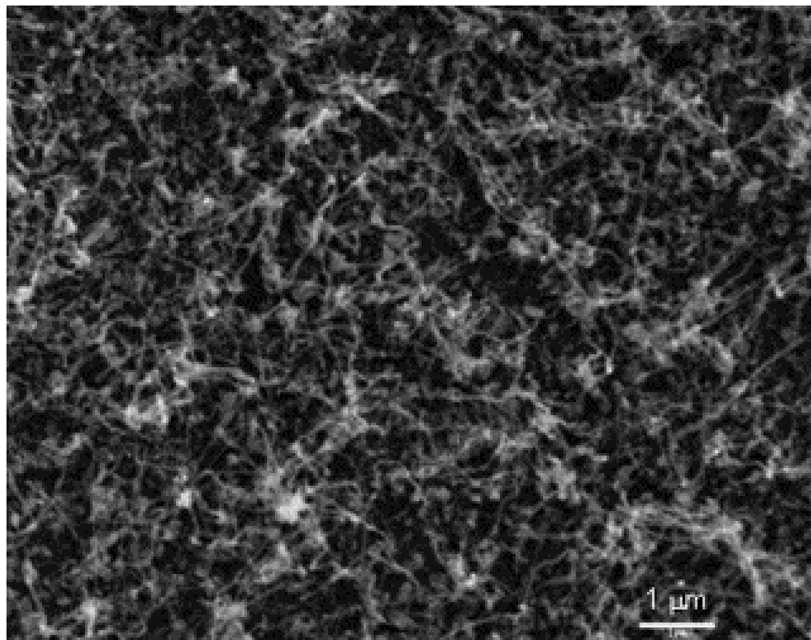

Figure 3.5: SEM micrograph of carbon nanotubes grown without bias voltage

Then a dc glow discharge is initiated by applying a bias voltage between the substrate holder and the filament. When the substrate holder is used as the anode at a discharge voltage in the range 25 to 250 V, the resulting nanotubes are also randomly oriented, similar to those grown without discharge.

When a large (over 300 V) negative bias voltage is applied to substrate holder, a plasma discharge is generated and nanotubes with different alignment angles and

orientations can be synthesized. In this case, ions bombard the substrate at high energy and deposit CNT there. In the regions around the sample edges, the orientations of the aligned CNTs gradually deviate from the normal direction at the sample center as seen in Fig. 3.6. Figure 3.6a shows SEM image of CNTs located at the left edge of the substrate where the electric field lines are expected to deviate from the substrate normal. Nanotubes in this region are aligned at large angles relative to the substrate normal. Figure 3.6b shows nanotubes grown in the region between the substrate center region and the edge where the electric field lines are not quite normal to the substrate normal. In the central region of the sample, the nanotubes are perpendicular to the sample surface as shown in Fig. 3.6c.

The alignment angle depends on both the gas pressure and the distance from the sample edge. The gradual change of the alignment angle as a function of the location from edge to center, under three different gas working pressures are illustrated in Fig. 3.7. As the distance from the edges increases, the CNT alignment gradually becomes upright (normal to the substrate surface). CNTs located far enough (>1 mm) from the edges are vertically aligned. However, with a decrease of working pressure (for a fixed discharge voltage of 400 V, the discharge current decreases with decreasing pressure), the alignment angle of CNTs to the substrate normal decreases at any fixed distance from the sample edge. The maximum alignment angle (to the substrate normal) of the CNTs located at the very edge is 38° for gas pressure of 2.66 kPa (20 Torr). This angle decreases to 25° and 14°, when the pressure is reduced to 1.06 and 0.53 kPa (8 Torr and 4 Torr), respectively. At 0.27 kPa (2 Torr) gas pressure, the resultant CNTs are almost vertically aligned even at the very edge.

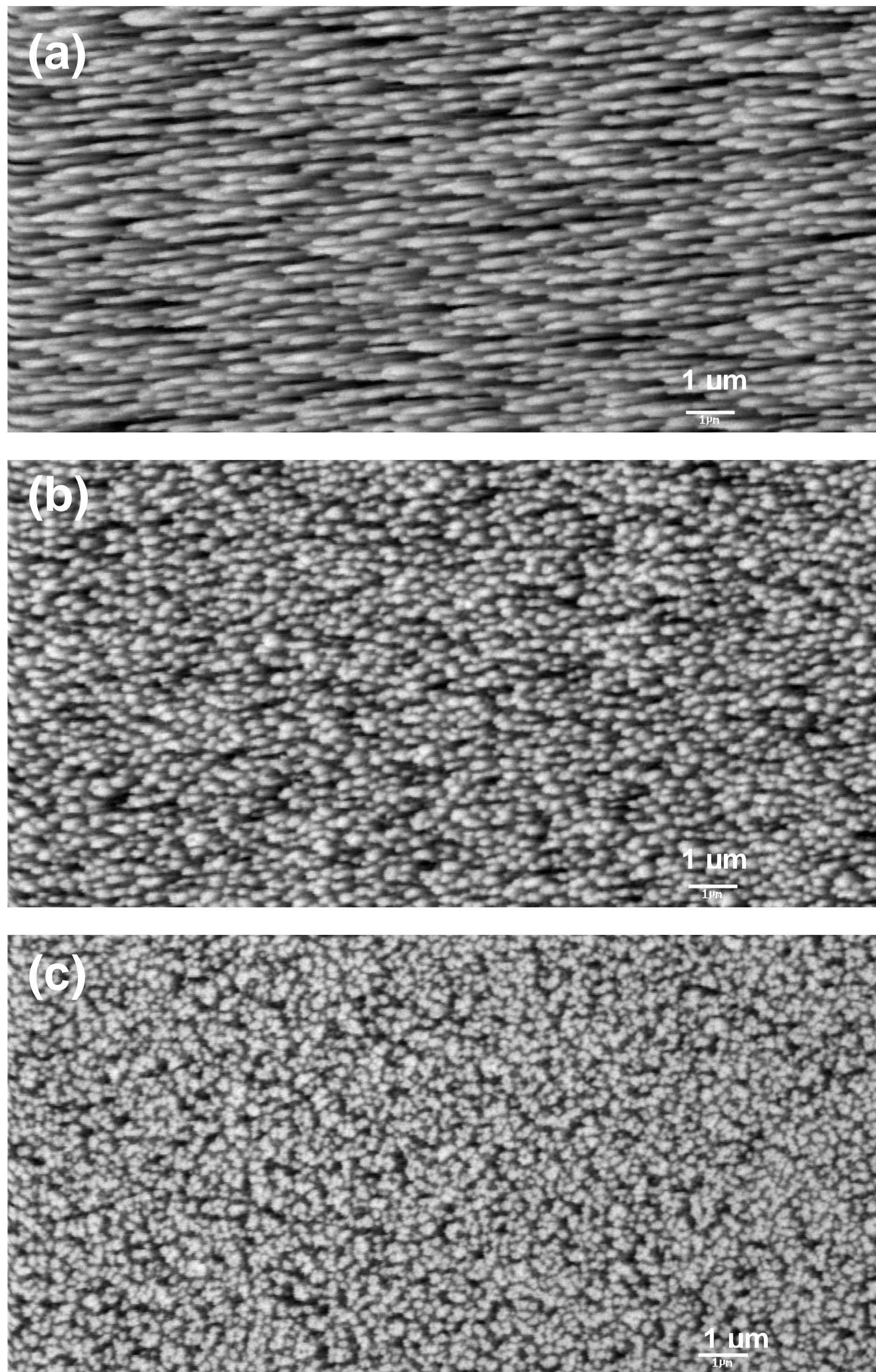

Figure 3.6: SEM (top view) images of nanotubes grown at -400 V bias at different regions: (a) at the left edge, (b) between the edge and center, (c) in the center region.

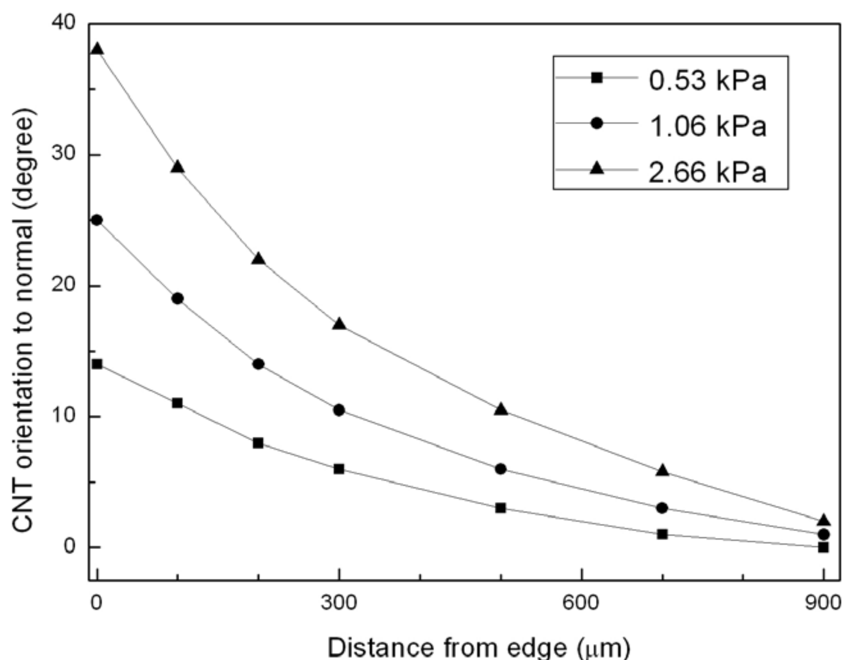

Figure 3.7: Angles between the CNTs alignment and the sample normal, as a function of the distance from the sample edge for three gas pressures in the discharge.

At 0.27 kPa (2 Torr) gas pressure and low discharge voltage less than 400 V, the orientations of the CNTs become random, similar to those shown in Fig. 3.5. The CNT alignment can be restored at 0.27 kPa (2 Torr) if the discharge voltage is increased to values between 400 and 550 V. In this case, the CNTs are almost vertically aligned even in the edge region of the samples

The nanotubes have been further analyzed by TEM. Figure 3.8 shows a TEM image of a typical carbon nanotube. The nanotube is a centrally hollow multi-walled tube, rather than a fiber. The outer diameter of this carbon tube is approximately 50 nm. The inner diameter is approximately 25 nm.

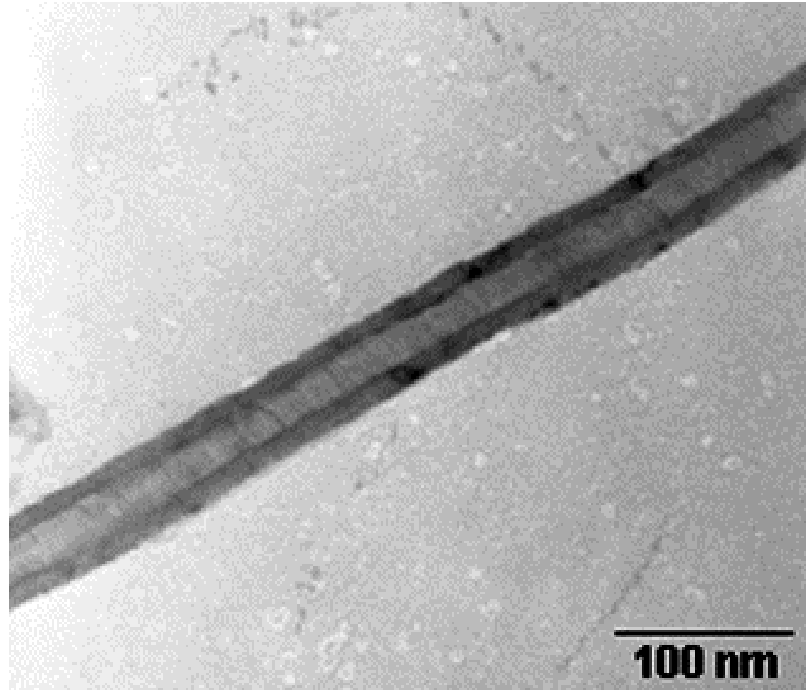

Figure 3.8: TEM image of a typical multi-walled carbon nanotube.

When no bias voltage is applied, there is neither plasma nor electric field present on the sample surface, and the resultant CNTs are randomly oriented. When a bias voltage (50–400 V) is applied, but no discharge is initiated, the electric field is present, but not the plasma. In this case, the electric field strength is expected to be uniformly distributed between two electrodes in our experimental set-up. The electric field strength on the sample surface is less than 0.05 V/μm, which is too weak to align the CNTs [*Chhowalla et al.*, 2001].

When a dc glow discharge is initiated by applying a bias voltage between the substrate holder and the filament, the potential does not vary linearly as a function of the distance from the electrodes. The potential falls mainly in the cathode region, known as the cathode sheath or cathode fall or Crookes dark space (between the cathode surface and the negative glow), and the electrical field in this region is much stronger

than any other regions between the two electrodes [*Lieberman and Lichtenberg*, 1994]. When the substrate holder is the anode, the estimated electric field strength near the substrate is less than 0.05 V/μm for a voltage less than 250 V in our experiments. This electric field is not strong enough to align the CNTs [*Chhowalla et al.*, 2001]. Consequently, the CNTs grown were randomly distributed when the substrate holder was the anode.

When the substrate holder is negatively biased, it effectively becomes a cathode, and most of the applied voltage drops near the substrate surface (cathode fall). The electric field strength on the substrate depends on the cathode fall thickness and the total voltage applied. The cathode fall thickness can be experimentally estimated by directly observing the width of the dark space around the cathode during the discharge. In our experiments, the observed fall thickness is less than 1 mm when the working pressure is 2.66 kPa (20 Torr). Even if the applied voltage is as low as 250 V, the estimated electric field strength around the sample surface is larger than 0.25 V/μm, which is sufficient to completely align the nanotubes [*Chhowalla et al.*, 2001]. When the working pressure is decreased to 0.27 kPa (2 Torr) and the applied voltage is kept at 400 V, the observed fall thickness is approximately 7 mm, and the estimated electric field strength is less than 0.1V/μm, which is too weak to align the nanotubes [*Chhowalla et al.*, 2001]. When the voltage is increased to 550 V at 0.27 kPa (2 Torr), the observed cathode fall thickness is approximately 5 mm and the estimated electric field strength increases to the order of approximately 0.1 V/μm. Consequently, well-aligned nanotubes can be obtained.

The cathode fall thickness can also be estimated theoretically. In a normal glow discharge, the width of the cathode region is proportional to p^{-1} (p is the working pressure) for a given type of the working gas and cathode material [*Lieberman and*

Lichtenberg, 1994]. For a pure hydrogen gas and a pure iron cathode in a conventional glow discharge configuration (a long glass cylinder with the anode at one end and a cathode at the other), the normal fall thickness is 9 mm at 0.13 kPa (1 Torr). Thus, the estimated cathode fall thickness at 0.27 kPa and 2.66 kPa (2 Torr and 20 Torr) is 4.5 and 0.05 mm, respectively, consistent with the observed thickness in our experiments.

In the presence of a discharge with the substrate holder as the cathode, the electric field lines around the sample surface are expected to change orientation as shown in Fig. 3.8. The electric field lines around the central region of the samples are oriented perpendicular to the sample surface. However, the direction of the field lines deviates from the substrate normal near the substrate edges due to the edge effect. The angle between the expected field lines and the substrate normal depends on the cathode fall thickness and the distance from the edge. The smaller the cathode region and closer towards the edge, the greater the angle deviates from the substrate normal. It is reasonable to expect that the angle deviates more significantly when the cathode region is narrow (Fig. 3.8a, corresponding to high pressures) compared to the larger cathode region case (Fig. 3.8b, corresponding to low pressures). Therefore, a lower gas pressure leads to wider cathode region, less edge effect, and thus smaller deviation of the electric field lines from the substrate normal. The observed reduction of the deviation angle of the CNTs with decreasing pressure shown in Fig. 3.8 apparently relates to this variation of electric field lines due to the pressure change. Our experiments suggest that the CNT alignment orientations coincide with the expected electric field line directions near the substrate and can be controlled by adjusting the gas pressure.

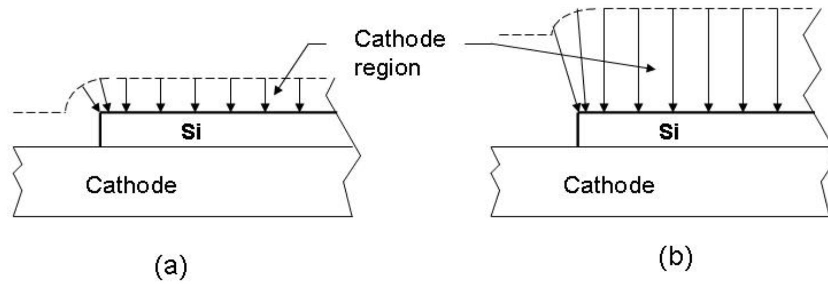

Figure 3.9: A cut-way view of the sample and the expected electric field lines in the cathode region around the sample for (a) narrow and (b) wide cathode region.

The fact that aligned CNTs can be obtained in a discharge only with the substrate as the cathode, supports the model that the unidirectional velocity distribution of carbon-containing ions incident on the substrate is responsible for the alignment of CNTs, proposed by Gamaly and Ebbesen [*Gamaly* and *Ebbesen*, 1995]. Due to the sharp potential drop near the cathode, ions reach high velocities along the direction of the electric field lines toward substrate. The directed carbon-containing ions facilitate the building of tubes in the direction of their motion (along the direction of electric field-lines). When the substrate holder is the anode, the high-energy ions towards the substrate are absent, and CNTs alignment has not been obtained in our experiments.

3.2.4 Conclusion

Growth of carbon nanotubes using HFCVD in a CH_4/H_2 gas mixture under various conditions has been investigated. Well-aligned nanotubes with variable orientations can be synthesized by initiating a dc glow discharge between the hot filament and the substrate holder, with the substrate holder as the negative electrode. A gradual deviation of the nanotube orientation with respect to the substrate normal has been observed near the sample edges, no matter where the sample is placed on the substrate holder. The

results suggest that the electric field is a determining factor for the alignment and the alignment orientation is likely determined by the direction of electric field lines on the sample surface. The orientation of CNTs can be controlled by adjusting the working pressure, presumably due to the change of electric field line directions in the cathode region at different pressures.

Chapter 4

Effects of the carbon source: graphite etching

The conventional conditions for diamond growth in Plasma Enhanced CVD (PECVD) include the use of substrate temperatures higher than 700 ℃ and a carbon-containing precursor gas diluted in excess hydrogen (typically $<5\%$ CH_4 in H_2) [*Angus* and *Hayman*, 1988; *Ashfold et al.*, 1994]. In this chapter, diamond synthesis at unusually low temperature (250 ℃) achieved by a unique carbon feeding (graphite etching) will be presented. This methodology allows deposition of diamond on materials with low melting points.

4.1 Low temperature synthesis of diamond thin films with in situ graphite etching

4.1.1 Introduction

CVD in hydrogen gas mixed with hydrocarbon gas is commonly used to synthesize diamond films. However, in this method, a substrate temperature above 700 ℃ is required for synthesis of high quality diamond films with reasonably high growth rate (over 1 μm/h). Substrates which melt or undergo phase transition at these temperatures cannot therefore be coated with diamond films. Removing this limitation would expand the applications of diamond films to such areas as micro-electronics and optics, and thus

the development of a low temperature synthesis technology for high purity diamond films is of current interest for practical applications. Several methods have been tested to lower the synthesis temperature: adding oxygen [*Asmann et al.*, 1999], using a halogenated carbon-containing precursor [*Proffitt et al.*, 2000; *Schmidt* and *Benndorf*, 2001], using gas mixtures of CO_2/CH_4 [*Petherbridge et al.*, 2001] and CO/H_2 [*Lee et al.*, 1996], improving the seeding processes [*Hiraki*, 2001], and using both argon-rich plasma and improved seeding processes [*Xiao et al.*, 2004]. However, to date, no direct evidence of the successful synthesis of a high-purity crystalline diamond film at temperatures below 300 ℃ has been reported.

In this section, a novel methodology in microwave CVD based on graphite etching for diamond thin film deposition at temperatures as low as 250 ℃ is described. In this method, no additional carbon sources are required. The diamond synthesis at low temperatures is believed to be induced by activated transitional hydrocarbon radicals formed in situ through hydrogen etching of graphite.

4.1.2 Experiments

The MWCVD reactor is filled with hydrogen in which a thin isotropic polycrystalline graphite sheet (Poco EDM-3) is placed underneath the silicon substrates. The graphite sheet acts as a carbon source. The vacuum chamber is pumped down to a pressure of 6.65×10^{-4} Pa using a turbo-molecular pump. Pure hydrogen gas is introduced using a mass flow controller. P-type (100)-oriented mirror polished Si wafers of thickness of 0.65 mm are chosen as substrates. In order to get a high nucleation density of diamond, the silicon substrate is ultrasonically scratched in a solution containing diamond powder. The substrate temperature is measured with a thermocouple mounted right behind the

substrate holder. When the working pressure is stabilized at 4 kPa (30 Torr), a 2.45 GHz microwave source is switched on to form a hydrogen plasma. In this process, almost no carbon soot is formed in the deposition system (chamber walls or substrate stage) because the hydrocarbon is only formed locally by hydrogen etching of graphite. This arrangement significantly reduces carbon contamination of the deposition system.

In order to compare the samples grown using a conventional gas mixture of methane and hydrogen, diamond thin films were also deposited using a gas mixture of 1% CH_4 + 99% H_2 under similar conditions without graphite inside the reaction chamber.

4.1.3 Results and discussion

Figure 4.1 shows the SEM morphologies (plan-view) of diamond films grown at substrate temperatures 310 ℃ and 250 ℃. Sharp triangle-faceted crystallites of submicron scale are clearly seen in films grown at a substrate temperature of 310 ℃ (Fig. 4.2a). Triangle-faceted grains in the films indicate (111) planes are the preferred growth plane. As seen in Fig. 4.2b, the grain size of the film is of nanoscale size when the substrate temperature is at 250 ℃. The facets of the crystallites in this case can not be seen clearly from SEM. The thickness of the films, measured by imaging the cross section of the thin film using SEM, shows that the growth rates of the diamond films are approximately 150 nm/h and 60 nm/h at 310 ℃ and 250 ℃, respectively.

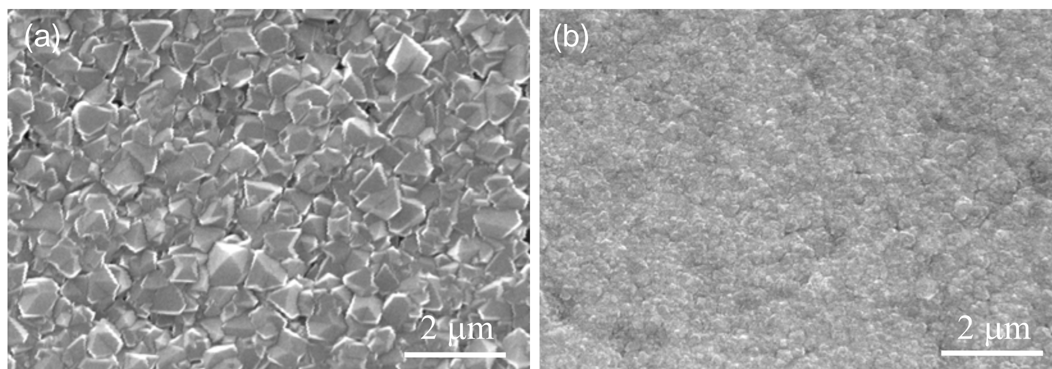

Figure 4.1: Typical SEM morphologies (plan-view) of diamond films grown on silicon at substrate temperatures (a) 310 ℃ for 10 h and (b) 250 ℃ for 20 h.

For comparison, diamond films grown under similar conditions with the conventional method using H_2 + 1% CH_4 gas mixture are shown in Fig. 4.2. No faceted diamond crystallites can be seen in the films grown at 310 ℃ (Fig. 4.2a). Only separated, spherical particles were grown on the samples at a temperature of 250 ℃ (Fig. 4.2b), indicating much lower nucleation density and much lower growth rate compared with the case of graphite etching.

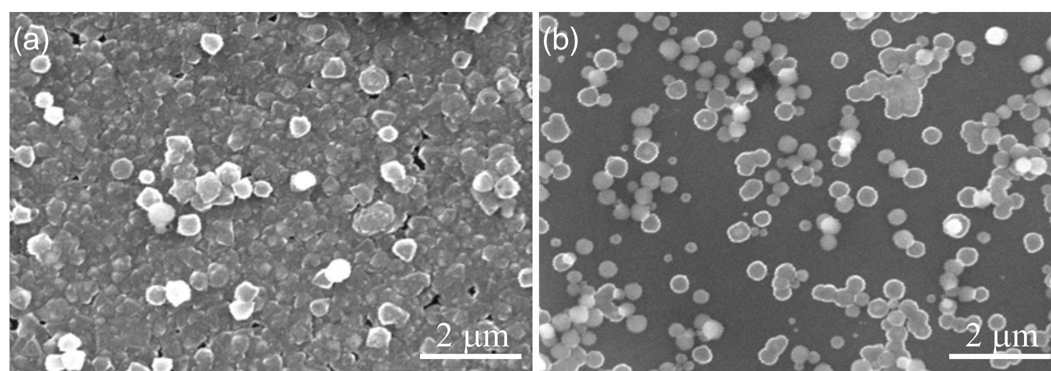

Figure 4.2: Typical SEM morphologies (plan-view) of diamond films grown on silicon at substrate temperatures (a) 310 ℃ for 10 h and (b) 250 ℃ for 30 h using conventional H_2 + 1% CH_4 gas mixture.

Curves a and b in Fig. 4.3 show visible Raman spectra (laser wavelength at 514 nm) of the films shown in Fig. 4.1. A clearly defined Raman phonon peak around 1333

cm^{-1}, characteristic of diamond phase, is observed in the spectrum of samples grown at substrate temperatures 310 ℃. The characteristic diamond peak becomes broadened as the substrate temperature is lowered to 250 ℃. This is accompanied by a slight increase of the broader band at around 1580 cm^{-1}. The broadening of the diamond peak at 1333 cm^{-1} is mainly due to the decrease of the diamond grain size from micrometer scale to nanometer scale [*Ager et al.*, 1991; *Prawer et al.*, 2000]. The broad peak at 1580 cm^{-1} corresponds to sp^2-bonded carbon. This peak is very weak even at the substrate temperature of 250 ℃. Considering the fact that Raman scattering in the visible range (514 nm) is about 50 times more sensitive to sp^2-bonded carbon than to sp^3-bonded carbon and the grain boundaries consist of sp^2-bonded carbon, the diamond films synthesized at low temperature (lower than 300 ℃) are likely of high purity.

Raman spectra of samples grown with the conventional H_2 + 1% CH_4 gas mixture are shown in curves c and d in Fig. 4.3. They exhibit a lower peak around 1333 cm^{-1}, and a much higher peak around 1580 cm^{-1} than those in curves a and b, indicating higher sp^2-bonded carbon in the samples. The absence of the characteristic diamond peak in the spectrum of samples grown at 250 ℃ using the conventional H_2 + 1% CH_4 gas mixture is clearly seen in curve d.

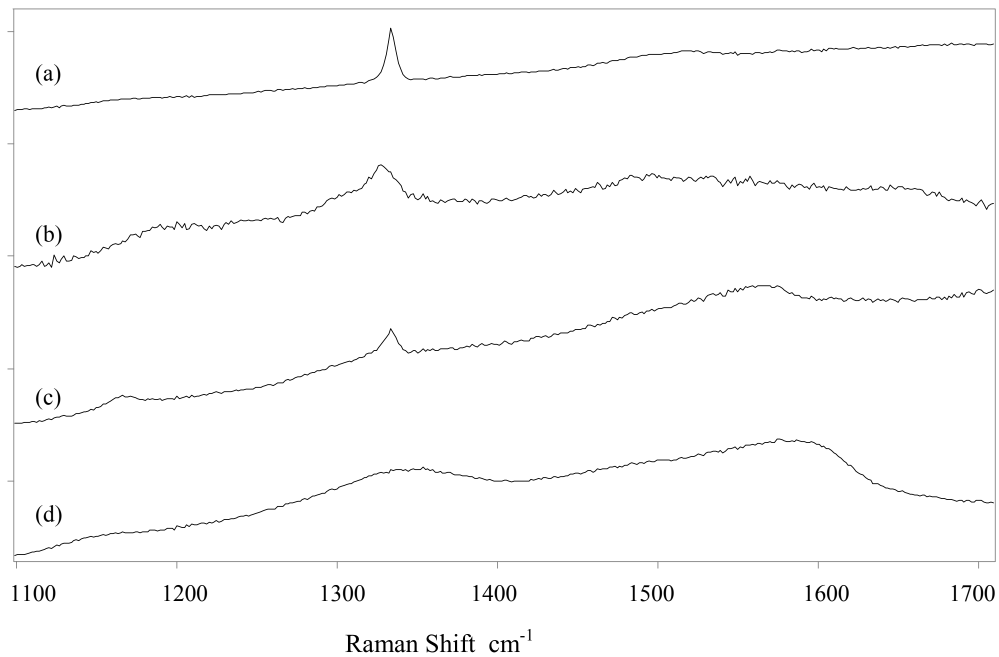

Figure 4.3: Typical Raman spectra of the diamond films grown at substrate temperature (a) 310 ℃ for 10 h and (b) 250 ℃ through graphite etching; (c) 310 ℃ and (d) 250 ℃ using conventional H_2 + 1% CH_4 gas mixture.

The experimental results show that diamond thin films can be synthesized at temperatures as low as 250 ℃ by etching graphite in a microwave hydrogen plasma. The new diamond synthesis technique uses in situ graphite etching as a carbon source instead of conventional hydrocarbon gases and has several advantages over the conventional process including deposition at unusually low temperature, higher growth rate, lower sp^2-bonded carbon concentration, and reduced carbon contamination of the microwave plasma reactor. Thermodynamically speaking, direct conversion of graphite into diamond is impossible under our experimental conditions, because the conversion is characterized by a positive Gibbs free energy change. However, it is well known that graphite can be selectively etched by atomic hydrogen generated by microwave plasma under the deposition conditions. In contrast to molecular hydrogen, atomic hydrogen is

extremely reactive. Atomic hydrogen etches graphite twenty times as fast as it etches diamond. The graphite sheet and non-diamond carbon grown on the substrate were preferentially etched by atomic hydrogen. The graphite etched in situ forms activated transitional hydrocarbon radicals around the substrate. These activated transitional hydrocarbon radicals formed in situ act as diamond precursors, lowering the activation energy and providing unique chemistry for diamond nucleation and growth. Lowering the activation energy can facilitate and enhance the nucleation and growth of diamond at low temperatures. An activation energy of 23 kcal/mol was reported for conventional H_2/CH_4 system [*Kondoh et al.*, 1993]. However, in work on low temperature diamond growth, 7 kcal/mol was reported for the CO_2/CH_4 mixture [*Petherbridge et al.*, 2001], 8 kcal/mol for the CO/H_2 mixture [*Lee et al.*, 1996], and 5.85 kcal/mol for the case of an Ar/CH_4 mixture and improved seeding processes [*McCauley et al.*, 1998]. When the carbon source is supplied by hydrocarbon gas, only a small portion of the hydrocarbon gas is decomposed and activated by the plasma to form activated hydrocarbon radicals. The concentration of the activated hydrocarbon radicals is likely much lower than formed in the in situ graphite etching process. The concentration of the activated hydrocarbon radicals around the substrate is even lower after traveling from the plasma to the substrate, because the transporting distance is longer than that in the in situ graphite etching process. A higher concentration of activated hydrocarbon radicals usually results in higher diamond growth rate and higher secondary nucleation rate of diamond. The higher concentration of activated transitional hydrocarbon radicals around the substrate is believed to contribute to the higher diamond quality and higher growth rate of diamond films in this graphite etching process.

4.1.4 Conclusion

In this section, it is shown that in microwave CVD, diamond thin films can be deposited at unusually low temperatures with in situ graphite etching which provides the carbon feed. Results indicate that diamond can be synthesized at temperatures as low as 250 ℃ by etching graphite without other carbon sources. This new synthesis technique has several advantages over the conventional process including deposition at unusually low temperature, higher growth rate, lower sp^2 bonded carbon concentration, and reduced carbon contamination of the reactor. The mechanism of diamond nucleation and growth by graphite etching at low substrate temperature was addressed in this study. The methodology may open a path to coating pure diamond films on steels and on low softening- or melting-points materials including glass and aluminum.

4.2 Deposition of diamond thin films on steels using graphite etching

4.2.1 Introduction

Chemical inertness along with high hardness and a low friction coefficient make diamond films an ideal protective coating against corrosion and wear in cutting tools used in metal working industries. However, deposition of diamond films on steels is problematic due to several reasons as explained below. The experiments presented in this section aim to explore the feasibility of depositing continuous diamond films on steels. In one attempt, an aluminum buffer layer was first deposited on the steel to prevent the graphitization problem and the diamond film was deposited on the

pretreated substrates by graphite etching. In the following, a review of studies of the deposition of diamond on steels is given.

Well-adhering CVD diamond films have been successfully deposited on some non-ferrous metals (e.g., WC-Co alloy for dental burs [*Sein et al.*, 2003]). Initial tests indicate that such CVD diamond-coated tools have a longer life and better tool performance. However, a large number of reports showed that it was difficult to deposit well adhering, continuous and high quality diamond layers on steel substrates. A number of severe problems occur during the initial nucleation and the subsequent growth stage of the CVD processes when blank steels are used as substrates [*Weiser et al.*, 1992]. The main problems are: *i*) the high diffusion of atomic carbon into the steel; *ii*) the catalytic effect of iron on the formation of graphite during the CVD process; *iii*) the significant difference in the thermal expansion coefficients between the steel substrate and the diamond film; *iv*) the phase transition problem of steel at high temperatures. Several research groups have been focusing on using suitable intermediate layers as a barrier in order to mitigate these problems [*Glozman et al.*, 1998; *Nesladek et al.*, 1994]. Such intermediate layers have to fulfill the following requirements: *i*) barrier against the diffusion of carbon from the gas phase into the substrate and against the diffusion of iron from the substrate onto the surface and *ii*) excellent adhesion of diamond coating on steel.

Extensive studies have been carried out to investigate different intermediate layers to achieve continuous, good-adhering diamond on ferrous substrates. It has been found that many intermediate coatings investigated are not able to meet all the requirements as described above. To date, only a small number of groups have obtained some encouraging, but not completely satisfactory, results. For example, Glozman *et al.* [*Glozman et al.*, 1998] and Schwarz *et al.* [*Schwarz et al.*, 2002] described the growth

of well-adhering diamond coatings by means of nitrided chromium and diffusion chromized intermediate layers, respectively.

One of the key problems related to the difficulties mentioned above is the high substrate temperatures involved in conventional CVD diamond deposition. A high temperature induces stress and phase transition. The stress and phase transition problems may be solved by combining the appropriate intermediate layers and low substrate temperatures during the diamond growth process through graphite etching. In this section, the synthesis of continuous diamond films on aluminum-coated steels using graphite etching will be described.

4.2.2 Experiments

Diamond deposition was performed using the graphite etching method as described in Section 4.1. Mild steel (1018 mild steel) and stainless steel (304 stainless steel) substrates were used in the experiments. The 1018 steel is composed of 0.15% - 0.20% C, 0.60% - 0.90% Mn, <0.04% P, <0.05% S, and the remainder is Fe, whereas 304 stainless steel contains <0.08% C, 17.5 - 20% Cr, 8 - 11% Ni, <2% Mn, <1% Si, <0.045% P, <0.03% S with the balance Fe. Direct deposition of diamond onto the mild steel and stainless steel substrates was attempted in a hot filament reactor at a substrate temperature of 400 ℃. Diamond deposition was also performed on aluminum-coated steel substrates under similar conditions. The aluminum interlayer coating was obtained using the plasma sputtering technique described in Section 3.2.2.

4.2.3 Results and discussion

Figure 4.4 shows the SEM image of the deposited film on the mild steel substrate using graphite etching. The film is porous and consists of loosely distributed grains which are sub-micrometer in size. Figure 4.5 shows the Raman spectrum of the film. The characteristic graphite peaks at 1350 cm^{-1} and 1580 cm^{-1} were observed. The deposited film on stainless steel has a similar morphology and Raman spectrum (data not shown here).

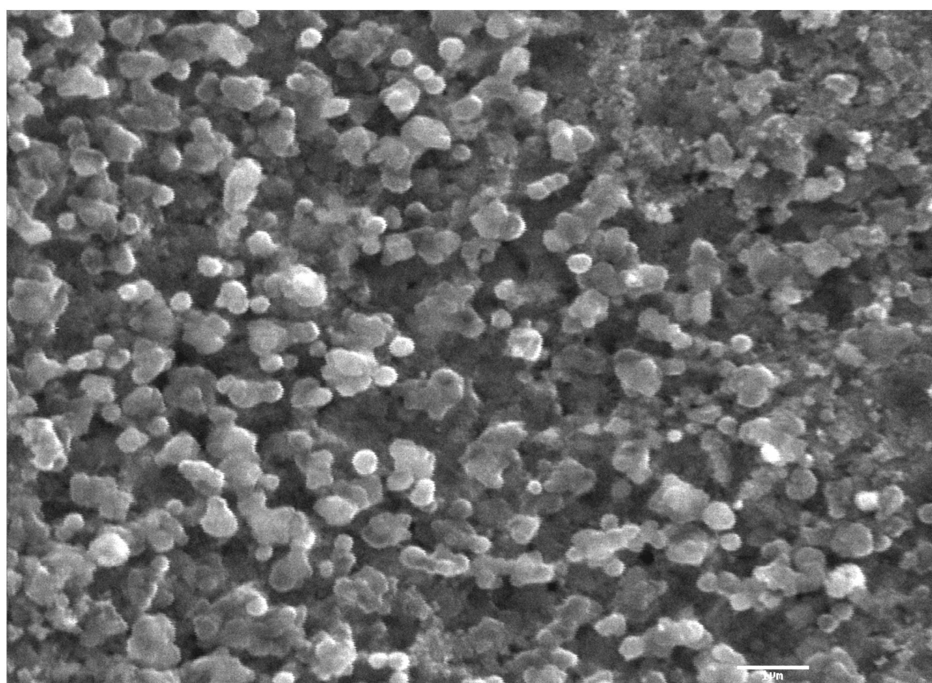

Figure 4.4: SEM image of the carbon layer formed on a mild steel substrate using graphite etching.

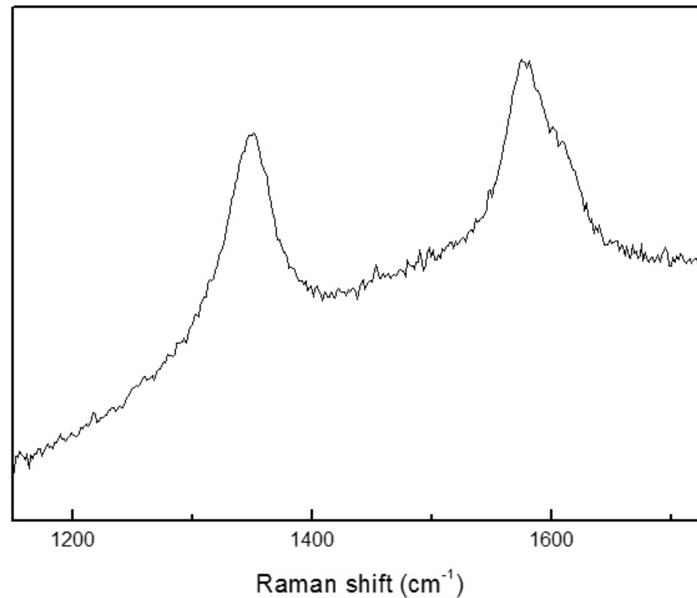

Figure 4.5: Typical Raman spectrum of the carbon layer deposited on a mild steel substrate using graphite etching.

It has been well established that direct deposition of carbon onto cutting tool steel samples leads to the formation of graphitic soot in the conventional diamond CVD methods [*Weiser et al.*, 1992; *Weiser* and *Prawer*, 1995]. This is explained by the catalytic effect of iron in the preferential nucleation of graphite. Similar results have been observed in our study. The interlayer system on steel substrates is necessary in order to avoid the graphite catalytic effect of iron. An aluminum interlayer was adopted in this study.

Figure 4.6 shows the SEM image of the as-deposited film on an aluminum-coated steel substrate by graphite etching at a substrate temperature of 400 ℃. Thick and continuous faceted grains with sub-micrometer grain size were deposited. Fig. 4.7 shows the Raman spectrum of the sample. A characteristic diamond peak at 1335 cm^{-1} is clearly seen. The shift of the peak position from 1333 cm^{-1} may be due to the stress between the diamond film and substrate. The experimental results show that the aluminum interlayer does work as a barrier layer to inhibit the catalytic effect of iron on

carbon-based radicals to form graphitic soot. Deposition of continuous diamond film on the aluminum coated steel materials is achieved.

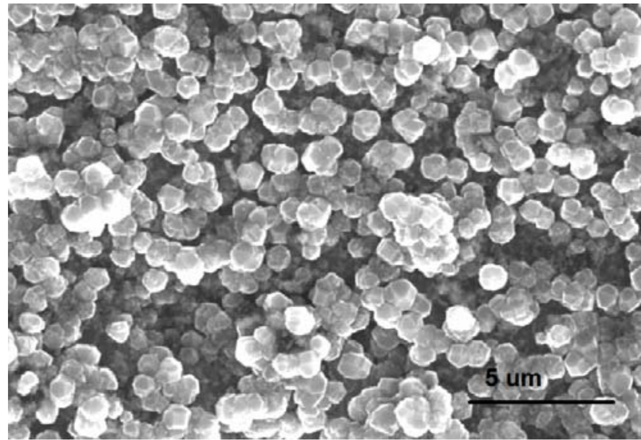

Figure 4.6: SEM image of diamond film deposited on the aluminum-coated steel substrate using graphite etching.

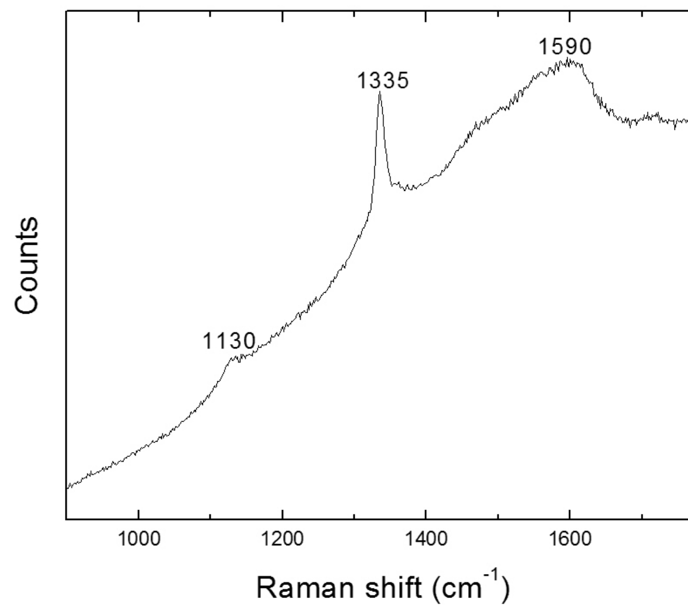

Figure 4.7: Raman spectrum of the diamond film deposited on the aluminum-coated steel substrate using graphite etching.

4.2.4 Conclusion

The study described in this section investigates the feasibility of depositing diamond films on steel materials. After depositing an aluminum interlayer on either carbon steels or stainless steel substrates, continuous diamond films have been successfully deposited on the interlayer at low temperatures by the in situ graphite etching technique, suggesting that the Al-interlayer prevented graphitization and increased diamond the nucleation density.

Chapter 5

Effects of gas flow rate on diamond nucleation and growth

Gas flow rate is an important parameter for CVD diamond growth because it is closely related to the transport of radicals in the CVD reactor [*Rau* and *Picht*, 1992]. An experiment has been designed and carried out to investigate the effects of the gas flow rate on the deposition of diamond films on silicon substrates using a microwave plasma CVD reactor. The experimental results show that the gas flow rate affects diamond nucleation density and also the diamond grain size. Nanodiamond films can be obtained at high gas flow rate, while at low flow rate microcrystalline diamond films are deposited. It is also demonstrated that diamond grain size can be further reduced with a positive substrate biasing under high gas flow rate. The smooth nanocrystalline diamond (NCD) film grown under this condition is beneficial for tribological and optical applications.

5.1 Introduction

To date, some efforts have been made to investigate the effects of the gas flow rate on diamond growth but conflicting results have been reported by different groups. Celii *et al.* [*Celii et al.* 1991; *Celii et al.*, 1992] reported that varying the gas flow rate could change markedly the resultant microcrystalline diamond (MCD) crystal texture and

surface morphology but has little effect on the growth rate. Yu *et al.* [*Yu et al.*, 1998; *Yu et al.*, 1999] have found that CVD diamond growth by hot filament CVD depends on a mass transfer controlled process where the initial diamond nucleation was enhanced and the growth rate improved as the gas flow rate was increased, while other groups reported that the gas flow rate did not appear to have a significant influence on diamond nucleation and growth [*Fan et al.*, 1999; *Buchkremer-Hermanns et al.*, 1996]. The experimental results to be reported here show that the variation of the gas flow rate has much more dramatic effects on diamond film morphology than those previously published [*Celii et al.* 1991] and [*Celii et al.* 1992] in which synthesis of only MCD films with different morphology were reported. Well-faceted MCD films have been deposited at lower flow rates (bellow 300 sccm). Randomly oriented submicron diamond films have been deposited at the flow rate of 300 sccm. At higher gas flow rates (above 300 sccm), NCD films have been obtained.

5.2 Experiments

Diamond deposition experiments were conducted using the MWCVD reactor. Under the optimized conditions, an excited spherical plasma ball is located around 5 mm above the substrate holder. The substrate holder is usually located 50 mm below the top gas diffuser and 30 mm above the bottom gas diffuser.

The *p*-type (100) mirror-polished silicon wafers, each with a size of $10 \times 10 \times 0.5$ mm^3, are used as substrates. Thin films are grown through two consecutive stages. In order to achieve a high initial nucleation density, substrates are pretreated in the first stage by bias enhanced nucleation in which a negative bias voltage of -350 V is applied to the substrate holder for 30 min. A mixture of 5 vol% CH_4 and 95 vol% H_2 at

a total flow rate of 100 sccm is supplied for the discharge during the bias enhanced nucleation stage. In the second stage, the bias voltage is removed and the methane concentration is reduced to 2 vol%. The processing time of the second stage was 22 hours. The total gas flow rate is set at 30, 50, 70, 100, 120, 200, 300, 400, 500 sccm, while the total pressure is maintained at 4 kPa through feedback control of a throttle valve in the pumping line. During both stages, the total pressure, substrate temperature, and microwave power are maintained at 4 kPa (30 Torr), 560 ℃, and 1000 W, respectively.

The films are characterized by a variety of techniques. SEM and AFM are used to image the surface morphology of the deposited diamond films. The AFM measurements were carried out on a PicoSPM instrument (Molecular Imaging, Tempe, AZ) operated in both contact and intermittent contact modes. The curvature radii of the silicon cantilevers were approximately 10 nm and 1 nm for contact mode and intermittent contact mode, respectively. Micro-Raman measurements and X-ray diffraction (XRD) measurements were also performed. In addition, the field electron emission (FEE) properties of the diamond films were investigated by a home-made device [*Lu et al.*, 2005].

5.3 Results and discussion

Figure 5.1 shows representative SEM micrographs (plan-view) of samples grown at different gas flow rates. With increasing gas flow rate, the film surface morphology gradually changes from typical MCD films to NCD films. At relatively low gas flow rates (30 sccm to 200 sccm), highly oriented and well-faceted MCD films (with an average grain size of 1 micron) are deposited (Fig. 5.1a). When the gas flow rate

increases to 300 sccm, the grain size of the deposited thin films reduces to the submicron scale and the grain orientation becomes random (Fig. 5.1b). Further increase in the gas flow rate (in the range from 300 sccm to 500 sccm, Fig. 5.1c) results in formation of films with a cauliflower-like morphology. The films consist of clusters of ball-like particles with a diameter of approximately 10 microns. Each cluster consists of a large number of much smaller grains with nanometer scales. The facets and the exact grain size of the crystallites can not be clearly identified from the SEM image due to its limited resolution. The cross-section SEM images of the diamond films (data not shown) are used to estimate the film thickness. The thickness of the diamond films grown at various gas flow rates is around 8 μm for diamond films grown at a gas flow rate below 300 sccm and 9 μm at a flow rate above 300 sccm. The gas flow rate has little effect on the diamond growth rate.

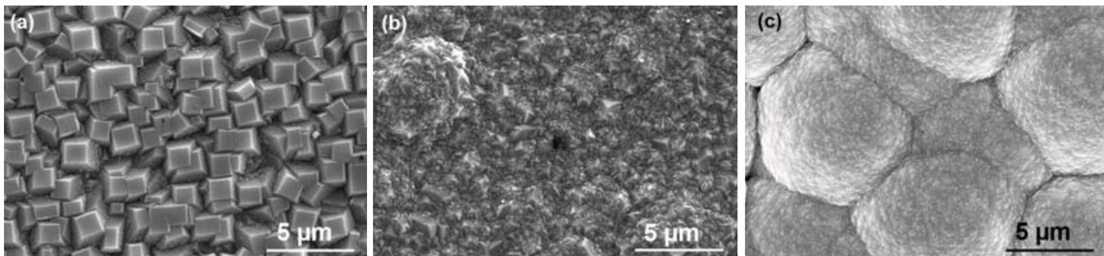

Figure 5.1: Typical SEM morphologies (plan-view) of films grown at various gas flow rates (sccm) of: (a) 200, (b) 300, and (c) 400.

Figure 5.2 shows typical AFM images of an NCD film. The higher resolution AFM image in Fig. 5.2a shows the details of the individual grains and the lower resolution AFM image in Fig. 5.2b has been used to estimate the overall surface roughness of the NCD film. Detailed image analyses performed by a computer software indicate that the average size of the tiny grains on the cauliflower-like clusters

is about 30 nm (Fig. 5.2a) and the root mean square surface roughness (R_m) of the film is found to be 244 nm over a 20μm ×20μm AFM image area (Fig. 5.2b).

Figure 5.3 shows the Raman spectra of the films grown at three different gas flow rates. As the flow rate increases, the spectrum gradually changes from the typical spectrum of MCD to those of NCD films. A sharp peak around 1333 cm^{-1}, characteristic of the sp^3-bonded diamond phase, is clearly shown in the spectrum of the sample grown at a gas flow rate of 200 sccm (curve (a)). The full width at half maximum (FWHM) of this peak of the sample is 6.2 cm^{-1}. The peak becomes broadened as the gas flow rate increases. The FWHM of the peak increases to 10.8 cm^{-1} for the sample grown at 300 sccm (curve (b)). At a gas flow rate of 400 sccm, the FWHM of the diamond peak increases further to 18.5 cm^{-1} and two additional peaks emerge at around 1140 cm^{-1} and 1480 cm^{-1} respectively (curve (c)). The origin of these two peaks has been attributed to either the size effect of NCD [*Yarbrough* and *Messier*, 1990] or the trans-polyacetylene in NCD films [*Pfeiffer et al.*, 2003]. The broadening of the diamond peak at 1333 cm^{-1} in Fig. 5.3 is mainly attributed to the small grain size in the films [*Robin et al.*, 1990]. It has also been noted that the broad band peak centered at around 1580 cm^{-1}, corresponding to sp^2-bonded amorphous carbon, increases slightly in curves (b) and (c) for the samples deposited at 300 and 400 sccm. Considering the fact that the sp^2-bonded carbon has 50 times higher Raman scattering efficiency than the sp^3-bonded carbon and the grain boundaries usually consist of sp^2-bonded carbon [*Wada et al.*, 1981], the diamond films synthesized have fairly high diamond content.

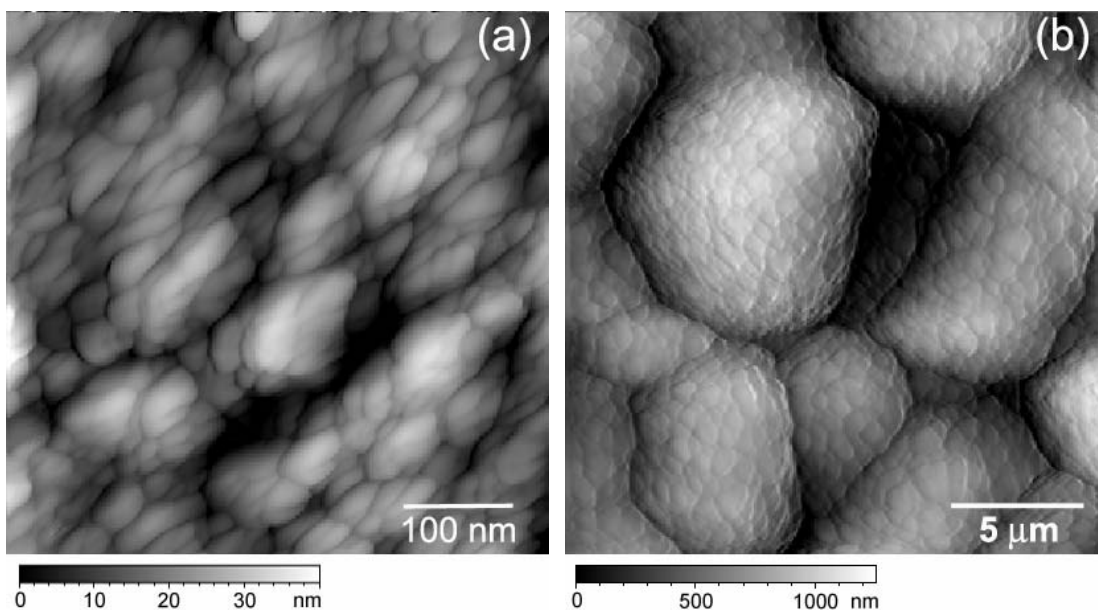

Figure 5.2: The 0.5×0.5 μm^2 and (b) the 20×20 μm^2 AFM topography of the NCD film grown at gas flow rate of 400 sccm.

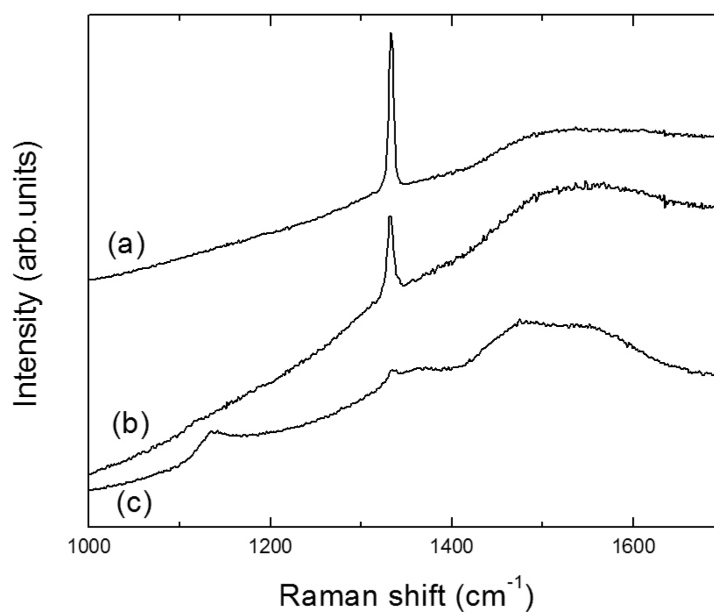

Figure 5.3: Typical Raman spectra of the diamond films grown at gas flow rates (sccm) of: (a) 200, (b) 300, and (c) 400.

The existence of the diamond structure of the NCD films corresponding to curve (c) in Fig. 5.3 is also confirmed by the X-ray powder diffraction pattern shown in Fig.

5.4. The position and relative intensity of the diffraction peaks (44.15°, 75.55°, 91.5°, 119.6°) are in good agreement with those of the randomly oriented cubic diamond powders (JCPDS 6-675), suggesting that the diamond grains in the films are randomly oriented as also shown in Fig. 5.1c.

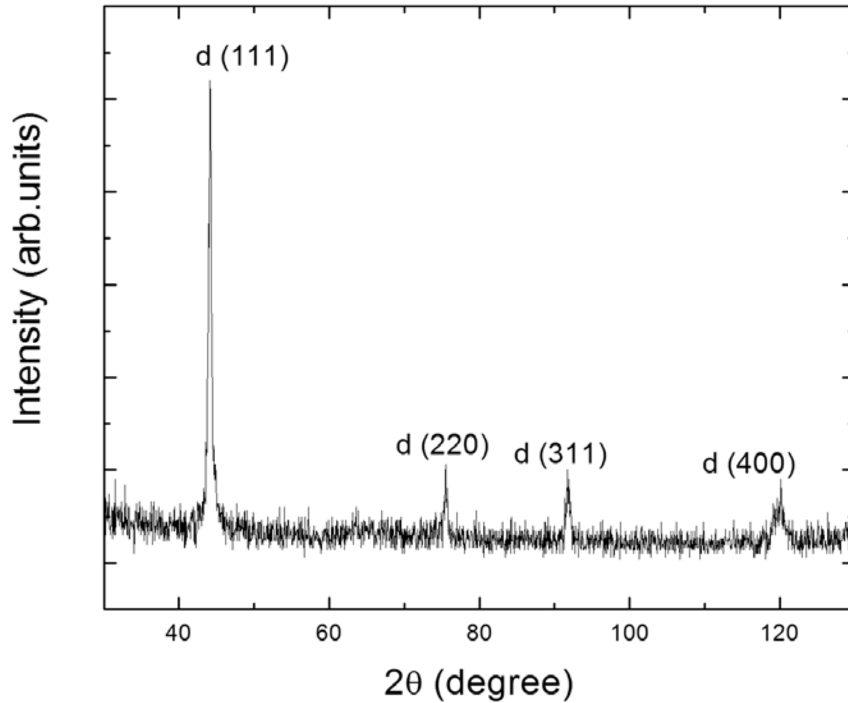

Figure 5.4: XRD pattern of the NCD film grown at a flow rate of 400 sccm.

Different properties of the MCD and NCD films are also revealed in the FEE measurements. The measured characteristic curves of the emission current from the diamond films synthesized at different flow rates (same sample as shown in Fig. 5.1) as the function of the applied electric field are shown in Fig. 5.5. Compared with the well-faceted MCD films and randomly oriented submicron diamond films, the FEE properties of the NCD films synthesized at high gas flow rates are significantly improved. The turn-on electric field (defined as an electric field at which the measured

current reaches 0.01 μA) decreases from 11 V/μm for well-faceted MCD films to 6 V/μm for NCD films. The emission current increases from 0.5 μA to 21.7 μA at the same electric field of 18 V/μm when the total flow rate increases from 200 sccm to 400 sccm. The turn-on field and emission current measured at 18 V/μm are listed in Table 3. The improved FEE properties of the NCD films may be attributed to the decrease in the diamond grain size [*Gruen*, 1999; *Lee et al.*, 2004]. NCD films have larger grain boundary areas, which contain sp^2 bonds and provide conduction paths for electrons, facilitating the electron transport in the NCD films.

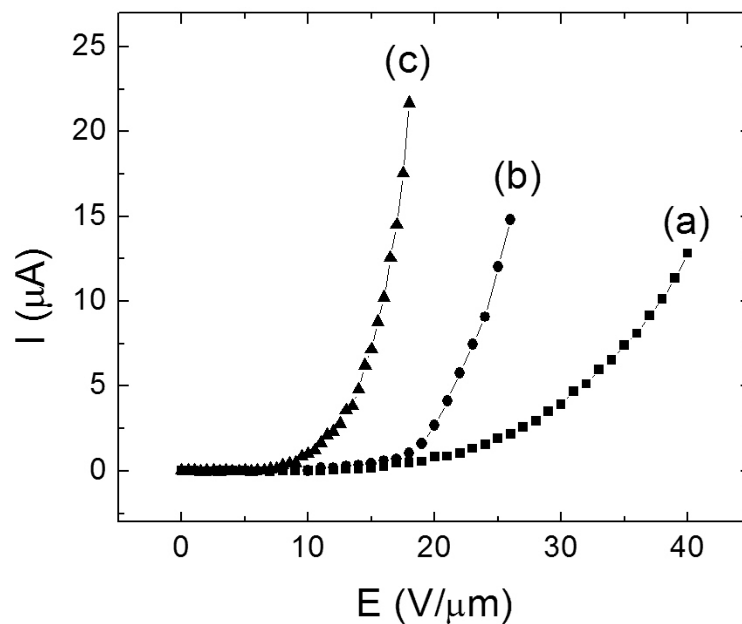

Figure 5.5: FEE current vs. electric field curves of the diamond films grown at various gas flow rates (sccm): (a) 200, (b) 300, and (c) 400.

Table 3: Typical FEE parameters of diamond films grown at various gas flow rates (sccm): 200, (b) 300, and (c) 400.

Gas flow rate (sccm)	200	300	400
Diamond films	Well-faceted MCD	Randomly oriented submicron diamond	NCD
Turn on electric field (V/μm)	11	10	6
Emission current (μA) at 18 V/μm	0.5	1.1	21.7

For tribological and optical applications, it is highly desirable to deposit smooth films with small (nanosized) grain. The NCD films with cauliflower morphology obtained at high gas flow rate have a relatively high surface roughness of 244 nm as measured by AFM. An experiment to reduce surface roughness was performed in which a positive biasing of 300 volts is continuously applied during the diamond growth stage. Figure 5.6a shows the SEM micrograph of a sample grown at a gas flow rate of 400 sccm with positive biasing. A more detailed AFM image of this surface shown in Fig. 5.6b is obtained from intermittent contact mode measurements using a high resolution cantilever. It clearly shows that the fine grains with an average grain size of approximately 12 nm (from AFM analyses) congregate together to form larger clusters of approximately 700-1000 nm, much smaller than the clusters in Fig. 5.2b. The root mean square surface roughness is approximately 37 nm over the 20 μm × 20 μm area, much smaller than the NCD films grown without positive bias. The results show that positive substrate biasing is beneficial to grow NCD diamond films with a smoother surface.

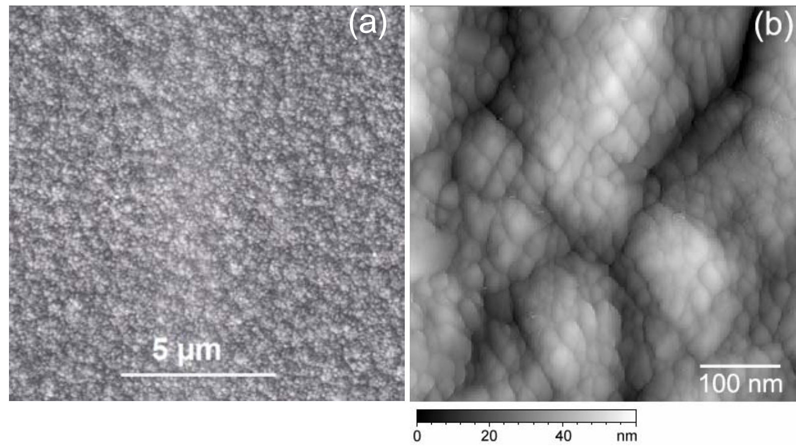

Figure 5.6: Morphology of the NCD film grown at a flow rate of 400 sccm with a positive biasing during the diamond growth stage: (a) SEM image, and (b) 0.5×0.5 μm^2 AFM image.

It is well known that a high secondary nucleation rate is of critical importance to synthesize NCD. To promote the secondary nucleation, various growth environments were employed to synthesize NCD. Some researchers mixed inert gases with the carbon precursors such as Ar/C_{60} [*Gruen et al.*, 1994], Ar/CH_4 [*McCauley et al.*, 1998], $Ar/CH_4/H_2$ [*Zhou et al.*, 1998]. Others applied negative bias and used CH_4/H_2 gas mixtures [*Gu* and *Jiang*, 2000; *Sharda* and *Umeno*, 2000]. Experiments were also performed by increasing the methane concentration and it has been confirmed that an increase in diamond growth precursor flux enhances secondary nucleation and leads to NCD growth [*Chen et al.*, 2001].

It should be pointed out that a favorable condition for NCD growth is achieved in our experiments by only increasing the total gas flow rate, an approach quite different from those employed by other researchers (increasing the methane concentration, substrate biasing, and addition of other gases). It is known that the quality of CVD diamond from CH_4/H_2 gas mixtures is controlled by the ratio of the carbon radicals to the atomic hydrogen ($[C_xH_y]/[H_{at}]$) on the diamond growth surface. This ratio

determines the competition between individual diamond grain growth and diamond nucleation. When the ratio is small, initial diamond nuclei have enough time to fully develop before secondary nucleation. When the ratio is large, the secondary nucleation inhibits the diamond grain growth. Consequently, a diamond film with much smaller grain size develops. The ratio of the carbon radicals to the atomic hydrogen can be controlled by experimental conditions such as substrate temperature, methane concentration, and substrate biasing. Similar to the increase of methane concentration or applying substrate biasing, the increase of gas flow rate may also increase the incident flux of diamond growth precursor (C_xH_y, radicals such as CH_3, C_2) to the growing surface, as reported by Celii *et al.* [*Celii et al.* 1991; *Celii et al.* 1992]. Their numerical simulations of the convective gas flow pattern in their reactor modeled the convective vortices above the substrates at various gas flow rates from 25 to 800 sccm and found that the ratio between convection and mass-related diffusion determines the concentration of the heavier carbon-containing species in the lighter hydrogen gas. At high flow rate, diffusion and convection are equally important. While the residence time of the rapid diffusion of atomic hydrogen is not significantly altered, the residence time of heavier carbon-containing species is sensitive to the change in gas flow pattern. The flux of carbon-containing species on the diamond growth surface is higher at higher flow rate. Celii *et al.* suggested that the changes in the flux of carbon-containing species with the gas flow rate were responsible for the changes in the morphology of the deposited diamond films. Similarly, deposition of NCD films at high flow rate in the experiments presented in this thesis may be attributed to an increase of the effective concentration of carbon-containing species which favors secondary nucleation. Furthermore, continuous positive substrate biasing in the diamond growth stage might further enhance nucleation since the biasing causes some surface-related effects such as

enhanced surface diffusion due to electron heating or more carbon-containing species decomposed near the substrate surface due to the strong electric field.

5.4 Conclusion

The effects of the gas flow rate on the growth of diamond films have been investigated using microwave plasma CVD. Highly oriented MCD films have been obtained at low gas flow rates while NCD films are formed at high flow rates. The results show that the gas flow rate is an important parameter influencing the nucleation and growth of diamond thin films. Synthesis of NCD films has been demonstrated by simply increasing the gas flow rate. The growth of NCD at high gas flow rate may be attributed to higher fluxes of diamond growth precursors toward the substrate as suggested by numerical simulations [*Celii et al.*, 1991]. Field electron emission characterization shows that NCD films grown at high flow rate have better FEE properties compared to their MCD counterpart grown at low flow rate. Furthermore, experiments reported here have also demonstrated that a positive substrate biasing during the growth stage at higher gas flow rate is beneficial for depositing NCD films with smoother surfaces which are desired in tribological and optical applications.

Chapter 6

Synthesis of high purity tungsten-based nanostructures

Tungsten and tungsten oxide nanostructured films are promising candidate materials for many technological applications such as field emission devices and semiconductor sensors. Various techniques have been used for the synthesis of these materials. However, studies on the synthesis of crystalline tungsten-based nanomaterials with high purity are still rare. This chapter reports on an effective synthesis method to synthesize high purity straight tungsten nanorods or tungsten oxide nanorods through optimization of the tungsten filament temperature in a hot filament reactor.

6.1 Introduction

In the past decade, developing methodologies to prepare one-dimensional nanostructured materials has attracted great attention because of the superior properties of materials due to nanoscale structure. Metallic tungsten has well-known chemical, physical, electrical, and mechanical properties suitable for various applications including thermal electron emission [*Yih* and *Wang*, 1979], and field electron emitters [*Choi et al.*, 2002b]. Tungsten oxides have also been developed for uses in

electrochromic devices [*Franke et al.*, 2000; *Santato et al.*, 2001], gas sensors [*Lee et al.*, 2000; *Boulova et al.*, 2001; *Solis et al.*, 2001], photo-catalysts [*Li et al.*, 2000; *Bamwenda* and *Arakawa*, 2001], and superconducting materials [*Aird et al.*, 1998]. Because of the distinct and promising properties of tungsten and tungsten oxide, tungsten-based nanostructured films are expected to have wide technological applications in many areas such as scanning tunneling microscope (STM) tips, field emission devices, and building blocks for terabit-level interconnection, nanomachine components and semiconductor sensors.

Recently, tungsten nanostructures have been realized using several different synthetic approaches, including hot filament vapor synthesis [*Vaddiraju et al.*, 2003], thermal treatment of sputtered tungsten film [*Lee et al.*, 2002], oblique-angle sputter deposition [*Karabacak et al.*, 2003], and field-emission induced growth [*Thong et al.*, 2002]. Synthesis of tungsten oxide nanostructures has also been the subject of active research. For example, thermal oxidation evaporation growth [*Zhu et al.*, 1999; *Liu et al.*, 2003; *Li et al.*, 2003a], and solvo-thermal reactions [*Li et al.* 2003b; *Zhang et al.*, 2005] have been investigated. However, studies on controlled growth of crystalline tungsten-based nanomaterials with high purity are still rare.

In the present study, synthesis of high purity tungsten and tungsten oxide nanorods is investigated by using a HFCVD reactor with various tungsten filament temperatures under flowing argon gas. The method used provides a relatively simple, yet effective route to synthesizing tungsten-based nanomaterials of high purity.

6.2 Experiment

The HFCVD system is used for the synthesis experiments. The distance between the filament and substrate is 5 mm. To get different temperatures from 1200 ℃ to 2330 ℃

for the deposition, various ac currents (60 Hz) are applied to heat the tungsten coil. Prior to the deposition under flowing argon gas (the purity of argon is 99.997%, the flow rate is 50 sccm) at pressure of 260 Pa for 20 h, the reactor is evacuated down to 1 Pa by a rotary pump.

6.3 Results and discussion

Figure 6.1 shows typical SEM morphologies of films deposited at different filament temperatures. At filament temperature of 1800 ℃, sub-micron semi-spherical particles exist (Fig. 6.1a) in the film. At filament temperatures of 1940 ℃, sub-micron size rod-like bundles can be found (Fig. 6.1b). After deposition at temperature above 2000 ℃, straight nanorod films cover the entire substrate surface, as shown in Fig. 6.1c and Fig. 6.1d.

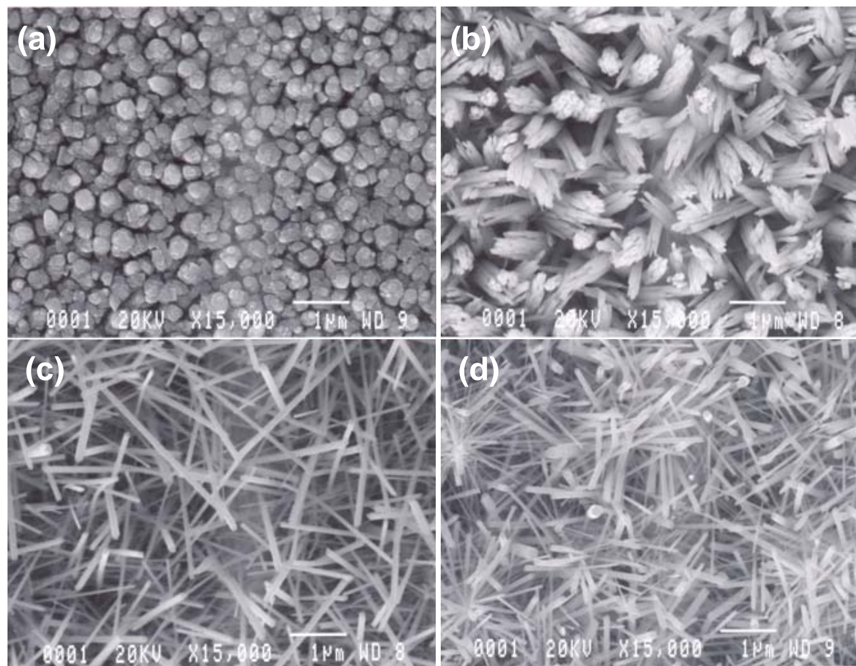

Figure 6.1: (a) Typical SEM micrographs of samples deposited at different filament temperatures: (a) 1600 ℃; (b) 1940 ℃; (c) 2000 ℃; (d) 2280 ℃.

Typical TEM and High Resolution Electron Microscopy (HREM) images of the nanorods formed with filament temperature of 2140 ℃ are shown in Fig. 6.2. It reveals that it is a solid rod (Fig. 6.2b). Both SEM and TEM images clearly show that the films synthesized at higher filament temperatures (above 2000 ℃) have nanorod structures. The rods are straight and relatively long, ranging from 1 to 5 μm, and have a relatively broad distribution of diameters, ranging from 4 to 200 nm; the aspect ratio (length/diameter) is up to 50. The diameter of each nanorod appears to be uniform along the entire length.

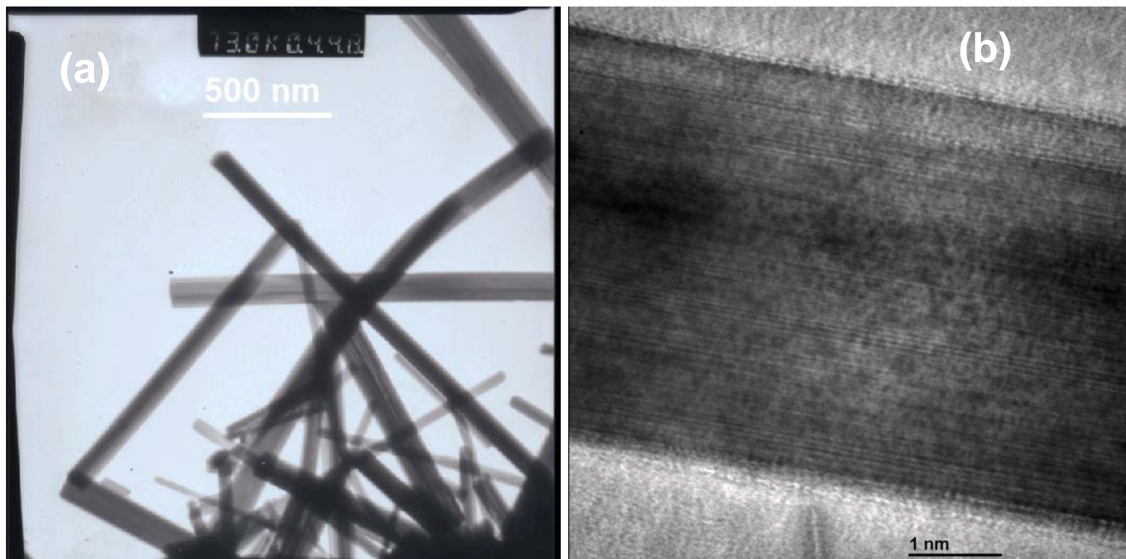

Figure 6.2: (a) Typical TEM image of nanorods deposited at a filament temperature of 2140 ℃; (b) HREM image of a nanorod deposited at a filament temperature of 2140 ℃.

Figure 6.3 shows the typical XRD patterns of the samples prepared at different filament temperatures. The phases in the deposited films are bcc (body-centered cubic) α-W and WO_{2+x} ($W_{24}O_{68}$) as well as monoclinic WO_2 (curve a). For the films deposited at 2000 ^{o}C, only $W_{24}O_{68}$ peaks are detectable. In the film deposited at 2140 ℃, the

peaks from both bcc W and $W_{24}O_{68}$ phases were identified (curve b). At 2240 ℃, bcc W peaks are much more significant compared with tungsten oxide peaks and the $W_{24}O_{68}$ peaks are replaced by WO_2 peaks. Further increasing temperature up to 2280 ℃, only bcc W peaks can be detected (curve d), indicating its high bcc W phase content.

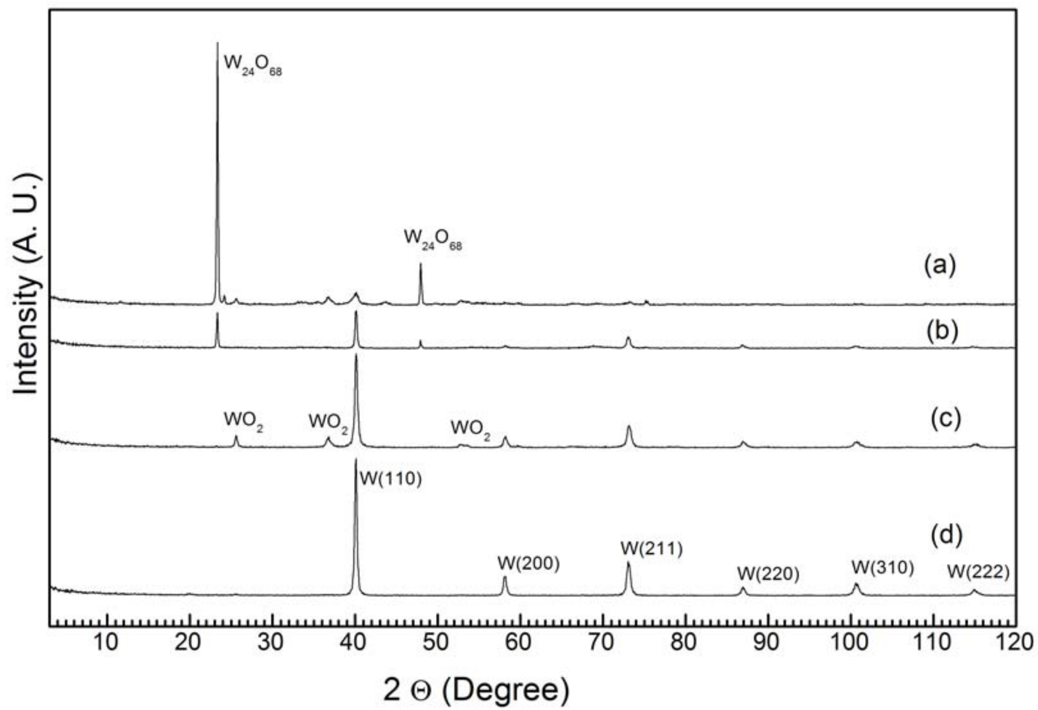

Figure 6.3: XRD patterns of nanorods grown at different filament temperatures: (a) 2000 ℃; (b) 2140 ℃; (c) 2240 ℃; (d) 2280 ℃.

Figure 6.4 shows the temperature dependence of the ratio of the main tungsten peaks (at 40.1°) to that of tungsten oxides ($W_{24}O_{68}$ at 23.3° or WO_2 at 25.6°). It is nearly zero (pure tungsten oxides were deposited) for films deposited at temperatures below 2100 ℃, and increases significantly with increasing filament temperatures above 2100 ℃. When the temperature reaches 2280 ℃, pure tungsten nanorods are obtained.

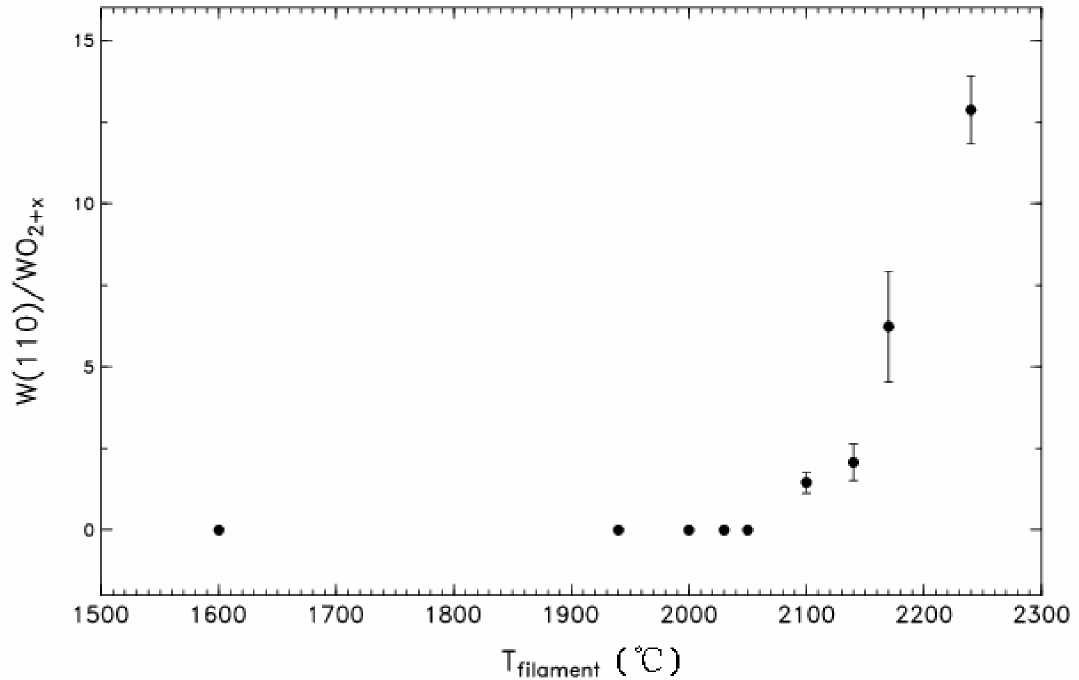

Figure 6.4: Integrated area ratio of main peak of W to the WO_{2+x} main peak in XRD measurements from samples grown at different filament temperatures. Each point in the error bar represents an average of 6 samples grown on the same condition.

It is hypothesized that the formation of tungsten or tungsten oxide nanorods presented in this work is within the framework of vapor-solid (VS) growth mechanism. Oxidation of the filament plays an important role in the growth of the tungsten-related nanorods. In the presence of oxygen, tungsten oxides, such as WO_3 and WO_2, can easily form on the solid surface at temperatures higher than 400 ℃, and at temperatures above 1300 ℃ those tungsten oxides are quickly evaporated [*Yih* and *Wang*, 1979; *Kofstad*, 1968]. There was no oxygen introduced into the system on purpose. It is speculated that the presence of tungsten oxides in our samples was due to the oxidation between tungsten and residual oxygen released from the glass chamber or the leakage of air through seals in our vacuum system. Part of the tungsten oxide undergoes some thermal

decomposition when heated in an inert gas, producing metallic tungsten according to the reaction [*Bai et al.*, 1973; *Kofstad*, 1968; *Blackburn et al.*, 1958; *Macintyre*, 1992],

$$3WO_2 \rightarrow W + 2WO_3 \qquad (6\text{-}1)$$

or [*Vaddiraju et al.*, 2003],

$$WO_2 \rightarrow W + O_2 \qquad (6\text{-}2)$$

and [*Vaddiraju et al.*, 2003]

$$2WO_3 \rightarrow 2W + 3O_2 \qquad (6\text{-}3)$$

The condensation of these diffused vapor species (either tungsten oxide or tungsten vapor) on the substrate at lower temperatures causes the nucleation and growth of the films. XRD measurements indicate that the filament temperature strongly affects the ratio of the α-W phase to the tungsten oxide phase. The tungsten phase increases significantly as the filament temperature increases. The mechanism is not fully understood yet.

To clarify the role of tungsten oxidation in the synthesis of tungsten nanostructures, a similar experimental setup was used as for diamond and carbon nanotube growth in the same reactor (see Chapter 3.2). In that experiment, hydrogen diluted with methane gas (around 1% CH_4), instead of argon gas, was used. No tungsten was detected in the deposited films. Another series of experiments was conducted under similar conditions to grow tungsten-based nanorods by using pure hydrogen gas, instead of pure argon gas. After 20 hours of filament heating, no deposition was found on the substrates, based on the SEM and XRD analyses. This could be due to the reaction between hydrogen and oxygen at high temperature, the hydrogen-rich gas serving as a reduction agent thus inhibiting the oxidization of the tungsten filament; the evaporation of pure tungsten is difficult at these temperatures. These results provide indirect evidence to support the proposed explanation that the oxidation of tungsten and the

decomposition of the evaporated tungsten oxides are keys for the formation of tungsten and tungsten oxides nanorods.

As mentioned above the filament temperature also has an effect on the morphology of the samples (see Fig. 6.1). Sub-micron particles (Fig. 6.1a) or quasi-nanorod (Fig. 6.1b) were obtained when the filament temperature is lower than 2000 ℃, while higher filament temperatures result in nanorods (Fig. 6.1c and Fig. 6.1d). This observation may be explained by the correlation of the critical nuclei diameter d_c with the experimental parameters [*Vaddiraju et al.*, 2003], higher filament temperature results in smaller critical nuclei diameter. For condensation of the vapor phase species, the critical nuclei diameter, d_c, depends on the supersaturation by the relation [*Tiller*, 1991],

$$d_c = 4\sigma\Omega/[RT\ln(p/p^*)] \qquad (6\text{-}4)$$

where σ is the interfacial energy, R is gas constant (8.134 $JK^{-1}mol^{-1}$), Ω is the molar volume, T is the temperature of the substrate, p is the partial pressure of the growth species, and p^* is the vapor pressure of the growth species at equilibrium. Both p and p^* are functions of temperature. As the filament temperature increases, the supply of the participation vapor phase species, that is, p, increases along with the increase in p^*.

6.4 Conclusion

Tungsten oxide, metallic tungsten and their mixed nanorod films have been synthesized in a HFCVD reactor. The effect of filament temperature on the structure of nanorod films has been investigated. The controlled growth of high purity tungsten oxide and metallic tungsten nanorod films has been realized by tuning the filament temperature. The method developed provides a relatively simple, yet effective route to synthesizing

one-dimensional tungsten-based nanomaterials of high purity. The growth mechanisms have been discussed based on oxygen assisted evaporation of filament and the decomposition of tungsten oxide vapor at high temperatures.

Chapter 7

Conclusions and future work

7.1 Conclusions

The main findings made in the work are as follows:

1) The effects of the substrate bias polarity on the growth of carbon films in an HFCVD reactor were investigated [*Chen et al.*, 2005]. It has been found that positive bias increased the diamond nucleation density on a bare silicon substrate. On the other hand, negative biasing promotes the deposition of dense, well-aligned carbon nanocones. The orientation of the carbon nanocones appears to align with the direction of the electric field lines near the substrate surface.

2) The growth of carbon nanotubes on Ni-coated silicon substrates using HFCVD in a CH_4/H_2 gas mixture under various substrate biasing conditions was investigated [*Yang et al.*, 2003]. In the cases of positive substrate biasing, no substrate biasing with or without a glow discharge, or negative substrate biasing without a glow discharge, randomly-oriented nanotubes were deposited. Well-aligned nanotubes with variable orientations can be only synthesized with a glow discharge by negative substrate biasing. A gradual deviation of the nanotube orientation with respect to the substrate normal has been observed near the sample edges. The results suggest that the electric field is a determining factor for the alignment, and the alignment orientation is likely determined

by the direction of electric field lines on the sample surface. The orientation of CNTs can be controlled by adjusting the working pressure which affects the thickness of the cathode fall region and thus the direction of electric field line near the edge region of the substrate.

3) The carbon source also influences diamond growth. In this thesis work, experiments were performed to investigate diamond nucleation and growth by graphite etching at low substrate temperatures. Results show that diamond can be synthesized at temperatures as low as 250 ℃ by etching graphite in a pure microwave hydrogen plasma [*Yang et al.*, 2005]. This newly developed diamond synthesis technique uses in situ graphite etching as a carbon source instead of conventional hydrocarbon gases, and has several advantages over the conventional process including deposition at unusually low temperature, higher growth rate, lower concentration of sp^2 bonded carbon, and reduced carbon contamination of the reactor. The methodology may open a pathway to coating pure diamond films on steels and on low softening- or melting-point materials including glass and aluminum.

4) The feasibility of the deposition of diamond films on steel materials was investigated. Carbon soot was formed on steel substrates (mild steel and stainless steel) using graphite etching at low substrate temperature. After depositing an aluminum interlayer on either carbon steel or stainless steel substrates, continuous diamond films have been successfully deposited on the interlayer at low temperatures by the in situ graphite etching technique, suggesting that the Al-interlayer prevented graphitization and increased diamond nucleation density.

5) The gas flow rate is an important parameter for CVD diamond growth because the gas flow rate is closely related to the gas transport in the CVD reactor [*Chen et al.*, 2006a]. The effects of the gas flow rate on the growth of diamond films were

investigated using microwave plasma CVD. Highly oriented MCD films have been obtained at low gas flow rates while NCD films are formed at high flow rates. The results show that the gas flow rate is an important parameter influencing the nucleation and growth of diamond thin films. The synthesis of NCD films has been demonstrated by simply increasing the gas flow rate. The growth of NCD at high gas flow rate may be attributed to higher fluxes of diamond growth precursors toward the substrate. Field electron emission characterization shows that NCD films grown at high flow rate have better FEE properties compared to their MCD counterpart grown at low flow rate. Furthermore, our experiments have also demonstrated that a positive substrate biasing during the growth stage at higher gas flow rate is beneficial for depositing NCD films with smoother surfaces.

6) Tungsten oxide, metallic tungsten and their mixed nanorod films have been synthesized in a hot filament CVD reactor. The effect of filament temperature on the structure of the nanorod films has been investigated [*Chen et al.*, 2006b]. The controlled growth of high purity tungsten oxide and metallic tungsten nanorod films have been realized by tuning the filament temperature. The method developed provides a relatively simple, yet effective route to synthesizing one-dimensional tungsten-based nanostructures of high purity. The growth mechanisms have been discussed based on oxygen assisted evaporation of filament and the decomposition of tungsten oxide vapor at high temperatures.

7.2 Suggestions for future work

The experimental results in this thesis show that experimental factors play important roles in controlling the nucleation and growth of diamond and carbon nanostructures.

Some plausible mechanisms were proposed to understand these effects. For example, our experimental results show the strong dependence of diamond properties on gas flow rate. However, no direct experimental study on the gas phase chemistry has been performed to understand the exact mechanism. So, the first issue of future work from this thesis is to use gas phase characterization techniques to observe the variation of plasma chemistry to better understand the mechanisms. For gas phase characterization, molecular beam mass spectrometry or optical emission spectroscopy may be employed since they are capable of providing quantitative measurements of both stable free radical gas-phase species under conditions typical in the CVD process. In addition, numerical fluid simulation based on the specific MWCVD reactor used should be carried out when the software becomes available or developed.

Secondly, it is necessary to study the properties of the diamond film from the point of view of practical applications. For example, in this thesis work, nanocrystalline diamond films with smooth surfaces which may be beneficial for optical applications have been deposited. However, due to the lack of further properties characterization facility, the optical properties have not been characterized to investigate the feasibility of these smooth nanocrystalline diamond films for optical applications. Also, the deposition of continuous diamond on steel materials at low temperature has been realized. The low growth temperature in our experiment is expected to reduce the stress due to the difference of thermal expansion of the diamond film and the steel substrate. For practical applications, the adhesion of the diamond film with steel substrate needs to be critically investigated. Generally, more characterization of the properties of diamond films from the point of view of practical applications will be an issue for future work if facilities become available.

References

J.W. Ager, D.K. Veirs, and G.M. Rosenblatt, *Phys. Rev. B* **43**, 6491 (1991).

A. Aird A, M.C. Domeneghetti, F. Mazzi, V. Tazzoli, and E.K.H. Salje, *J. Phys.: Condens. Matter* **10**, L569 (1998).

J.C. Angus and C.C. Hayman, *Science* **241**, 913-921 (1988).

M.N.R. Ashfold, P.W. May, C.A. Rego, and N.M. Everitt, *Chem. Soc. Rev.* **23**, 21 (1994).

M. Asmann, J. Heberlein, and E. Pfender, *Diam. Relat. Mater*. **8**, 1 (1999).

P.K. Bachmann, W. Drawl, D. Knight, R. Weimer, and R. Messier, *Mater. Res. Soc. Symp. Proc.* **EA-15**, 99 (1988).

J.C. Bailar, H.J. Emeleus, S.R. Nyholm, and A.F. Trotman-Dichenson, *Comprehensive inorganic chemistry,* Pergamon (1973).

G.R. Bamwenda and H. Arakawa, *Appl. Catal. A* **210**, 181 (2001).

P.E. Blackburn, M. Hoch, and H.L. Johnston, *J. Phys. Chem.* **62**, 769 (1958).

M. Boulova, A. Gaskov, and G. Lucazeau, *Sens. Actuators B* **81**, 99 (2001).

C. Bower, W. Zhu, S. Jin, and O. Zhou, *Appl. Phys. Lett.* **77**, 830 (2000).

H. Buchkremer-Hermanns, H. Ren, and H. Weiß, *Diam. Relat. Mater.* **5**, 312 (1996).

F.P. Bundy, H. T. Hall, H. M. Hall, *et al.*, *Nature* **176**, 51 (1955).

F.G. Celii, D. White, Jr., and A.J. Purdes, *J. Appl. Phys.* **70**, 5636 (1991).

F.G. Celii, D. White, Jr., and A.J. Purdes, *Thin Solid Films* **212**, 140 (1992).

L.C. Chen, P.D. Kichambare, K.H. Chen, J.-J. Wu, J.R. Yang, and S.T. Lin, *J. Appl. Phys.* **89**, 753 (2001).

W. Chen, C. Xiao, Q. Yang, A. Moewes, and A. Hirose, *Can. J. Phys.* **83**, 753 (2005).

W. Chen, X. Lu, Q. Yang, C. Xiao, R. Sammynaiken, J. Maley, and A. Hirose, *Thin Solid Films* **515**, 1970 (2006a).

W. Chen, C. Xiao, Q. Yang, S. Yang, and A. Hirose, *Mater. Res. Innov.* **10**, 169 (2006b).

F. F. Chen, *Introduction to plasma physics and controlled fusion*, Plenum Press (1984).

M. Chhowalla, K.B.K. Teo, C. Ducati, N.L. Rupesinghe, G.A.J. Amaratunga, A.C. Ferrari *et al.*, *J. Appl. Phys.* **90**, 5308 (2001).

http://www.chm.bris.ac.uk/pt/diamond/theses.htm

G.S. Choi, Y.S Cho, S.Y. Hong, J.B. Park, K.H. Son, and D.J. Kim., *J. Appl. Phys.* **91**, 3847 (2002a).

C.H. Choi, Y.T. Jang, B.K. Ju, Y.H. Lee, M.H. Oh, J.H. Ahn, and N.K. Min, *SID Digest* **3301**, 369 (2002b).

C.T. Colbert, *Fullerenes and Nanotubes, Nanotechnology Research Directions, IWGN Worksop Report* (1999) (http://itri.loyola.edu/nano/IWGN.Research.Directions/), p. 55.

J. Cui, and R. Fang, *J. Phys. D* **29**, 2759 (1996).

H. Dai, J. H. Hafner, A. G. Rinzler, D. T. Colbert, and R. E. Smalley, *Nature* **384**, 147 (1996).

W. A. de Heer, A. Chatelain, and D. Ugarte, *Science* **270**, 1179 (1995).

M. S. Dresselhaus, G. Dresselhaus, and P. Avouris, *Carbon nanotubes: synthesis, structure, properties, and applications*, Springer (2001).

T.W. Ebbesen and P.M. Ajayan, *Nature* **358**, 220 (1992).

http://en.wikipedia.org/wiki/Allotropes_of_carbon/.

Q.H. Fan, E. Pereira, and J. Cracio, *J. Mater. Sci.* **34**, 1353 (1999).

P.E.J. Flewitt and R.K. Wild, *Physical Methods for Materials Characterisation*, IOP Publishing (1994).

E.B. Franke, C.L. Trimble, J.S. Hale, M. Schubert, and J.A. Woollam, *J. Appl. Phys.* **88**, 5777 (2000).

M. Funer, C. Wild, and P. Koidl, *Surf. Coat. Technol.* **74-5**, 221 (1995).

E. G. Gamaly and T. W. Ebbesen, *Phy. Rev. B* **52**, 2083 (1995).

A. Gicquel, K. Hassouni, S. Farhat, Y. Breton, C. D. Scott, M. Lefebvre, and M. Pealat, *Diam. Relat. Mater.* **3**, 581 (1994).

O. Glozman, A. Berner, D. Shechtman, A. Hoffman, *Diam. Relat. Mater.* **7**, 597 (1998).

D.M. Gruen, S. Liu, A.R. Krauss, J. Luo, and X. Pan, *Appl. Phys. Lett.* **64**, 1502 (1994).

D.M. Gruen, *Annu. Rev. Mater. Sci.* **29**, 211 (1999).

C.Z. Gu and X. Jiang, *J. Appl. Phys.* **88**, 1788 (2000).

Y. Hayashi, T. Negishi, and S. Nishino, *J. Vac. Sci. Technol. A* **19**, 1796 (2001).

G.E. Harlow, *The nature of diamonds*, Cambridge University Press (1998).

A. Heiman, I. Gouzman, S.H. Christiansen, H.P. Strunk, G. Comtet, L. Hellner, G. Dujardin, R. Edrei, and A. Hoffman, *J. Appl. Phys.* **89**, 2622 (2001).

A. Hiraki, *Mater. Chem. Phys*. **72**, 196 (2001).

W.L. Hsu, *J. Vac. Sci. Technol. A* **6**, 1803 (1988).

B.R. Huang, C.T. Chia, M.C. Chang, and C.L. Cheng, *Diam. Relat. Mater.* **12**, 26 (2003).

S. Iijima, *Nature* **354**, 56 (1991).

Y.T. Jan, H.C. Hsieh, and C.F. Chen, *Diam. Relat. Mater.* **8**, 772 (1999).

JCDPS Powder Diffraction File; International Centre for Diffraction Data, Swarthmor (1990).

X. Jiang, C. P. Klages, R. Zachai, M. Hartweg, and H.J. Füsser, *Appl. Phys. Lett.* **62**, 3438 (1993).

T. Karabacak, A. Mallikarjunan, J.P. Singh, D. Ye, G.C. Wang, and T.M. Lu, *Appl. Phys. Lett.* **83**, 3096 (2003).

P. Kofstad, *High-temperature oxidation of metals*, Wiley Press (1968).

E. Kondoh, T. Ohta, T. Mitomo, and K. Ohtsuka, *J. Appl. Phys.* **73**, 3041 (1993).

H. W. Kroto, J. R. Heath, S. C. O'Brien, R. F. Curl, and R. E. Smalley, *Nature* **318**, 162 (1985).

K.H. Lee, Y.K. Fang, W.J. Lee, J.J. Ho, K.H. Chen, and K.C. Liao, *Sens. Actuators B* **69**, 96 (2000).

Y.H. Lee, C.H. Choi, Y.T. Jang, E.K. Kim, B.K. Ju, N.K. Min, and J.H. Ahn, *Appl. Phys. Lett.* **81**, 745 (2002).

Y.C. Lee, S.J. Lin, C.T. Chia, H.F. Cheng, and I.N. Lin, *Diam. Relat. Mater.* **13**, 2100 (2004).

J.C. Lee, B.Y. Hong, R. Messier, and R.W. Collins, *J. Appl. Phys.* **80**, 6489 (1996).

F.B. Li, G.B. Gu, X.J. Li, and H.F. Wan, *Acta Phys.-Chim. Sinica* **16**, 997 (2000).

Y.B. Li, Y. Bando, D. Golberg, and K. Kurashima, *Chem. Phys. Lett.* **367**, 214 (2003a).

X.L. Li, J.F. Liu, and Y.D. Li, *Inorg. Chem.* **42**, 921 (2003b).

W. Z. Li, S. S. Xie, L. X. Qian, *et al.*, *Science* **274**, 1701 (1996).

M. A. Lieberman and A. J. Lichtenberg, *Principles of Plasma Discharges and Materials Processing*, Wiley Press (1994).

J. Liu, Y. Zhao, and Z. Zhang, *J. Phys.: Condens. Matter* **15**, L453 (2003).

X. Lu, Q. Yang, C. Xiao, and A. Hirose, *Appl. Phys. A* **82**, 293 (2005).

J.E. Macintyre (Ed), *Dictionary of inorganic compounds, volumes 3*, Chapman & Hall Press, (1992).

S. Matsumoto, Y. Sato, M. Tsutsumi, and N. Setaka, *J. Mater. Sci.* **17**, 3106 (1982).

T.G. McCauley, D.M. Gruen, and A.R. Krauss, *App. Phys. Lett.* **73**, 1646 (1998).

V.I. Merkulov, A.V. Melechko, M.A. Guillorn, M.L. Simpson, D.H. Lowades, J.H. Whealton, and R.J. Radidon, *Appl. Phys. Lett.* **80**, 4816 (2002).

R.J. Nemanich, J.T. Glass, G. Lucovsky, and R.E. Shroder, *J. Vac. Sci. Technol. A* **6**, 1783 (1988).

M. Nesladek, J. Spinnewyn, C. Asinari, R. Lebout, and R. Lorent, *Diam. Relat. Mater.* **3**, 98 (1994).

http://nobelprize.org/educational_games/physics/microscopes/tem/index.html/.

T. Ono, H. Miyashita, and M. Esashi, *Nanotechnology* **13**, 62 (2002).

M. R. Pederson and J. Q. Broughton, *Phys. Rev. Lett.* **69**, 2689 (1992).

J.R. Petherbridge, P.W. May, S.R.J. Pearce, K.N. Rosser, and M.N.R. Ashfold, *J. Appl. Phys.* **89**, 1484 (2001).

R. Pfeiffer, H. Kuzmany, P. Knoll, S. Bokova, N. Salk, and B. Gunther, *Diam. Relat. Mater.* **12**, 268 (2003).

http://physicsweb.org/articles/world/13/6/8/1/pw-13-06-08fig6/.

S. Prawer, K.W. Nugent, D.N. Jamieson, J.O. Orwa, L.A. Bursill, and J.L. Peng, *Chem. Phys. Lett.* **332**, 93 (2000).

S. Proffitt, C.H.B. Thompson, A. Gutierrz-Sosa, N. Paris et al., *Diam. Relat. Mater.* **9**, 246 (2000).

H. Rau and F. Picht, *J. Mater. Res.* **7**, 934 (1992).

Z. F. Ren, Z. P. Huang, J. W. Xu, J. H. Wang, P. Bush, M. P. Siegal, and P. N. Provencio, *Science* **282**, 1105 (1998).

L.H. Robin, E.N. Farabaugh, and A. Feldman, *J. Mater. Res.* **5**, 2456 (1990).

S.R. Sails, D.J. Gardiner, M. Bowden, J. Savage, and D. Rodway, *Diam. Relat. Mater.* **5**, 589 (1996).

C. Santato, M. Odziemkowaski, M. Ulmann, and J. Augustynski, *J. Am. Chem. Soc.* **123**, 10639 (2001).

I. Schmidt and C. Benndorf, *Diam. Relat. Mater.* **10**, 347 (2001).

S. Schwarz, Y. Musayer, S.M. Rosiwal, C. Schaufler, R.F. Singer, and H. Meekamm, *Diam. Relat. Mater.* **11**, 757 (2002).

H. Sein, W. Ahmed, C.A. Rego, A.N. Jones, M. Amar, M. Jackson, and R. Polini, *J. Phys.: Condens. Matter.* **15**, S2961 (2003).

T. Sharda and M. Umeno, *Appl. Phys. Lett.* **77**, 4304 (2000).

J.L. Solis, S. Saukko, L. Kish, C.G. Granqvist, and V. Lantto, *Thin Solid Films* **391**, 255 (2001).

S.A. Solin and K. Ramdas, *Phys. Rev. B* **1**, 1687 (1970).

K. Spear, *J. Amer. Ceram. Soc.* **7**, 171 (1989).

J.T.L Thong, C.H. Oon, M. Yeadon, and W.D. Zhang, *Appl. Phys. Lett.* **81**, 4823 (2002).

W.A. Tiller, *The Science of Crystallization: Microscopic Interfacial Phenomena*, Cambridge University Press (1991).

F. Tuinstra and J. L. Koenig, *J. Chem. Phys.* **53**, 1126 (1970).

S. Vaddiraju, H. Chandrasekaran, and M.K. Sunkara, *J. Am. Chem. Soc.* **125** 10792 (2003).

J.B. Wachtman, *Characterization of materials*, Manning Press (1993).

N. Wada and S.A. Solin, *Physica B* **105**, 353 (1981).

P.S. Weiser, S. Prawer, A. Hoffman, R.R. Manory, P.J.K. Paterson, and S.A. Stuart, *J. Appl. Phys.* **72**, 4643 (1992).

P.S. Weiser and S. Prawer, *Diam. Relat. Mater.* **4**, 710 (1995).

X. Xiao, J. Birrell, J.E. Gerbi, O. Auciello, and J.A. Carlisle, *J. Appl. Phys*. **96**, 2232 (2004).

Q. Yang, C. Xiao, W. Chen, A.K. Singh, T. Asai, and A. Hirose, *Diam. Relat. Mater.* **12**, 1482 (2003).

Q. Yang, W. Chen, C. Xiao, A. Hirose, and M. Bradley, *Carbon* **43**, 2635 (2005).

W.A. Yarbrough and R. Messier, *Science* **247**, 3842 (1990).

W.A. Yarbrough, *J. Mater. Res.* **7**, 379 (1992).

S.W.H. Yih and C.T. Wang, *Tungsten: sources, metallurgy, properties, and applications*, Plenum Press (1979).

M. Yoshikawa, G. Katagiri, H. Ishida, and A. Ishitani, *Sol. Stat. Comm.* **66**, 1177 (1988).

J. Yu, R. Huang, L. Wen, and C. Shi, *J. Matt. Sci. Lett.* **17**, 1011 (1998).

J. Yu, R. Huang, L. Wen, and C. Shi, *Mater. Res. Bull.* **34**, 2319 (1999).

S. Yugo, T. Kimura, and T. Muto, *Vacuum* **41**, 1364 (1990).

S. Yugo, T. Kanai, T. Kimura, and T. Muto, *Appl. Phys. Lett.* **58**, 1036 (1991).

B. Zhang, C. Cao, H. Qiu, Y. Xu, Y. Wang, and H. Zhu, *Chem. Lett.* **34**, 154 (2005).

X.T. Zhou, Q. Li, F.Y. Meng, I. Bello, C.S. Lee, S.T. Lee, and Y. Lifshitz, *Appl. Phys. Lett.* **80**, 3307 (2002).

D. Zhou, D.M. Gruen, L.C. Qin, T.G. McCauley, and A.R. Krauss, *J. Appl. Phys.* **84**, 1981 (1998).

W. Zhu, C.A. Randall, A.R. Badzian, and R. Messier, *J. Vac. Sci. Technol. A,* **7**, 2315 (1989).

Y.Q. Zhu, W. Hu, W.K. Hsu, M. Terrones, N. Grobert, J.P. Hare, H.W. Kroto, D.R.M. Walton, and H. Terrones, *Chem. Phys. Lett.* **309**, 327 (1999).